

2
X-651-72-279

PREPRINT

NASA TM-X-66044

OBSERVATIONS OF THE GLOBAL STRUCTURE OF THE STRATOSPHERE AND MESOSPHERE WITH SOUNDING ROCKETS AND WITH REMOTE SENSING TECHNIQUES FROM SATELLITES

(NASA-TM-X-66044) OBSERVATIONS OF THE
GLOBAL STRUCTURE OF THE STRATOSPHERE AND
MESOSPHERE WITH SOUNDING ROCKETS AND WITH
REMOTE SENSING TECHNIQUES FROM D.F. Heath,
et al (NASA) Aug. 1972 121 p

N72-32417

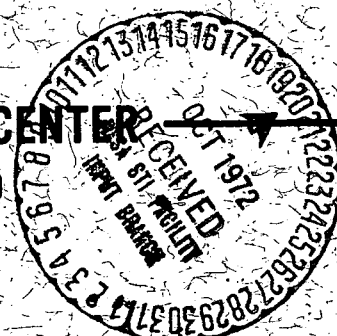
CSCL 04A G3/13

Unclas
43812

AUGUST 1972

GSFC

GODDARD SPACE FLIGHT CENTER
GREENBELT, MARYLAND



Reproduced by
NATIONAL TECHNICAL
INFORMATION SERVICE
U S Department of Commerce
Springfield VA 22151

OBSERVATIONS OF THE GLOBAL STRUCTURE OF THE
STRATOSPHERE AND MESOSPHERE WITH SOUNDING ROCKETS
AND WITH REMOTE SENSING TECHNIQUES FROM SATELLITES

Donald F. Heath, Ernest Hilsenrath, Arlin J. Krueger,
William Nordberg,* C. Prabhakara and J. S. Theon

NASA/Goddard Space Flight Center
Greenbelt, Maryland, U.S.A.

May 1971

*Presented at the International School of Atmospheric Physics,
ETTORE MAJORANA Center for Scientific Culture,
Erice, Italy 13 - 27 June 1971

GODDARD SPACE FLIGHT CENTER
Greenbelt, Maryland

CONTENTS

	<u>Page</u>
1. Introduction	1
2. Techniques for Measuring the Composition, Thermodynamic Structure and Motion Field of the Neutral Atmosphere up to 80 km	3
2.1 Rocket Techniques	4
2.1.1 Radar Tracking of Chaff	5
2.1.2 Thermistor Dropsondes.	5
2.1.3 Falling Spheres	6
2.1.4 The Pitot Probe Technique	7
2.1.5 The Acoustic Grenade Technique.	7
2.1.6 Ozone Sondes	9
2.1.6.1 Optical	9
2.1.6.2 Chemical	10
2.1.7 Atomic Oxygen Probes	11
2.1.8 Water Vapor Probes	12
2.2 Satellite Techniques.	13
2.2.1 Broad-Band Infra-Red Radiometers for Mapping Stratospheric Temperatures.	13
2.2.2 Infra-Red Spectrometers for Measurements of the Temperature and Ozone Distribution in the Stratosphere	16
2.2.3 Spectrophotometers to Measure Backscattered Ultra-Violet (BUV) Solar Radiation for Determination of Ozone and Its Vertical Distribution	20

CONTENTS (continued)

	<u>Page</u>
2.2.4 Photometers to Monitor Ultraviolet Solar Energy	24
3. Results of Observations.	25
3.1 The Mean Thermodynamic Structure and Circulation of the Mesosphere from Rocket Soundings	25
3.2 Small Scale and Short Term Variations in the Vertical Struc- ture of the Mesosphere	31
3.2.1 Thermal Tide	32
3.2.2 Gravity Waves	33
3.3 Temperature Structure in Noctilucent Clouds	36
3.4 Global Stratospheric Temperature Fields Observed with Satellites	42
3.5 Global Ozone Fields from Satellite Observations	49
3.5.1 Total Ozone	50
3.5.2 High Altitude Ozone Distributions	52
3.6 Diurnal Variations of the Vertical Structure of Ozone in the Mesosphere	54
3.7 Rocket Measurements of Atomic Oxygen in the Mesosphere . . .	57
3.8 Long Term Variations in UV Solar Energy Inputs into the Mesosphere	58
3.8.1 Solar Cycle Variations	59
3.8.2 27-Day Variability	60
3.8.3 Flare UV Variability	63

1. Introduction

Until about eight years ago, analyses of the structure and behavior of the upper stratosphere and of the mesosphere were based on rather indirect ground-based observations and on infrequent rocket soundings from isolated sites.

Ground based observations resulted in the description and understanding of only the most basic physical processes of that region of the atmosphere: the absorption of near-ultraviolet solar radiation resulting in the temperature maximum at the stratopause; the photochemistry and transport phenomena responsible for the distribution of ozone and of atomic oxygen in the upper stratosphere and mesosphere; the predominant radiative cooling of the mesosphere resulting in very low temperatures near the mesopause; the accumulation of particles near the mesopause at high latitudes in summer which relate to the noctilucent cloud phenomenon; and the generally easterly winds during summer, alternating with predominantly westerly flow in winter throughout the upper stratosphere and lower mesosphere.

From occasional rocket soundings during the IGY and during subsequent years we have learned: that the temperature structure varies with latitude and season such that at high latitudes during summer, maximum temperatures near 50 km and minimum temperatures near 80 km are extremely pronounced while in winter the temperature extremes at these levels are much less distinct; that the temperature structure in the mesosphere in winter displays large, short-term local variations; that the circulation of the atmosphere up to 70 km follows

patterns of high and low pressure systems which may bring about the onset of sudden stratospheric warmings; and that the general concept of the meridional circulation in the mesosphere, with upward motion over the summer pole and downward motion over the winter pole, which was derived theoretically, is basically correct.

However, until recently, observations were lacking to describe the structure and phenomena of this region in greater detail and on a truly global scale. Systematic exploration of the atmosphere up to about 100 km began in the mid-1960's with simultaneous, seasonal rocket soundings distributed along latitude circles, almost around the globe or along meridians from the equator to high latitudes. This became possible because of the evolution of relatively simple and economical rocket instruments for the direct measurement of such parameters as pressure, temperature, wind, and ozone, and because of the strong interest in exploring this part of the atmosphere by many nations around the world. Also, during these recent years, meteorological satellites have carried "remote sensors" such as spectrometers and image forming radiometers which have permitted the observation of temperature patterns in the stratosphere, the distribution of ozone, and the variation of solar radiation absorbed in the mesosphere on a daily basis over the entire globe.

The systematic rocket soundings and global surveys by satellites have resulted in considerably better descriptions of the structure of, and in better understanding of processes in the stratosphere and mesosphere than was possible

before. For example, from continuous observations with NIMBUS 3 and 4 since April, 1969, we have been able to determine the correlation of variations in the intensity of ultra violet solar radiation between 1200 and 1800Å with the 27 day rotation period of the sun and with other solar activity, while no such correlation was observed at longer wavelengths. The genesis and morphology of stratospheric warmings has been observed with TIROS and NIMBUS satellites during numerous occasions in both hemispheres and on a global scale since 1963. Ozone distributions have been measured with NIMBUS 4 up to 50 km, daily and globally, since April, 1970. Systematic rocket soundings established a relationship between the occurrence of noctilucent clouds and the mesospheric temperature profile. They also demonstrated the vertical propagation of wavelike phenomena and of tides through the mesosphere, and measured the changes in the distribution of ozone between day and night as well as during the polar night up to 70 km.

In the following discussion, a brief description of the techniques involved in these observations and a survey of the results, many of which are still preliminary, will be given. The discussion will be limited to those techniques and results dealing with rocket and satellite programs conducted or sponsored by the National Aeronautics and Space Administration (NASA) of the U.S.A.

2. Techniques for Measuring the Composition, Thermodynamic Structure and Motion Field of the Neutral Atmosphere up to 80 km

Observations of the upper atmosphere are carried out in complementary fashion: Rocket soundings provide measurements with detailed resolution and

accuracy along the vertical scale, but they cannot be deployed in sufficient numbers to provide more than a coarse picture on the horizontal and time scales. Conversely, as many as several thousand satellite observations of temperature or ozone distribution with height are being made daily over the entire globe, but in the vertical scale, each measurement is usually averaged through an interval of 5-10 km. Thus, satellite observations now provide for an unprecedented number of measurements (especially of temperature and ozone in the stratosphere) on a global scale, while rocket soundings complement and supplement these observations with detailed measurements of the vertical structure and of parameters such as winds which are not yet observable with satellites.

2.1 Rocket Techniques

Generally, instruments for measuring temperature, density pressure, composition and winds in the upper stratosphere and mesosphere are carried on two-stage sounding rockets of the Nike-Cajun type. Some observations are based on direct measurements such as those of temperature and pressure with thermistor and electrical gauges, respectively, and the measurement of ozone by means of chemical reactions with substances carried aloft by rockets. Other observations are derived from indirect measurements such as temperature from the measured speed of sound propagation, density from the measured acceleration of spheres dropped from rockets, and ozone from the attenuation of solar radiation. Winds are usually measured by tracking the horizontal drift of objects such as smoke, chemicals, chaff, or parachutes released from rockets,

or of sound waves propagating through the atmosphere. The following techniques have produced significant measurements of the structure of the upper stratosphere and mesosphere during the past several years. About 50 of the larger, two-stage rockets are launched every year to heights of about 100 km from several sites between the Equator and Alaska to measure temperature, pressure, density, wind, and ozone. Many more smaller rockets (several per week from about 14 sites and one or two per month from a few additional sites in the Americas) provide temperature and wind soundings up to about 60 km.

2.1.1 Radar Tracking of Chaff

A vertical profile of the horizontal winds and wind shears can be obtained by tracking the horizontal drift of falling chaff with a radar (Warner and Bowen, 1953). Chaff consists of a large number ($\sim 10^6$) of dipole reflectors, usually fine wire or electrically conductive thin ribbon which is cut to half the wavelength of the tracking radar to improve its reflectivity, and is most often deployed in the 60-100 km altitude region by Loki-class rockets. Considerations of desired fall rate and altitude determine the type of chaff used, but all chaff inherently begins to disperse after falling 20-30 km, so that the radar no longer has a single target and tracking becomes unreliable (Beyers, 1969).

2.1.2 Thermistor Dropsondes

Dropsonde instruments containing immersion temperature sensors are ejected from Arcas-class rockets near apogee to measure (and telemeter) the ambient temperature of the atmosphere as they descend on parachutes or other drag devices from about 60 to 20 km (Ballard and Rofe, 1969).

The pressure profile can then be obtained by the upward integration of the hydrostatic equation using the measured temperature profile and a balloonsonde pressure measurement; the density profile can be calculated from the equation of state (Nordberg and Rasool, 1968). Radar tracking of the metallized parachute provides a wind profile as the sonde descends. The temperature sensor most commonly employed is a 10 mil bead thermistor which has a rapid time response, but at altitudes above 45 km, it is subject to errors caused by radiation, aerodynamic heating, heat conduction from the payload, etc. When the parachute undergoes high fall velocities at the upper altitudes, it does not respond to wind shears effectively.

2.1.3 Falling Spheres

Falling spheres are used as sensors to measure density profiles in the upper atmosphere. Although several variations of the sphere technique are used, i.e., rigid or inflatable, the passive type deployed from a small meteorological sounding rocket near apogee is the most common (Wright, 1969). This sphere is tracked by radar as it falls through the 100 to 35 km altitude range, providing density and, below 70 km, winds also. Changes in the fall rate of the sphere are measured by the radar and, with the use of aerodynamic theory, are interpreted in terms of an atmospheric density profile. Using the density profile derived from the measured accelerations of the falling sphere, the hydrostatic equation can be integrated downward to produce a temperature profile. A pressure profile can be calculated from the density and temperature profiles

using the equation of state. Active spheres contain accelerometers and telemetry instrumentation, and rely on radars for altitude discrimination and wind determination only. However, these systems dictate the use of larger, Nike-Cajun class rockets to deliver the payload to the desired altitude.

2.1.4 The Pitot Probe Technique

The pitot probe technique utilizes pressure sensors mounted in the forward tip of the payload to measure the impact pressure as the Nike-Cajun class rocket ascends through the 30 to 120 km region of the atmosphere (Ainsworth, et al., 1961). The pressure measurements are telemetered to the ground. The impact pressure profile is used, with appropriate aerodynamic theory, to derive a profile of atmospheric density. The temperature profile is calculated by integrating the hydrostatic equation downward using the derived density profile and the pressure profile is obtained from the equation of state (Horvath, et al., 1962). This technique provides data with 0.5 km vertical resolution, but no wind measurement.

2.1.5 The Acoustic Grenade Technique

In the grenade technique, explosive charges (grenades) varying in weight from 0.1 to 1.8 kg are carried aloft in the nose cone of a Nike-Cajun rocket. Up to 31 grenades are ejected and detonated at 2 to 4 km intervals as the rocket traverses the 35 to 95 km region of the atmosphere (Nordberg and Smith, 1964).

The position of the rocket, and therefore of each explosion, is determined by a Doppler tracking system or a high precision radar such as the

FPQ-6, or both. The time of each explosion is detected by sensors in the payload and telemetered to the ground. A ground based array of hot-wire microphones, capable of responding to frequencies between 1-20 Hz, is used to detect and record the arrivals of the sound waves generated by the exploding grenades. The times and positions of the grenade explosions, and the arrival times of the sound waves at the ground based microphones are measured.

The elevation and azimuth angles of the normal to each arriving spherical sound wave front are computed by applying a least-squares-fit to the arrival times at the various microphones. Each wave front is then analytically traced back along its path of propagation through the atmosphere by means of Snell's Law. Wind and temperature data from balloon sondes and rocket sondes below the grenade explosions are used to trace the path of the sound wave from the ground to the level of the first explosion; above this altitude, the results of the grenade sounding itself are used for each succeeding explosion. The origin of the sound wave as determined by ray tracing is compared with the known position of the explosion, and the horizontal difference by which the sound wave has been displaced from one explosion to the next is a measure of the average wind velocity in the layer bounded by the two explosions. The average speed of sound, and hence the average temperature of the atmosphere between adjacent explosions, may also be determined. The temperature and wind profiles consist of discrete points, each representing the average temperature and average wind, respectively, of the vertically stacked horizontal layers between consecutive

explosions. The pressure profile is derived from the temperature profile, using the pressure measured by an accompanying balloon sonde as a reference value. Pressure is calculated as a function of altitude from the hydrostatic equation, by integrating the pressure upward over the temperature profile. The density is then calculated as a function of altitude from the temperature and pressure using the equation of state.

2.1.6 Ozone Sondes

2.1.6.1 Optical

The most common ozone sensing technique measures the intensity of sunlight or moonlight as a function of height with photometers at one or more wavelength bands between 2500 and 3500Å. The method is characterized by its absolute accuracy; in a dropsonde configuration, the ozone concentration can be measured with 10 percent accuracy with one kilometer resolution throughout the stratosphere. Early experiments used spectrographs (Johnson, et al., 1952), but filter photometers are used now, since narrow band interference filters have been developed in that spectral region. Ozone concentrations are computed by iteration from the attenuation of radiation intensity with height in each spectral channel (Paetzold, 1961a). For soundings through the height region of 20 to 60 km, a minimum of two optical filters is required. This technique has been developed for routine daytime use on small rockets by several investigators. The dropsonde approach, in which the instrument is deployed on a parachute at apogee, has been pursued by Krueger and McBride

(1968) in the United States, and by Sissons (1968) and Beach (1970) in Australia. More than 20 soundings have been made by the American group using Arcas rockets. Soundings have been conducted to survey the latitudinal and temporal changes in the ozone distribution, and to provide reference data for calibration or verification of satellite ozone measurements.

An alternate approach has been taken by Nagata, et al. , (1970) in Japan who make measurements from the rocket during ascent. Five soundings have been reported to date. Weeks and Smith (1968) have used a single channel radiometer at 2550\AA on larger sounding rockets to monitor ozone above 50 km in conjunction with other experiments.

Night-time ozone has been measured optically by Reed (1964) in the U. S. and by Carver (1966) in Australia. Reed's experiment was unusual in that the UV airglow was used as a light source.

2.1.6.2 Chemical

In contrast to optical techniques, where natural light sources are required, chemical ozone probes can be used routinely at night. Nocturnal ozone soundings of the mesosphere provide information on the increase of ozone concentration due to "three body" collisions of O with O_2 and the absence of dissociating radiation. This technique has also been used to observe ozone variations in the mesosphere during the polar winter night.

A chemiluminescent sonde dropped from a rocket on a parachute (Hilsenrath, et al. , 1969) makes measurements of ozone from 70 to

15 km. It uses a principle first discussed by Beranose and Rene (1959). Exposure of a chemiluminescent material (Rhodamine B) to ozone causes luminescence which is proportional to the ozone concentration and the sampling rate. The atmosphere is sampled by self pumping as the sonde descends on a specially designed parachute. A ballast chamber is connected to the ambient atmosphere through an inlet pipe and is initially in pressure equilibrium with the atmosphere. The sensor is released at apogee and as it descends through the atmosphere on the parachute, the pressure inside the ballast chamber is lower than the increasing external pressure, resulting in a net flow of gas through the inlet pipe. The chemiluminescent detector and a photometer are positioned along the inlet pipe; thus, the ambient atmosphere is continuously sampled. Photometer, pressure, and flow rate data are telemetered to the ground during the entire parachute descent. Ozone mixing ratios vs height are derived from the measured light intensity. Calibration of the sensor is performed by exposing the instrument to known concentrations of ozone at pressures and flow rates that are expected to occur during the flight. Numerous laboratory studies have been performed to establish the validity of the method and to verify the assumptions upon which it is based. These studies have also demonstrated that under flight conditions, the sonde will not be affected by atomic oxygen.

2.1.7 Atomic Oxygen Probes

A sensor for measuring the height profile of oxygen atoms from approximately 70 to 100 km has been developed by Henderson and Schiff

(1970). This sensor consists of a thin film of silver deposited on a pyrex rod which is sufficiently small to permit free molecular flow of atomic oxygen onto its surface at the measurement altitude range. As the sensor is exposed to the ambient atmosphere during the rocket ascent, the atom flux is determined from the rate of change of the electrical resistance of the silver film. This information is telemetered to the ground during the rocket ascent. Laboratory measurements indicate that this technique is accurate to at least 25 percent.

2.1.8 Water Vapor Probes

A promising technique for water vapor measurements in the mesosphere is a rocket-borne aluminum oxide hygrometer (Chleck, 1966). The hygrometer consists of a thin aluminum foil strip that has been anodized. A coating of gold is vacuum deposited over this strip, to produce an aluminum oxide capacitor. Changes in the ambient water vapor pressure result in corresponding changes in the electrical impedance of the sensor. The measurement range is from approximately 300 K to 150 K dew/frost point temperatures with an error of about ± 2 K at the lower temperature

This hygrometer, which has been flown routinely on a jet aircraft, has produced continuous water vapor data from the ground to just above the tropopause. (Hilsenrath and Coley, 1971). Balloon flights have yielded data in the lower stratosphere. Rocket flights to measure water vapor concentrations in the mesosphere are planned for 1972.

2.2 Satellite Techniques

All observations of the atmosphere below 100 km from satellites are necessarily based on indirect measurements. They permit the derivation of atmospheric composition or temperature from radiometric measurements of the spectral attenuation of either direct solar radiation or of solar radiation reflected by the Earth, and from spectral measurements of infra-red and microwave radiation emitted by the upper atmosphere. Both methods have been employed successfully on meteorological satellites for the United States (TIROS and NIMBUS) to make observations of temperature and ozone up to about 50 km. In addition, the spectral intensity of incident solar radiation between 1200 and 2600 Å was measured with such satellites. These techniques are described below.

2.2.1 Broad-Band Infra-Red Radiometers for Mapping Stratospheric Temperatures

The first satellite observations of global stratospheric temperature fields were based on measurements of the radiant emittance of the atmosphere in the spectral interval 14.8–15.5 μm (Kennedy and Nordberg, 1967). They were obtained by TIROS 7 during June, 1963 to November, 1964. The radiometer consisted of a thermistor bolometer, filters, light gathering mirrors and lenses, and associated electronics. The instantaneous field of view was approximately 5 x 5 degrees which was scanned across the surface of the Earth by the spinning motion of the satellite. A description of this instrument is contained in the TIROS VII Radiation Data Catalog and User's Manual (1964). During each

12 hour period which corresponded to 14 consecutive orbits, the instrument observed the entire zone of the Earth between 65 N and 65 S. Thus, radiation patterns over this "quasi global" zone could be mapped by the satellite every 12 hours. Practically, however, the time interval during which full coverage was achieved ranged over several days because measurements could not be transmitted to the ground for each and every full orbit. Also, the spatial resolution of the measurements was considerably coarser than that ideally possible: although each instantaneous radiation measurement corresponded to an area of 50 x 50 km on the surface of the Earth, the radiometric accuracy of such a measurement when converted to equivalent black-body temperatures was generally poorer than ± 5 C, and required the averaging of many hundred measurements over larger areas and longer time periods. This resulted in nearly full coverage of the "quasi globe" with a relative accuracy of better than ± 1 C in periods of about 10 days.

The radiant emittances measured by the satellite sensor in this spectral interval (14.8-15.5 μm) were primarily due to thermal emission in the vibration-rotation band of carbon dioxide. It was assumed that carbon dioxide is distributed uniformly throughout the upper troposphere and stratosphere. Also, assuming a typical temperature profile for the troposphere and stratosphere such as that given by the U. S. Standard Atmosphere (1962), one may compute for any given height interval in the atmosphere, the radiant emittance which is transmitted to the satellite within this spectral interval. The result of

such a computation shows that more than 90 percent of the total radiation sensed by the satellite is emitted by the atmosphere above 10 km. More than 70 percent of that total radiation is emitted at heights between 10 and 30 km. Thus, if the measured radiant emittances are converted to equivalent black-body temperatures, they can be generally interpreted as atmospheric temperatures averaged over the height range from 10 to 30 km. Equivalent black-body temperature is defined here as the temperature of an isothermal black-body filling the field of view of the sensor which would cause the same response from the radiometer as does the radiation emerging from the top of the atmosphere in the direction of the satellite.

A similar technique was also used with NIMBUS 2 between April and July, 1966. In this case, the spectral interval was somewhat wider than in the previous experiment on TIROS 7. This resulted in considerably more accurate measurements, but decreased the height range of the temperature measurements to somewhat lower altitudes than with TIROS 7. Maximum radiation was received from near the 16 km level and about 75 percent of the radiation emanated from above 10 km. This permitted inferences of average temperatures in the upper troposphere and lower stratosphere. (Nordberg et al., 1966). In contrast to TIROS 7, NIMBUS satellites were fully stabilized such that the radiometer viewed the earth at all times. Scanning across the Earth was therefore achieved with a rotating mirror in front of the radiometer optics (Nimbus II Data User's Guide, 1966).

2.2.2 Infra-Red Spectrometers for Measurements of the Temperature and Ozone Distributions in the Stratosphere

Nimbus 3 carried two and Nimbus 4 carried three spectrometers which measured, among other quantities, spectral radiances in the 14.5 to 15 μ m wavelength range from which temperatures in the stratosphere could be derived. In contrast to TIROS 7 and NIMBUS 2, these instruments provided a very high spectral resolution (5 cm⁻¹ or better) and measurements were made in more than one spectral channel in the 14.5-15.0 μ m interval which allowed derivations of temperatures at different heights in the stratosphere.

The Satellite Infra-Red Spectrometer (SIRS) of Wark and Hilleary (1969) obtained measurements relating to stratospheric temperatures in two discrete spectral intervals. Radiances in several additional wavelengths shorter than 14.5 μ m were also measured from which the temperature profile in the troposphere was derived. The SIRS instrument is a conventional diffraction grating spectrometer, and has been described in detail in the NIMBUS 3 (1969) and NIMBUS 4 (1970) User's Guides. On NIMBUS 3, it measured radiances from the atmosphere in a narrow strip about 200 km wide along the sub-satellite track. On NIMBUS 4, the 11 degree field of view was scanned to 38 degrees on each side of the satellite track. Two observations per day were made at every latitude from 81 N to 81 S: once near noon, and once at night near midnight. The instrumental accuracy was such that each measurement yielded temperatures of a 200 x 200 km area up to an altitude of about 40 km within about ± 1 C. Measurements with the SIRS have been made continuously since April, 1969.

The Infra-Red Interferometer Spectrometer (IRIS) by Conrath et al. , (1970) obtained measurements of spectral radiances over the entire range from 6 to 20 μ m which included not only the wavelengths from 14.5 to 15 μ m from which stratospheric temperature could be derived, but also the emission from ozone between 9 and 10 μ m. The instrument was a Michelson Interferometer with an 8 degree field-of-view which pointed 2 degrees ahead along the sub-satellite track at the beginning of an interferogram. At the end of the interferogram, or ten seconds later, the field-of-view was directed about 2 degrees behind the sub-satellite point. Therefore, the radiation contained in a single interferogram originated from a circular area, about 150 km in diameter. Spectra were obtained by Fourier analyses of the interferograms. About 4000 spectra, each containing information on stratospheric temperatures and total ozone amounts, were obtained daily. Measurements have been made with NIMBUS 3 continuously from April to July, 1969, and with NIMBUS 4 since April, 1970.

The third instrument on NIMBUS 4 to measure stratospheric temperatures was a Selective Chopper Radiometer (SCR), by Ellis et al. , (1970). The object of the Selective Chopper Radiometer (SCR) was to determine the temperature of the atmosphere from the surface of the Earth or cloud top level to 60 km height. Temperature soundings were achieved by observing the emitted infrared radiation in the 15 μ m band from atmospheric carbon dioxide. Height resolution was obtained by a combination of optical multi-layer filters, and selective absorption of radiation using carbon dioxide-filled cells within the

experiment. The four lower channels consisted of a cantilever-mounted blade shutter which oscillated at 10 Hz and successively chopped the field-of-view between earth and a cold reference source (space). The chopped radiation was then passed through a 10 cm path length of carbon dioxide, the pressure being set for each channel to define the viewing depth in the atmosphere. Behind the CO₂ path was a narrow band filter, the centers of which were different for each channel, and a light pipe which converged the radiation on a thermistor bolometer detector. In order to obtain adequate height resolution in the upper layers of the atmosphere, the upper two channels operated as double cell channels, switching the radiation between two half-cells, semicircular in shape and of 1 cm path length, containing different pressures of carbon dioxide. The oscillating shutter used in the four lower channels was replaced by a vibrating 45 degree mirror. During one half-period, earth radiation passed through one half-cell and space radiation through the other; the situation was reversed during the other half-period. This system assumed that, apart from the CO₂ pressures, both halves of a cell had equal optical transmissions. A special in-flight calibration procedure, known as "imbalance calibration" was required to verify this assumption.

Radiances measured by any of these instruments could be converted to temperatures of stratospheric layers, each corresponding to a given spectral interval, similar to the broad band measurements made earlier with TIROS7 and NIMBUS2. However, it was also possible to "invert" simultaneously

measured radiances in different spectral intervals to continuous profiles of atmospheric temperatures with height. This was based on the fact that radiation near the center of the carbon dioxide absorption band ($15\mu\text{m}$) is emitted at higher altitudes (30–60 km) than radiation in the weaker absorption portion of the CO_2 spectrum, such as near $14.4\mu\text{m}$, which is emitted from an altitude range from about 7 to 20 km.

It was first pointed out by King (1958) and Kaplan (1959) that vertical temperature profiles could be obtained from remote infrared measurements. Since then, analytical techniques have been developed by which estimates of temperature profiles could be obtained from actual radiance measurements (Wark and Fleming, 1966; Rodgers, 1966; Strand and Westwater, 1968; Conrath, 1968, Chahine, 1968). These retrieval techniques can be divided into two general categories: techniques which utilize only the radiances measured from the satellite, and statistical techniques which, in addition to the satellite measurements, employ statistical information on the behavior of the atmospheric temperature profiles. Measurements with the SIRS and SCR were "inverted" to temperature profiles by means of statistical analyses (Smith, 1969 and Ellis et al., 1970, respectively). A nonstatistical method, based on an iterative computational technique developed by Chahine (1968) was used for the inversion of IRIS measurements.

The emission of radiation by ozone in the $9\text{--}10\mu\text{m}$ band which was measured with the IRIS was used to extract information on the total amount

and the vertical distribution of ozone (Prabhakara, 1969). A representation containing free parameters was assumed for the vertical distribution of ozone, and the free parameters were evaluated by making a least squares fit of the theoretically calculated radiances to the measured radiances in the ozone band. The vertical ozone distribution was represented in terms of empirical orthogonal functions or characteristic patterns (Obukov, 1960; Mateer, 1965). The empirical orthogonal functions were calculated from ensembles of historical ozone profiles obtained with ozone sondes. From the spectral resolutions and accuracies of the radiation measurements obtained in the IRIS experiment, essentially only one parameter of the ozone distribution could be derived. This was the expansion coefficient of the first empirical orthogonal function. While such a representation provided only relatively crude information on the vertical distribution of ozone, it did, however, permit a meaningful estimate of the total ozone.

2.2.3 Spectrophotometers to Measure Backscattered Ultra-Violet (BUV) Solar Radiation for Determination of Ozone and its Vertical Distribution

An experiment for obtaining the spatial distribution of atmospheric ozone on a global scale, by inversion of measurements of ultraviolet radiation backscattered by the atmosphere, completed one year of continuous operation aboard NIMBUS 4 in April, 1971.

The instrument consists of a double (tandem) Ebert-Fastie spectrophotometer in conjunction with a narrow band interference filter photometer.

Both of the instruments view along the nadir direction of the spacecraft. The spectrophotometer measures spectral intensities at 12 wavelengths from 2555 Å with a 10 Å band pass. The interference filter photometer measures a 50 Å band centered at 3800 Å. A depolarizer is inserted in front of the entrance slit of the spectrophotometer to eliminate any effects due to its polarization properties. The double monochromator is composed of two 25 cm focal length Ebert-Fastie monochromators. Light entering the entrance slit is rendered parallel by a spherical collimation mirror and is then diffracted by a 52 x 52 mm grating of 2400 grooves mm^{-1} (solid angle is 0.043 steradians). The diffracted light returns to the spherical collimating mirror, passes through a roof prism, and is imaged onto an intermediate slit. The light passing through the intermediate slit is dispersed again by a second monochromator. A field lens at the exit slit is used to image the grating onto the photocathode of a photomultiplier. Both gratings are mounted onto a common rigid shaft so that no wavelength tracking error can occur between the two monochromators. A roof prism is used to invert the image in the direction of dispersion at the intermediate slit. This is necessary if one is to double the dispersion in passing through the second monochromator. When passing over the polar regions, diffuser plates are deployed in front of the spectrophotometer and the filter photometer to view the sun for calibration.

The primary reason for using a double monochromator is to obtain the desired spectral purity, i. e., the elimination of scattered light, which

permits one to use a high quantum efficiency (>20 percent for the 12 wavelengths) photomultiplier tube with a dark current of the order of 10^{-11} amp at a gain of 10^6 . A secondary reason is that the aberrations at the exit slit are much less than those produced by a single monochromator. In addition, the use of a double dispersion system permits one to double the slit width while maintaining the band pass of a single dispersion system. Since the radiation energy throughput increases with the square of the slit width, the transmission losses in passing through the second half of the double monochromator are almost offset by the doubled dispersion.

The problem of measuring the Earth radiance in terms of a laboratory standard of spectral irradiance is illustrated in Figure 2.2.3.1. The standard of spectral irradiance (1000 watt, quartz-iodine lamp) and the solar irradiance decrease by only an order of magnitude from 3200 to 2500 Å while the Earth radiance decreases by more than 10^3 over this wavelength interval. In addition, one must either know the polarization characteristics of the measurement equipment or make it insensitive to the polarization of the incident radiation, since for single scattering the polarization of the Earth radiation may be as much as 60 percent at 60 degrees from the sun. The BUV double monochromator uses a Lyot type depolarizer to make it insensitive to the state of polarization.

Because ozone absorption is very strongly wavelength dependent through much of the middle ultraviolet, observations of backscattered energy at several wavelength bands in this spectral region provide a mechanism

for scanning through the atmosphere in the vertical. This wavelength effect is illustrated in Figure 2.2.3.2 which shows the relative amount of energy back-scattered at various levels in the atmosphere for 8 of the 12 wavelengths measured by the NIMBUS 4 BUUV instrument. As wavelength increases, the absorption coefficient decreases, and there is an increase in the depth of penetration of the solar radiation into the atmosphere. Each curve has been normalized to unity at the level of maximum contribution and the area between the curve and the y-axis is directly proportional to the backscattered energy observed at the spacecraft. The curves are based on a mid-latitude ozone distribution having total ozone of 0.336 atm-cm as measured by Hering and Borden (1965).

According to Figure 2.2.3.2, the radiance measurements contain information about vertical ozone distribution from the earth's surface up to about 60 km. However, because of the rather large half-width of the curves, the random errors introduced by the instrument, and random deviations in the atmosphere during the period of measurement, a fundamental limitation is placed on the vertical resolution that can be obtained by the inversion of these measurements [Wei (1962), Mateer (1965), Twomey (1965, 1966)], especially at lower altitudes where the resolution is particularly poor because of the bimodal nature of the weighting curves (e.g., 3058 Å). Therefore an iterative scheme (Mateer, 1971) is used in the derivation of the total amount of ozone assuming certain statistics for its vertical distribution, and using the measured ratios of Earth radiance to solar irradiance at each wavelength. Total amounts of ozone can be determined to an accuracy of about 5 percent.

The distribution of ozone with height above 30 km is determined by means of an iterative inversion of the measured radiance ratios at wavelengths shorter than 2976 Å. For altitudes below 30 km statistical methods (Strand and Westwater, 1968) may be used to infer the ozone distribution with height.

2.2.4 Photometers to Monitor Ultraviolet Solar Energy

A Monitor of Ultraviolet Solar Energy (MUSE) experiment was flown on NIMBUS 3 and NIMBUS 4. A detailed description of these observations has been given by Heath (1971). The absolute solar flux in the 1100-3000 Å region has been measured continuously since April, 1969. Each of the five wavelength intervals was several hundred Angstroms wide. Solar energy in this region represents the major radiative energy input into the lower thermosphere, mesosphere, and upper stratosphere. This wavelength range also covers the transition from photospheric to chromospheric radiation which passes through the region of the solar temperature minimum. The instrument consists of five vacuum photodiodes, each with a nominal 90 degree field of view. The sensors are fully illuminated by the sun for about 20 minutes of each orbit, and they view the sun at near normal incidence on every crossing of the terminator in the north polar regions. The angle of solar illumination to the normal of the face of the sensors is measured precisely with a solar aspect sensor. The short wavelength response is determined by a suitable radiation resistant optical filter. The long wavelength cutoff is achieved through the use of photocathode materials of varying degrees of "solar blindness."

3. Results of Observations

3.1 The Mean Thermodynamic Structure and Circulation of the Mesosphere from Rocket Soundings

The mean profiles of temperature and pressure were computed from 227 soundings carried out from five sites which covered a wide range of geographical latitudes during all seasons. The launch sites included: Natal, Brazil (6 S) and Ascension Island (8 S) which were combined to represent a tropical regime; Wallops Island, Virginia, U. S. A. (38 N) representing a temperate regime; Churchill, Manitoba, Canada (59 N) representing a subarctic regime; and Point Barrow, Alaska, U. S. A. (71 N) representing an arctic regime. (See Smith, et al., 1964, 1966, 1967, 1968a, 1969, 1970, 1971).

Soundings conducted in December, January, and February were averaged to produce mean winter profiles, those conducted in June, July, and August were averaged to produce a mean for summer, and those in March, April, May, September, October, and November were averaged to produce mean profiles for the transition seasons at the Wallops Island, Churchill, and Barrow sites. Since only a very small seasonal dependence was detected in the Natal-Ascension soundings, the data for all months were averaged together to produce a mean annual profile for the tropics. The numbers of soundings and the months included in each model are listed in Table 3.1.1 (see p. 79). Profiles are shown in Figure 3.1.1.

The mean temperature profile for the tropical sites, indicates a mean stratopause temperature of about 260 K, and an indistinct mesopause of about

200 K at 80 km. The mesospheric lapse rate is small and no substantial seasonal effect is observed. The mean seasonal temperature profiles for the middle latitudes (Wallops), indicate that the stratopause temperature is higher than 270 K during all seasons. The mean mesopause temperature is 180 K in summer and about 200 K in winter. Note that the structure in the mesosphere is more disturbed than in the tropics during all seasons, and that distinct differences occur with the change of season. The mean seasonal profiles for the subarctic site (Churchill), show an even more pronounced seasonal variation of temperature. The mean summer stratopause temperature exceeds 270 K while the mean winter stratopause temperature is only about 250 K. The mean mesopause temperature is as low as 150 K in summer, while in winter, the mesopause is undiscernable; during winter, the mean temperature above the stratopause is never lower than 195 K. The mean profiles for the arctic site (Barrow) show a 40 C variation of the stratopause temperature, and a 80 C variation in the mesopause temperature with season. Note the smooth, steep lapse rate in summer and the very cold (140 K) mean mesopause temperature. The winter profile, on the other hand, shows a very shallow lapse rate, and a warm upper mesosphere.

Comparisons of these data with the U.S. Standard Atmospheres Supplements (1966) demonstrate that some substantial differences exist between the statistical mean of these observations and the "Standard" profiles for the corresponding latitude and season (Theon et al. , 1970). Of course, the argument can be made that the observations are valid for only one station while the standard

model is an attempt to give a representative value for a given latitude (i. e. , all longitudes). However, the standard profiles were drawn from earlier observations which were sparser than the data reported here, and, as is evident from recent observations, conditions at any one latitude vary greatly with longitude.

Quasi-meridional cross-sections along a diagonal path traced across the North American continent from Barrow southeastward through Churchill, Wallops Island and across the western Atlantic Ocean to Natal have been drawn from seasonal mean profiles of Figure 3.1.1. The resulting temperature cross-section, shown in Figure 3.1.2, forms an organized pattern dominated by the warm stratopause and cold mesopause of the high latitudes in summer, and the almost isothermal structure of the high latitudes in winter. These features are, in general terms, similar to the earlier models of Murgatroyd (1957) except that the high latitude summer stratopause and mesopause are colder than in Murgatroyd's model. Figure 3.1.2 is also similar to the cross section given in the U. S. Standard Atmospheres Supplements (1966) except that the winter mesosphere shown here is colder.

Combining the mean seasonal pressure profiles into the same quasi-meridional cross-section, results in Figure 3.1.3. Here the values are shown in percent difference from the U. S. Standard Atmosphere, 1962. Note that the zero percent difference line (i. e. , exact agreement with the standard) is most nearly approximated by a low latitude pressure profile in winter, while a well

developed low pressure region dominates the winter mesosphere at higher latitudes and a high pressure region dominates the summer mesosphere. These latitudinal pressure differences drive the mean circulation in the mesosphere, and are consistent with the observed winds. The low pressure (cyclonic) region in the winter mesosphere underlies a high pressure (anticyclonic) region, and the high pressure region in the summer mesosphere underlies a low pressure region. This vertical alternation of pressure systems closely resembles the patterns observed in the troposphere, but the vertical scale sizes are much larger in the upper atmosphere. The patterns shown in Figure 3.1.3 are not necessarily an exact description since we expect that the latitudinal and vertical extent of these systems varies with longitude. Such variation cannot be determined from the observations shown here, since they were made only over a very limited longitudinal segment. Nevertheless, the basic nature of the atmospheric mass distribution in the mesosphere is quite evident. For example, latitude zones where the tightest horizontal pressure gradients are shown in Figure 3.1.3, namely, near 60 km at 45° in winter, are also zones where the most intense zonal winds occur. This is consistent with the observed wind fields. An analysis of the circulation of the mesosphere was made by Theon and Smith (1970), based on the monthly and seasonal mean values of pressure and winds observed from three sites over North America. These observations provide a considerable improvement over earlier circulation estimates for this region which were based on observations at only one or two sites.

Figure 3.1.4 presents mean seasonal "weather" maps over the North American continent for the 60 and 80 km levels. These maps are polar stereographic projections with the north pole indicated by the x at the top center of the figure. Longitudes radiate from that point, and latitudes are concentric circles, the center of which is the pole. The maps were analyzed by plotting the mean wind and mean pressure for the appropriate level for each of the three sites previously mentioned. In addition, the mean wind data from the Meteorological Rocket Network (MRN) in January and July were plotted in the winter and summer respectively, to aid in the analyses. As the altitude increases, horizontal pressure gradients become weaker, necessitating the choice of smaller intervals of pressure to describe the flow at higher levels. These analyses are geostrophic, which means that the curvature of the isobars, friction, and all short term effects have been neglected. Figure 3.1.4a, which gives the mean winter circulation at 60 km, indicates that the flow is dominated by a vortex centered over North Central Canada far from the geographic pole. This circulation produces strong westerly winds over most of the continent, and a predominately northerly component over Alaska. By extrapolating the analysis over the Atlantic (broken lines), one may infer strong southerly winds over Greenland. The polar asymmetry of the flow implies the transport of atmospheric properties across latitude circles. The mean summer circulation at 60 km (Figure 3.1.4b) is dominated by an anticyclone whose center cannot be determined from the available data. This pattern produces easterly winds over most of the continent with the

strongest zonal components occurring along the southern portion of the United States. The pressure gradients are smaller in magnitude in summer than in winter, producing generally lighter winds. Figure 3.1.4c shows the mean winter circulation at 80 km. This coherent circulation is somewhat unexpected since the data from individual soundings fluctuate widely. The averaging process appears to filter out most of the ageostrophic components which appear to be quite large in individual soundings. The prevailing west winds, which are generated by the strong vortex at 60 km, remain essentially intact up to 80 km. But, two disturbances stand out in the mean zonal flow: the ridging over eastern Alaska, which produces a southerly wind over Barrow, and the divergent flow between Wallops Island and Cape Kennedy. The mean circulation in summer at 80 km, shown in Figure 3.1.4d, is vastly different from that at 60 km. The high pressure region to the north of the continent still exists in summer, but ridging appears across the center of the continent in a north-south direction producing a seemingly chaotic circulation. Low pressure regions extend onshore from both the Atlantic and Pacific Oceans, and the flow is generally light (except for Barrow). The appearance of this map may result from the breakdown of the geostrophic assumption at these altitudes. If tides and/or gravity waves dominate the flow, as discussed in the next section, then large accelerations in the flow occur, and the geostrophic balance no longer applies. Averaging a sample of this small size may not adequately remove short term influences, since the variability of the individual soundings about the mean is quite large. Thus, Figure 3.1.4d may not represent a true mean circulation.

3.2 Small Scale and Short Term Variations in the Vertical Structure of the Mesosphere

Since 1967, we have conducted soundings of the atmosphere above 50 km primarily utilizing the acoustic grenade and pitot-static tube techniques to observe short term variations in the temperature, pressure, and density profiles to altitudes as high as 120 km. Soundings closely spaced in time have demonstrated that the structure of the atmosphere above the stratopause is subject to rapid and dynamic changes. Temperature variations are used here to demonstrate the variability of the upper atmosphere clearly.

Superimposed upon the gross seasonal differences in temperature presented in Section 3.1, there are temperature changes which have been observed to occur over short periods of time, e.g., days or hours. Examination of these observations reveals that the variations in the tropics are quite different from those which occur at middle and high latitudes (Theon, 1968). Several different mechanisms appear to be responsible for these short term fluctuations in the upper atmosphere, and several theories have been advanced to explain the observations. Hines (1960) proposed internal gravity waves to explain the irregular motions observed in the lower thermosphere and proposes that this gravity wave mechanism may also be the cause of the wave-like structure in the temperature profiles lower in the atmosphere. Lindzen (1967) proposed thermally driven diurnal tides to explain the periodic motions observed in the stratosphere, mesosphere, and lower thermosphere. In both cases, the propagation of energy

from lower levels upward disturbs the temperature and wind profiles of the upper atmosphere. Examples of observed, short term disturbances in the temperature profiles and comparisons of these with the appropriate theory follow.

3.2.1 Thermal Tides

Large variations in individually observed tropical temperature profiles occur, despite the absence of seasonal changes in the mean profiles. An example of the variability of the tropical upper atmosphere is given in Figure 3.2.1 which shows three temperature profiles observed with the acoustic grenade technique at Natal, Brazil (6 S) in October, 1966. This series of soundings was initiated at sunrise and the second and third soundings were launched approximately 12 and 24 hours later, at the following sunset and sunrise, respectively. Temperature changes of up to 50 C (at 91 km) occurred during the two 12 hour periods, and these far outweighed the small changes which occurred during the 24 hour period. Thus the diurnal variation was greater by far, than other variations. In another instance, a 100 C temperature change was observed in 12 hours at 105 km with a pair of pitot-static tube soundings conducted at the equator in March, 1965. In Figure 3.2.1, the temperature changes vary considerably with altitude so that cooling occurred at the 68 and 90 km levels and heating occurred at the 90 km level during the first 12 hour period.

When the profiles in Figure 3.2.1 are paired and the temperatures at sunrise are subtracted from the temperatures at each sunset, the two profiles of temperature differences, shown in Figure 3.2.2, result. These temperature difference profiles change sign and increase in amplitude with altitude.

The dashed curve in Figure 3.2.2 gives the temperature changes which were derived by Lindzen from theoretical consideration of the thermal tides. The agreement between observation and theory is good above 70 km although the theory underestimated the amplitude of the cooling above 85 km. The agreement is remarkable considering that the theoretical profile is based on assumed vertical distributions of temperature, water vapor, and ozone.

According to theory, these temperature variations are due to solar heating of water vapor in the troposphere and ozone in the stratosphere which generate periodic disturbances that propagate upward into the mesosphere and lower thermosphere. The amplitudes of these disturbances are small in the region where they are generated, but they increase inversely as the square root of the density. The phase of the disturbance varies continuously and in an irregular manner with altitude. The distinguishing characteristic of the short term temperature variation produced by the thermal tides is their regular, periodic recurrence. In Lindzen's model, the amplitude of the thermal tide diminishes rapidly with increasing latitude. Thus the diurnal temperature variations produced by this mechanism become small at middle and high latitudes and are masked by other effects.

3.2.2 Gravity Waves

Wave-like features in the temperature structure of the mesosphere and lower thermosphere, which are superimposed upon the average seasonal profiles, have been observed at both middle and high latitudes in winter

and at middle latitudes in summer. Figure 3.2.3 gives typical temperature profiles obtained with the acoustic grenade technique at a mid-latitude site, namely Wallops Island, Virginia (38 N). These profiles were observed over a period of several years and grouped according to season. The three upper plots are for consecutive winters, and the two lower plots are for consecutive summers. For two of the three winters, temperature fluctuations were much greater than in summer, while during the winter of 1965, a stratospheric warming was observed, but fluctuations in the mesosphere were relatively small. Typical temperature profiles obtained with acoustic grenades for the winters and summers of several years at Churchill, Canada (59 N) are shown in Figure 3.2.4. The average amplitude for the winter temperature fluctuations is about 30 C, but in summer, there is no consistent wave-like structure in the mesosphere. If the profiles in Figure 3.2.4 are compared with the seasonal averages given in Section 3.1, the summer profiles are seen to be well described by a single average temperature profile, but the winter mesosphere changes so dynamically from day to day that the average winter profile is not representative of any given time. At even higher latitudes, namely, at Point Barrow, Alaska (71 N) this contrast is still more pronounced. The summertime mesosphere temperature profile is extremely uniform, as can be seen in Figure 3.2.5a. The seven acoustic grenade soundings were made over periods spanning two summers; yet, the temperature spread is no greater than 10-15 C at any given altitude below the mesopause, and there is no trace of the wave-like structure. Contrast these results with the 6 temperature soundings given in Figure 3.2.5b. These were observed with the

acoustic grenade technique during a 15 hour period at Barrow on 31 January - 1 February, 1967. Temperature changes of up to 80 C were observed to occur in less than 3 hours. The wavelengths of the structure averaged about 10-15 km, and the amplitudes increased with altitude (Smith et al., 1968b). The following analysis was performed on the soundings shown in Figure 3.2.5b: Average temperatures were computed at each height level from the six soundings and were subtracted from the temperatures of each of the individual soundings. These differences were then plotted in Figure 3.2.5c as a function of altitude in a time cross section for the 15 hour period. Isolines for zero temperature change were drawn to separate the zones of positive difference (heating) from the negative difference (cooling). The phase of the waves was assumed to propagate downward. An average wave period of approximately 200 minutes is obtained from Figure 3.2.5c, with minimum periods of 85 minutes and maximum periods of 330 minutes occurring at the higher and lower altitudes, respectively.

Temperature variations observed at middle and high latitudes thus have much shorter periods than the diurnal waves observed in the tropics. As at low latitudes, there is a definite periodicity, and amplitudes increase with height. There is some selective mechanism which allows these disturbances to propagate upward in winter, but not in summer at high latitudes. Perhaps this dependence on season is a result of the generating mechanism at low levels, or of the vertical wind shears suggested by Hines and Reddy (1967). The regular vertical wavelength of 10-15 km, and the relatively short period suggest that a

mechanism such as the internal gravity waves proposed by Hines are responsible for the variations, which amount to as much as 80 C in 3 hours near the mesopause. At higher altitudes (120 km), temperature changes of over 150 C were observed at Churchill, but these large temperature variations may have been caused by intense auroral activity which was observed at the same time.

3.3 Temperature Structure in Noctilucent Clouds

Noctilucent clouds have been a subject of interest for many years because of the great heights above the earth at which they occur. These clouds have generally been observed at altitudes ranging from 78 to 90 km, the majority of observations indicating a cloud height of about 83 km (Fogle, 1966). They have been sighted only at high latitudes and most frequently during the 4- to 6-week period following the summer solstice. Noctilucent clouds are visible only during the time that the sun is below the observer's horizon, and they are directly illuminated by sunlight against a darkened sky background. High latitudes provide favorable geometry for observation of the clouds for considerably longer periods each day than middle or low latitudes do, but the fact that clouds exist only at high latitudes and only during summer can be explained in terms of the temperature structure of the mesosphere at these latitudes.

The acoustic grenade technique was employed to provide measured profiles of atmospheric temperature, pressure, density, and wind to an altitude of 95 km during displays of noctilucent clouds. A total of ten grenade soundings were carried out from Kronogard, Sweden (66 N) (Witt et al., 1965), and Barrow,

Alaska (71 N), during the summers of 1963 through 1965 to determine the relation between the mesospheric temperature structure and the occurrence of noctilucent clouds. Results of soundings at Barrow (August, 1965) and Krongard (1963) are given in Figure 3.3.1. As discussed in section 3.2, these profiles display remarkable uniformity. The mesopause temperatures ranged from 130 to 148 K, and the steep uniform lapse rate, which is typical of the high latitude summer mesosphere, was observed in all the soundings. An error analysis has been performed on these data, and the errors associated with the temperatures mentioned above are 1 to 3 C. Very little change in the temperature structure can be seen between soundings made in the presence and absence of noctilucent clouds. The first sounding at each site was conducted during a display of noctilucent clouds, and the second served as a control sounding, having been carried out in confirmed absence of the clouds. At Barrow, the minimum temperature of the profile made in the presence of clouds was 139 K, which is 3 C warmer than the mesopause temperature of the control sounding. At Kronogard, however, the minimum temperature of the profile made during the cloud display was 130 K, or 18 C colder than the mesopause temperature of the control.

The profile of the average temperature for five soundings conducted during displays of noctilucent clouds (Figure 3.3.3) and the average profile for three soundings conducted during the confirmed absence of these clouds do not differ by more than 5 C at any point between 45 and 90 km. The warm stratosphere, the steep uniform lapse rate, and the extremely cold mesopause are

essentially identical for both average profiles. For five soundings conducted during displays of noctilucent clouds, mesopause temperatures varied from 130 to 147 K. Correspondingly, for soundings conducted in the absence of clouds, the mesopause temperatures ranged from 129 to 149 K. Thus the coldest temperatures did not necessarily produce noctilucent clouds, but the clouds were always accompanied by mesopause temperatures less than 150 K.

There are two schools of thought concerning the composition of noctilucent cloud particles. One theory assumes the presence of sufficient water vapor at the mesopause to form ice particles by a process of saturation and condensation (Humphreys, 1933). The other does not accept the presence of water vapor and ice, but explains the noctilucent clouds in terms of the light-scattering properties of the dust alone (Ludlum, 1957), which is believed to originate from the vaporization of incoming meteors or from the surface of the Earth. Sampling experiments have been conducted to resolve the question of the composition of cloud particles, and traces of a volatile substance believed to be ice were found surrounding many of the larger particles obtained from a noctilucent cloud (Hemenway, et al., 1964).

In view of the temperature data reported above, it appears that the occurrence of noctilucent clouds depends largely on the amount of water vapor present at the mesopause. Khvostikov (1966) has postulated that "Noctilucent clouds appear in the atmosphere at the place and the time where and when the temperature of the air turns out to be low enough." However, the results shown

in Figure 3.3.1 indicate that a given low temperature alone is not sufficient to produce noctilucent clouds, unless the low temperature occurs in conjunction with sufficient water vapor. Thus the water vapor content of the high atmosphere must be considered.

Seasonal variations of the mesopause temperature not only produce sufficiently cold conditions for the formation of noctilucent clouds, but also provide a circulation consistent with the transport of water vapor to the mesopause at high latitudes in summer. According to section 3.1 the high-latitude summertime mesopause is about 80 C colder than the wintertime mesopause. These seasonal variations of temperature are not consistent with considerations of radiation alone, since at high latitudes, the summer mesosphere is heated almost 24 hours a day, and the winter mesosphere is dark almost 24 hours a day. Leovy (1964) demonstrated that a meridional circulation superimposed on an atmosphere in radiative equilibrium produced good qualitative agreement with observed seasonal variations of temperature. This meridional circulation caused ascending motion at the summer pole and descending motion at the winter pole, thereby transferring heat from the radiatively heated upper atmosphere of summer to the heat-deficient upper atmosphere of winter.

Hesstvedt (1964) used a meridional circulation similar to that proposed earlier by Murgatroyd and Singleton to explain the presence of water vapor in the upper atmosphere. This model is also consistent with the observed variations of temperature. As can be seen in Figure 3.3.2, Hesstvedt's model shows

that the source of water vapor is the tropical troposphere, and that water vapor enters the stratosphere through the gap in the tropopause. From this relatively narrow latitudinal band near the equator, air rises to an altitude of 25 km, moves meridionally toward the summer pole, and then ascends rapidly at high latitudes. Poleward of 60 degrees latitude in the summer hemisphere, air at 80 km is seen to originate from the equatorial troposphere. Such a model qualitatively explains the mechanism both for transporting water vapor to the summer mesopause and for transferring heat from the summer mesosphere to the winter mesosphere, thereby accounting for the observed seasonal variations in the temperature structure. There is no more reason to believe that water vapor is homogeneously distributed in the high-latitude mesosphere than to believe that such a situation exists in the troposphere. The meridional circulation shown in Figure 3.3.2 represents the average motion in the stratosphere and mesosphere, but this circulation is subject to frequent and dynamic changes, and, therefore, any assumptions of steady-state flow or homogeneous composition are unrealistic. Thus the low temperatures at the mesopause may not produce noctilucent clouds if there is insufficient water vapor available. Questions of the amount of water vapor available and the magnitude of the vertical velocity necessary to transport water vapor to the mesopause must remain unanswered for the present, since no in situ measurements have been made to confirm or to refute the estimates and extrapolations that have been published. Figure 3.3.3 shows that Hesstvedt (1962) estimated the mixing ratio at the mesopause to be 1 g kg^{-1} , which corresponds

to a frost point of 172 K at 82 km. Hesstvedt (1964) later revised this value downward to the order of $10^{-2} \text{ g kg}^{-1}$, which is consistent with Paton's (1964) estimate of $6 \times 10^{-3} \text{ g kg}^{-1}$ ($6 \times 10^{-3} \text{ g kg}^{-1}$ corresponds to a frost point of 150 K at 80 km). Charlson (1965) used the mesopause temperature measured at Kronogard (130 K) as a conservative approximation to develop a steady-state model for noctilucent clouds. Thus, estimates of the content of water vapor at the mesopause have grown smaller with the observations of lower mesopause temperatures.

Figure 3.3.3 also shows a comparison of the frost points for various mixing ratios and a curve which has been extrapolated from measurements at altitudes reached by balloon-borne instrumentation, with the average temperature profile for the five soundings made during displays of noctilucent clouds. Curves A, B, and C were computed for constant mixing ratios with the use of the pressure profile derived from the average of 15 measured temperature profiles at high latitudes in summer. Curve A gives the frost points for a mixing ratio of $10^{-3} \text{ g kg}^{-1}$, curve B for $10^{-2} \text{ g kg}^{-1}$, and curve C for $10^{-1} \text{ g kg}^{-1}$. Badinov, et al., (1966) have extrapolated values for frost points from measurements made by various techniques at balloon altitudes of 28 to 30 km, and these are given by curve D. The average temperature profile for the five soundings of noctilucent clouds is given by curve E. The mesopause temperature of 143 K corresponds to a saturation mixing ratio of approximately $1.3 \times 10^{-3} \text{ g kg}^{-1}$. It must be remembered, however, that this is an average value of the mixing ratio and that both cooler and warmer temperatures, corresponding to lower and higher saturation mixing ratios, have been measured during the cloud displays.

Since no significant difference in the observed temperature was noted between the soundings conducted in the presence of noctilucent clouds and those conducted in the absence of the clouds, it appears reasonable to conclude that a mesopause temperature of less than 150 K is a necessary, but not sufficient, condition for the existence of noctilucent clouds. Variability of the water vapor content at the mesopause is also believed to be a key factor in the occurrence of these clouds. In view of the circulation that is implied by the seasonal differences in temperature in the mesosphere, small amounts of water vapor may be transported by this circulation into the mesosphere during the summer at high latitudes. It is at these latitudes that saturation or super-saturation occurs in the narrow layer at the mesopause where these extremely cold temperatures occur. Dust particles, probably originating from incoming meteors, serve as sublimation nuclei in this saturated region, and grow to sufficient size to scatter sunlight, thus producing noctilucent clouds.

3.4 Global Stratospheric Temperature Fields Observed with Satellites

The first global patterns of stratospheric temperatures observed with satellites were presented by Kennedy and Nordberg (1967). They dealt with the results from TIROS 7 which produced measurements of temperatures "weighted" over a broad slab of most of the lower stratosphere. Nevertheless, these patterns provided a synoptic insight into the seasonal variations of that region which was not possible with previous conventional observations. A total of about 70 "quasi-global" maps, from 65°N to 65°S were analyzed by Kennedy (1966). Two

of these maps are shown here in Figures 3.4.1 and 3.4.2. The temperature patterns are indicative of the summer polar anticyclones and the winter polar vortices. During June, 1963, the warm core was centered over the north polar cap, and the cold core over the south polar cap. A significant deviation in the symmetry of the rather closely spaced isotherms around the south pole occurs over the central South Pacific. A ridge of warm air (high pressure) extends to high latitudes southeast of Australia and over New Zealand while cold air (low pressure) penetrates to low latitudes over the eastern Pacific Ocean, suggesting anticyclonic circulation over Australia. Differences of about 6 C in equivalent black-body temperatures along latitude circles are observed between the western and eastern South Pacific. This asymmetry was observed during both the 1963 and 1964 Southern Hemisphere winters, and was observed again with greater detail in the south polar region during 1966 with the Nimbus 2 satellite (see Figure 3.4.5 below). During September, 1963 the warm air ridge spread considerably westward so that the equivalent black-body temperature difference between the Pacific and the Indian Oceans along 60 S was almost 20 C.

Northern Hemisphere isotherms display a pattern which is well correlated with the circulation features already known from radiosonde observations in this region (Figure 3.4.2). This correlation lends confidence to the application of satellite observations to infer circulation in areas where no conventional observations exist.

Temperatures in the tropics are considerably lower during December-January than they are during June-July (Figure 3.4.3). There is an almost perfect

phase relationship between the high latitude Northern Hemisphere and tropical temperature curves (a and b) and a 180 degree phase lag between the tropical and high latitude Southern Hemisphere temperature cycle (curves b and c). Note the almost identical zonal average temperatures at high northern and southern latitudes and in the tropics during the equinoxes. The difference in the amplitudes of the high latitude curves in the two hemispheres in winter indicates that the magnitude of the temperatures in the stratosphere are strongly influenced by probably both radiative exchange with the surface and lower atmosphere, and eddy transfer of energy within the stratosphere. The warm anti-cyclone over the North Pacific is obviously responsible for the fact that zonal average temperatures between 40-65 N are 4-6 C higher in December-January than corresponding temperatures between 40-65 S during June-July. The almost equal amplitudes of the two high latitude curves in Figure 3.4.3 during summer indicate that such effects are of lesser consequence in summer.

The TIROS 7 data also permitted, for the first time, the analysis of the development of the final stratospheric warming in the Northern and Southern Hemispheres during March, 1964 and September, 1963, respectively. The essence of this analysis is illustrated in Figures 3.4.4a and b.

Similar measurements were made with NIMBUS 2 (Warnecke and McCulloch, 1967). In this case, because of the higher inclination of the satellite orbit, these measurements included both polar regions. The position of the southern polar vortex with coldest temperatures located over the South Pole is

shown, Figure 3.4.5, as derived from NIMBUS 2 observations on June 10, 1966. The temperature pattern is extremely asymmetric. Warmer mid-latitudes and stronger temperature gradients than elsewhere exist toward the Australian and western Pacific side of the hemisphere. This asymmetry which has been observed consistently in the Antarctic winter with the instruments on TIROS 7 and NIMBUS 2, 3, and 4, seems to indicate that dynamic processes strongly counteract the radiative heat loss which is responsible for the cold air cyclone in the Southern Hemisphere winter stratosphere.

Global stratospheric temperature analyses were made by Prabhakara, et al., (1971) based on the "inversion" of 14 to 15 μ m radiances measured with the IRIS. In that analysis, global temperature maps for both the 10 mb and 50 mb levels were drawn for the period 25 to 29 April 1969. Figure 3.4.6 shows one set of these maps for the 50 and 10 mb levels. The 50 mb (approx. 21 km) map reflects the lower stratospheric regime: the middle and high latitudes of the Northern Hemisphere display a series of waves of wavenumber 4 and 5 in the zonal temperature pattern around the globe; the tropical regions between 20 N and 20 S are characterized by a belt of very cold air separating warmer air on both sides. The temperatures, in general, increase from equator (approx. 208 K) to the North Pole (approx. 228 K) while toward the Southern Hemisphere warm air (228 K over the Indian Ocean and 218 K over the eastern Pacific) is sandwiched between the cold tropics and the cold vortex over the Antarctic. This is in accord with the earlier TIROS and NIMBUS 2 observations. The 10 mb

(approx. 32 km) level maps show a steady increase of temperature from south pole (208 K) to north pole (235 K) indicating that the cooling of the Southern Hemisphere has progressed considerably further at this level than at 50 mb. The characteristic asymmetry in the south polar vortex mentioned earlier is still evident at the 10 mb level.

The most complete analysis to date of stratospheric temperatures observed by satellites was made by Fritz and Soules (1970). Radiances measured by the SIRS instrument on NIMBUS 3 in a narrow 5 cm^{-1} wide spectral interval near $15\mu\text{m}$ were analyzed globally for the period April, 1969 to April, 1970. No attempt was made to convert the radiances to atmospheric temperatures, but, the radiance patterns in themselves are extremely revealing of the temperature structure of the "middle stratosphere." All radiation in this spectral channel is received from the stratosphere and more than half of it is received from heights greater than 30 mb. The annual variations at different latitudes analyzed by Fritz and Soules (Figure 3.4.7) are in essential agreement with those derived from TIROS 7 (Figure 3.4.3), but they were obtained with a much higher resolution of both time and latitude zones. Once again, the remarkable uniformity of stratospheric temperatures over the entire globe during the equinoxes can be seen. The warming in the Northern winter from January to March is also extremely pronounced. The minimum temperature in the tropics occurs again in December/January, but maxima at the equator are observed at the equinoxes which is in contrast to the TIROS 7 results which showed the maximum temperatures in the tropics in June/July. Apparently, the TIROS 7 observations were

averaged over too wide a latitude band (30 N to 30 N) to show the behavior of the Equatorial Zone. A most significant result of Fritz and Soules is that all stratospheric warmings in the winter hemisphere are accompanied by simultaneous coolings in the stratosphere of the tropics and the summer hemisphere. Figure 3.4.8 shows this out-of-phase relationship in the radiances averaged around latitude circles. However, these changes did not occur at all longitudes. When the warming reached their maxima, the higher radiances occurred only in one part of a latitude zone, while widespread cooling took place in the tropics and in the summer hemisphere. Fritz and Soules believe that these out-of-phase changes of stratospheric temperature may be explained by heat transfer changes which result from variations in the meridional circulation and large-scale eddies.

Radiances measured by the SCR instrument on NIMBUS 4 have been inverted to temperature profiles up to 60 km and analyzed in terms of daily variations of the global temperature structure since April, 1970 by E. J. Williamson and J. T. Houghton of Oxford University, England. Figures 3.4.9 and 3.4.10 are examples of these analyses, and are shown here through the courtesy of Williamson and Houghton. Figure 3.4.9 displays meridional temperature cross-sections for four days (near the solstices and equinoxes) from the surface to heights of about 60 km. The upper portions of Figure 3.4.9 are comparable to the lower portion of Figure 3.1.2. The SCR measurements for 21 January 1971 correspond indeed with the mean cross-section shown in Figure 3.2.1. However, the 16 July SCR data show a much warmer and higher stratopause for the

winter (South) polar region than would be expected from Figure 3.2.1. It should be noted that it took some 200 rocket soundings over a period of nearly a decade, and the assumption of complete seasonal symmetry between Northern and Southern Hemispheres to interpret Figure 3.2.1 on a truly global scale, while one global cross-section of Figure 3.4.9 was observed in one single day. The asymmetry in the seasonal temperature extremes between the North and South polar caps is quite interesting. During summer, both regions show the well known weak temperature lapse rate in the troposphere, a shallow tropopause and a very steep temperature increase throughout the stratosphere. In winter, however, the north polar region shows the expected, nearly isothermal troposphere and stratosphere with a very shallow tropopause and stratopause, while the south polar region displays a remarkably cold tropopause (180 K) at the extremely high altitude equivalent to 30 mb; indications of an unusually warm (270 K) and high (0.5 mb) stratopause at the south pole are also found in Figure 3.4.9 for 16 July 1970. The dynamic structure of the stratosphere is illustrated by Figure 3.4.10 where vertical cross-sections across longitudes of the temperature deviations from a mean for the latitude belt of 55-66 S are shown for three days during September, 1970. On each of the three days, the westward slope of the temperature deviations with height is clearly evident. For example, on 4 September, at a height of about 1 mb, the characteristic warm sector of the Southern Hemisphere (+20 C deviation) is located near 30 E, while at 200 mb a deviation of equal amplitude is found near 90 E. Five days later, on 9 September, this

warm sector has intensified to +25 C deviation and moved further eastward in the lower stratosphere, while at the 1 mb level it has split into two centers one at 50 E, the other at 120 W. In general, it is observed that cold and warm regions in the lower stratosphere are overlain by warm and cold regions, respectively in the upper stratosphere.

3.5 Global Ozone Fields from Satellite Observations

The principal impetus for observing atmospheric ozone on a global scale arises from the fact that the ozone concentration at altitudes below 30 km serves as a tracer of the general circulation of the atmosphere, while at higher altitudes, ozone relates to the heat budget and the photochemistry of the atmosphere.

Ozone is produced in the middle stratosphere (30-40 km) at low and mid-latitudes by photochemical processes and transported to other heights and latitudes by the vertical and meridional motions of the atmosphere. About two-thirds of the ozone is found in the lower stratosphere (below 30 km) where it is protected from photochemical modification by the absorption of dissociating radiation at higher altitudes. The lower stratosphere ozone is moved by winds and eddy motions until it is either destroyed by oxidation reactions or lost in the troposphere. Dobson Spectrophotometer measurements of the total columnar ozone content have given systematic data on the fluctuations of the lower stratosphere ozone. It has become apparent that the total ozone field is more complex than can be determined from the existing network of about 80 stations, located primarily in the northern hemisphere. The general latitudinal gradient

of total ozone is modulated by longitudinal patterns which seem to be related to tropospheric pressure patterns.

Balloon ozone soundings have been useful in demonstrating the relationships between total ozone amounts and the vertical ozone distribution. They have also served in characterizing the quasi-horizontal transport processes near the base of the stratosphere. The density of balloon ozone sounding stations, however, is inadequate for a study of the general circulation mechanisms.

The ozone source region in the middle stratosphere is above balloon altitudes. The amount of ozone in that region is a small fraction of the total ozone amount which is dominated by the lower altitude ozone. The only reliable source of data for this region has been from sounding rockets. The number of flights of instruments with well defined absolute accuracy has been sufficient only to provide a general understanding of the photochemical processes and of static-equilibrium ozone distributions, and to hint that transport processes might actively modify the distributions. The systematic, global observations of both total amount of ozone and its vertical distribution, especially above 30 km, from NIMBUS afford an excellent opportunity to analyze the circulation of the lower stratosphere, and to study the combination of photochemistry and transport processes in the middle stratosphere.

3.5.1 Total Ozone

Figure 3.5.1.1 shows a latitudinal profile of total ozone observed during one single orbit of NIMBUS 4 on April 15, 1970. Simultaneous

observation by the BUV and IRIS instruments are compared to results from earlier observations from shipboard by the Dobson spectrophotometer (White and Krueger, 1968). It is interesting to compare the time scale of the observations. It took 54 days to acquire the shipboard data, while the satellite data were taken in 54 minutes!

The shipboard Dobson data are consistent with climatological mean values where available from fixed stations. The differences between the recent satellite and earlier shipboard observations are representative of the short-term variability at mid-latitudes. The IRIS and BUV results agree reasonably well between 70 N and 45 S but total ozone measured with the BUV is about 7 percent lower than that measured with IRIS. According to Mateer, et al., (1971), the BUV measurements systematically underestimate total ozone by about 0.020 atm.-cm from simultaneous comparisons with Dobson observations. The same major features of the variation of total ozone amount with latitude appear in both sets of data, but the fine scale structure differs between the two observing techniques. This is probably due to the differences in the field-of-view of the two instruments (5 x 5 degrees for IRIS and 11 x 17 degrees for the BUV). Between 45 S and 74 S the measurements diverge considerably, although similar structural features appear in both profiles. The BUV values seem in better agreement with the shipboard observations and with climatological data for Antarctica. The reason for this discrepancy appears to be that the near isothermal temperature structure of the stratosphere over Antarctica introduces errors in

the retrieval of ozone amounts from the IRIS observations. The IRIS measurements depend on the thermal emission from the atmosphere, and therefore on a strong temperature gradient with height. Thirteen profiles such as that given in Figure 3.5.1.1 may be obtained from NIMBUS 4 daily with each of the two instruments. Daily global maps of total ozone were constructed from the BUUV observations which are shown in Figures 3.5.1.2a and b. Longitudinal variations in the total amount of ozone are strongly related to upper tropospheric and lower stratospheric pressure patterns. For example, high amounts of ozone near Greenland and over Siberia appear to be related to persistent low pressure systems in these regions. In the southern hemisphere autumn, the latitudinal gradients of the ozone amount are less steep than gradients in the northern hemisphere during spring.

Mean monthly global maps of total ozone were prepared from the IRIS observations with NIMBUS 3 for April, May, June, and July, 1969. They are shown in Figures 3.5.1.3a-d. The minimum in the total ozone over the equatorial region is produced by the transport of ozone away from the equator to higher latitudes by the Hadley circulation in the stratosphere. However, in July, the total ozone values in this equatorial minimum increase to about 270 Dobson units, suggesting the probable weakening of the Hadley cell at that time.

3.5.2 High Altitude Ozone Distributions

A parameter which is particularly useful for analysis of the middle and upper stratosphere is the ozone-to-air mixing ratio. Within a given

parcel of air, the mixing ratio is unmodified by vertical or horizontal displacements; only photochemical or chemical reactions can change its value. Latitudinal cross-sections of mixing ratios in the stratosphere from 10 mb to 0.2 mb have been prepared from the BUUV observations over the latitude range 70 S to 80 N. One such cross-section for an equatorial crossing of 56 E on July 5, 1970, is shown in Figure 3.5.2.1. The contours are values of constant O_3 to air mass mixing ratio in $\mu\text{gm gm}^{-1}$. At pressure levels greater than 4 mb (lower than 37 km), mixing ratios are practically symmetrical with latitude about the Equator in April and 10 N in early July. Relatively high mixing ratios of ozone are centered in the tropics but decrease abruptly toward the poles at about 20 degrees latitude from the center. A cellular structure can be observed within the tropical region. Mixing ratios in the polar winter region (South Pole) are 15-20 percent lower than what those measured in the polar summer (North Pole). At pressures lower than 4 mb (heights greater than 37 km), distributions are not symmetric about the Equator. Mixing ratios at those altitudes increase monotonically from north to south. The winter hemisphere between 40-60 S exhibits a striking maximum at the 1 to 3 mb levels.

The global nature of these characteristics is shown in Figures 3.5.2.2 a-d. In Figures a and b, the total ozone above 10 mb has been plotted for both hemispheres. They show symmetry about the Equator with zonal gradients circling about the minima at both poles. The total amounts are approximately equal in the two hemispheres with highest values at low latitudes and

minima at both poles. Longitudinal variation features appear to bear little relationship to the lower stratosphere ozone. Figures c and d show the total ozone above the 2.8 mb level. The two hemispheres are remarkably dissimilar in this case. The northern hemisphere has weak gradients and irregular contours. The southern hemisphere has strong gradients with contours centered at the pole. Total ozone amounts in the southern hemisphere are about double those in the northern hemisphere. The highest values are found, not at the pole, but near 50S.

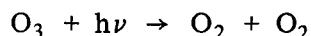
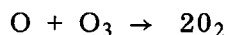
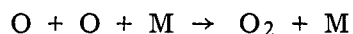
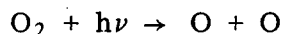
Calculations of the ozone distribution assuming a static atmosphere model have shown the mixing ratio maximum near the equator (Dütsch 1969), and correspond approximately to our observations in the northern hemisphere (summer). The southern hemisphere (winter) maximum, however, has not been reproduced by these calculations.

3.6 Nocturnal Structure of O_3 in the Mesosphere

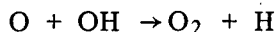
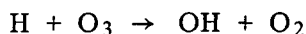
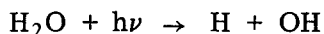
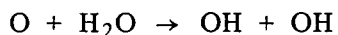
Ozone measurements up to 67 km with the chemiluminescent rocket sounding technique described in 2.1.6 were first obtained at Wallops Island, Va., in 1968, and were compared with simultaneous optical rocket and chemical balloon soundings. Good agreement among all techniques was demonstrated in the regions where the measurements overlap, as shown by Figure 3.6.1.

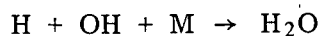
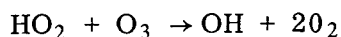
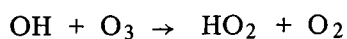
In March, 1970, and March, 1971, pairs of chemiluminescent ozone soundings were made at Wallops Island, Virginia (38 N), and at the Guiana Space Center (5 N) to determine the diurnal variation of ozone concentrations at various

latitudes in the mesosphere. The results of these experiments are shown in Figure 3.6.2. At both locations, the day/night variations in O_3 concentration are smaller than those calculated on the basis of even a "wet" model of the atmosphere where the hydrogen compounds play a major role in the photochemistry of the mesosphere. Water vapor or other constituents responsible for the decomposition of ozone may be present at these heights in greater amounts than previously expected. In the pure oxygen or "dry" model only the following reactions are considered:



In the "wet" model, described in detail by Hunt (1966) the decomposition of H_2O by oxygen atoms starts a chain of reactions which, by their reaction rates, are more effective in controlling O and O_3 in the mesosphere than if only oxygen were considered. The following equations demonstrate these additional sinks for O and O_3 due to the presence of water vapor.





Significantly, the rate coefficients of these reactions have no known temperature dependence, whereas those in the pure oxygen atmosphere are temperature dependent.

In January, 1969, two chemiluminescent ozone soundings were made from Pt. Barrow, Alaska (71 N). The objective of this experiment was not only to measure the ozone distribution in the polar winter night, but also to measure this distribution before and after a stratospheric disturbance (Hilsenrath, 1971). Figure 3.6.3 shows the results of the two ozone soundings performed on January 11 and 30. The solar zenith angle was 125 degrees for both flights, while the minimum zenith angle during the days of the launch was 93 degrees and 80 degrees for the 11th and 30th of January, respectively. In the mesosphere, the ozone profiles show an essentially monotonic decrease of ozone concentration with height, in contrast to the distribution observed at lower altitudes. It was thought that in the absence of ultraviolet radiation responsible for the production of O and loss of O₃, some structure would appear in the profiles even at higher altitudes, especially in light of the highly disturbed temperature and wind fields that occur at high latitudes during the winter. Since this structure did not appear, one might conclude that the chemical restoration time constants are short enough, or mixing is rapid enough to yield the measured smooth profiles. Another

significant feature of this experiment is the variation of ozone near 60 km. Temperature soundings at this altitude conducted within 3 hours of the ozone soundings indicated a temperature decrease of approximately 50 C near 60 km, for the same period during which the ozone concentration increased by almost a factor of four. This result is consistent with the pure oxygen model of the atmosphere in photochemical equilibrium, where ozone destruction is favored by the warmer temperature. The colder temperature enhances the formation of ozone by recombination of available oxygen atoms with molecular oxygen. This conclusion is based on the assumption of a constant source of atomic oxygen at these altitudes. The latitudinal differences in the diurnal variation of the ozone distributions as well as the results from the polar night measurements imply a fairly strong horizontal and seasonal variation of atomic oxygen and water vapor in the mesosphere.

3.7 Results - Atomic Oxygen Sounding

The first flight of the atomic oxygen experiment discussed here was performed at Wallops Island, Va. on a Nike Cajun sounding rocket in October, 1970. Figure 3.7.1 shows the results of this flight compared to theoretical models. Though this first flight yielded data from only 88-95 km, future flights will extend measurements to a height range of 75 to 120 km. Measurements of oxygen atoms in this altitude region are important to determine the state of the mesosphere and lower thermosphere because of the wide range of characteristic time constants (or residence times) for oxygen atoms, i. e. , from less than one day

at the lower altitudes to months at altitudes above 110 km. These measurements would then yield information on the photochemical processes as well as the dynamics of this part of the atmosphere. Since only one set of data has been obtained, it would be premature to make any definitive conclusions on the results of this experiment, except that the results are consistent with models that include molecular and eddy diffusion and turbulent mixing, but not with those that assume steady state conditions. Therefore inferences concerning the large scale dynamics in this altitude range, such as the nature of meridional flow from the summer pole to winter pole near the mesopause, will be difficult. Oxygen atom data will also be applicable to the description of phenomena in the ionosphere such as D and E region anomalies, since they both most likely involve neutralization of atomic oxygen atoms.

3.8 Long Term Variations of Solar UV Energy Inputs to the Mesosphere

Variations of solar UV radiation have been derived from the three UV sensors which were common to a rocket flight in 1966, and the NIMBUS 3 and 4 MUSE experiments during 1969, and 1970, respectively. The MUSE sensor response distributions functions are shown in Figure 3.8.1. The response distribution function at any wavelength represents the fraction of the sensor output which comes from shorter wavelengths.

There are three types of solar UV variations which have been observed: those related to the long term or solar cycle variation; those related to the solar rotation period; and those associated with flare activity. They are listed in order of decreasing magnitude.

3.8.1 Solar Cycle Variations

Significant variations of solar irradiance were observed in accordance with the 11 year solar cycle (minimum 1964, maximum late 1968). The best demonstration of this variation is found in the 1750 \AA radiation which originates near the region of solar temperature minimum. In August, 1966, the solar irradiance observed by the sensor at 1750 \AA was only 41 percent of that observed in April, 1969; by April, 1970, the irradiance had decreased to 76 percent of the 1969 value. Such variation should produce significant changes in the production rate of atomic oxygen in the lower thermosphere-upper mesosphere region. A discussion of the importance of dissociation in the tail of the Schumann-Runge continuum and predissociation of the vibrational levels at wavelengths shorter than 1972 \AA has been given in detail by Hudson, et al. (1969).

An increase in the production rate of atomic oxygen in the mesosphere-lower thermosphere region without a corresponding change in the photodissociation rate of O_3 leads to an increase in the amount of ozone. There is some experimental evidence that this may be taking place. Gattinger and Jones (1966) observed a fourfold decrease in the twilight brightness of the $0, 1$ band of the $\text{O}_3, {}^1\Delta_g - {}^3\Sigma_g$ system between 1960 and 1964. One of the theories for the production of $\text{O}_2 ({}^1\Delta_g)$ is via the photodissociation of O_3 in the Hartley continuum. Additional experimental evidence has been given by Paetzold (1961b) who reported a small enhancement in the amount of ozone above 35 km which was greater in 1958 than in 1952, and which showed a small positive correlation with sunspot numbers and the decimeter solar radio flux.

3.8.2 27-Day Variability

The most unambiguously observed type of UV variability is that associated with the 27-day solar rotational period. These variations are easily observed since the amount of sensor degradation which occurs in the 27-day period is practically negligible.

If the slowly varying exponential decay factors are removed from the MUSE photometer measurements, and corrections are made for the variable earth sun distance, one obtains the curves of Figure 3.8.2 showing the 27-day solar UV variability. The curves labeled A, B, and C refer to sensors whose response functions are shown in Figure 3.8.1. Each data point represents a daily average of one to eight observations per day at the terminator. In this figure, the long term trends of the curves over a period of a year are due to the way in which the exponential decay factors were removed. However, the following significant factors inherent in the solar UV flux are clearly evident in Figure 3.8.2:

1. Two UV flux maxima per solar rotation are observed.
2. The magnitude of UV flux variation decreases with increasing wavelengths.
3. The UV flux variation per rotation is decreasing with time.
4. The UV flux variations correlate with other indicators of solar activity.

Three indicators of solar activity are shown below the MUSE measurements. The 8-20 Å x-ray flux background (flare enhancements removed)

is from the experiment on Explorer 37 of R. Kreplin of the U.S. Naval Research Laboratory. The values for the daily ΣK_p and the 10.7 cm solar flux are taken from "Solar-Geophysical Data" of the Environmental Data Service NOAA. Active solar regions producing enhancements in the 8-20 Å X-ray flux and the 10.7 cm radio flux are definitely related to the UV enhancements. In addition, it appears that some relationship does exist between the solar wind related perturbations of the geomagnetic field through K_p . Increases to values greater than 40 frequently follow 0-3 days after a UV maximum, which sometimes does not correlate well with the other solar activity indicators.

The UV maxima and minima correlate better with the 10.7 cm radiation than with the calcium plage area or the Zurich provisional mean sunspot numbers. Similarly, Timothy and Timothy (1970) have observed that the correlation between the EUV helium II Lyman- α line at 304 Å with the standard indicators of solar activity is poor. For the MUSE experiment, the correlation is much worse for the longer wavelength sensors (B) and (C).

The percentage variation of solar irradiance versus wave number (cm^{-1}) is shown in Figure 3.8.3 for the spectral region spanned by sensors A and C. No scientific justification is proposed for the logarithmic relation between percentage variation and wave number.

It can be seen in Figure 3.8.2 that two UV maxima per solar rotation are frequently observed from sensors A and B. A graph of the Carrington longitude of the central meridian on the days of the UV flux maxima is presented

in Figure 3.8.4 which covers a period of 28 solar rotations. The UV maxima can be determined with an accuracy of about ± 1 day or ± 13 degrees in longitude. Two distinct phenomena are observed. The UV maxima appear to originate from two UV active regions, as seen by the clustering of the points about two straight lines. The regions have persisted through 28 solar rotations, and they have been observed by the MUSE experiments on NIMBUS 3 and 4. The longitude of the strongest or primary feature is indicated by (x) whereas the secondary region is described by (o). At the time of launch of NIMBUS 3, the two regions were separated in longitude by 225 degrees, and 28 rotations later, the separation had decreased to 190 degrees. If one uses $13.199 \text{ degrees}^{-1} \text{ day}$ as the rotation rate of the Carrington longitude, then the rotation rate of the primary UV active region is $13.14 \text{ degrees day}^{-1}$, while that of the secondary one is $13.11 \text{ degrees day}^{-1}$.

The time dependence of the variations of the UV irradiances (sensor A) per solar rotation are given in Figure 3.8.5 for the two regions shown in Figure 3.8.4. The primary region peaked during solar rotation 1548 while the secondary one appears to have reached a maximum around rotation number 1557.

Evidence for the existence of persistent zones of activity on opposite sides of the sun has been presented by Dodson (1970) and Bumba (1970). In general, the active regions appear to be better defined in the UV. Also, there is an approximate agreement as to strength and longitude of the active regions as determined from ground based and satellite UV measurements.

3.8.3 Flare UV Variability

On April 21, 1969, at 1959 UT, a major optical flare of optical importance 3B, small class X was recorded. The response of the solar UV flux measured with the MUSE experiment to this flare is shown in Figure 3.8.6. The ordinate is the sensor current normalized to the value at the terminator on orbit 101. The function $f(\phi)/\cos\phi$ represents the sensor response function to changing angles of illumination of the photocathode. The flare occurred during orbit 102, 15 frames or 12 minutes prior to the sun appearing in the field-of-view. Only the shortest wavelength channel showed any flare enhancement. If an exponential decay for the flare radiation is assumed, then this leads to an enhancement of 16 percent above the pre and post flare values of solar radiation which produces the signals in the shortest wavelength channels. Based on the sensor response functions given in Figure 3.8.1, the enhancement shown for sensor A should be due principally to H, Ly- α .

References

- Ainsworth, J. E. , D. F. Fox, and H. E. LaGow, "Upper Atmosphere Structure Measurement Made with the Pitot-Static Tube," J. Geophys. Res. , 66 (10), 3191-3211, 1961.
- Badinov, I. Y. , S. D. Andreyev, V. B. Lipatov, "Measurements of Humidity in the Upper Atmosphere," in izdatel'stvo Nauka, Moscow, pp. 66-79, 1966. (NASA Tech. Trans. F10, 303).
- Ballard, Harold N. , and Bryan Rofo, "Thermistor Measurement of Temperature in the 30-65 km Atmospheric Region," Stratospheric Circulation, ed. by Willis L. Webb, Academic Press, New York, 141-166, 1969.
- Beach, C. J. , "A Rocket-borne Photometric Ozone and Temperature Measuring Sonde," Australian Defense Scientific Service, WRE Note HSA 179, 1970.
- Beranose, H. J. , and M. G. Rene, "Oxyluminescence of a Few Flourescent Compounds of Ozone," Ozone Chemistry and Technology, Advances in Chem. Sci. , 21, 7-12, 1959.
- Beyers, Norman J. , "Radar Chaff as a Wind Sensor," Stratospheric Circulation, ed. by Willis L. Webb, Academic Press, New York, 89-96, 1969.
- Bumba, V. , "Large-Scale Magnetic Field and Activity Patterns on the Sun," Leningrad Symposium, IUCSTP, May 1970 (in press).
- Carver, J. H. , B. H. Horton, F. G. Burger, "Nocturnal Ozone Distribution in the Upper Atmosphere," J. Geophys. Res. , 71, 4189-4191, 1966.
- Charlson, R. J. , "Noctilucent Clouds: A Steady-State Model," Quart. J. Roy. Met. Soc. , 91, 517-523, 1965.

- Chahine, M. T. , "Determination of the Temperature Profile in an Atmosphere from its Outgoing Radiance," J. Opt. Soc. Am. , 58, 1634, 1968.
- Chleck, "Aluminum Oxide Hygrometer, Laboratory Performance," J. Appl. Meteorol. , 5, (878-885), 1966.
- COESA, (Committee on Extension of the Standard Atmosphere), U.S. Standard Atmosphere, 1962, U.S. Government Printing Office, Washington, D.C. , 1962.
- COESA, U.S. Standard Atmosphere Supplement, 1966, U.S. Government Printing Office, Washington, D.C. , 1966.
- Conrath, B. J. , R. A. Hanel, V. G. Kunde, and C. Prabhakara, "The Infrared Interferometer Experiment on Nimbus 3," J. of Geophys. Res. , 75, (30), pp. 5831-5857, 1970.
- Conrath, B. J. , "Inverse Problems in Radiative Transfer: A Review," Proceedings of the XVIIIth International Astronautical Congress, edited by M. Junc, 339, 1968.
- Dodson, H. W. , "Comments on Large Scale Organization of Solar Activity in Time and Space," AIAA Bulletin, 7, 563, 1970.
- Dutsch, H. U. , "Atmospheric Ozone and Ultraviolet Radiation," Climate of the Free Atmosphere, 4, Ed. by D. F. Rex, 383-432, 1969.
- Ellis, P. J. , G. Peckham, S. D. Smith, J. T. Houghton, C. G. Morgan, C. D. Rodger, and E. J. Williamson, "First Results from the Selective Chopper Radiometer on Nimbus 4," Nature, 228, (5267), 139-143, 1970.

- Fogle, Benson, "Noctilucent Clouds," Report UAG R-177, Geophysical Inst., Univ. of Alaska, College, 34-66, 1966.
- Fritz, S., and S. D. Soules, "Large-Scale Temperature Changes in the Stratosphere Observed from Nimbus III," J. Atmos. Sci., 27, (7), 1091-1097, 1970.
- Gattinger, R. L., and Jones, A. V., "The $^1\Delta_g - ^3\Sigma_g^-$ O_2 Bands in the Twilight and Day Airglow," Planet. Space Sci., 14, 1, 1966.
- Heath, D. F., "Observations of Solar Long Term Variability and Irradiance in the Near and Far Ultraviolet," GSFC X-651-71-116, NASA Goddard Space Flight Center, Greenbelt, Maryland, 1971.
- Hedin, A. E., C. P. Avery, and C. D. Tschetter, "An Analysis of Spin Modulation Effects on Data Obtained with Rocket Borne Mass Spectrometer," J. Geophys. Res., 69, 4637, 1964.
- Hemenway, C. L., E. F. Fullum, R. A. Skrivanek, R. K. Soberman, and G. Witt, "Electron Microscope Studies of Noctilucent Cloud Particles," Tellus, 9, 96-102, 1964.
- Henderson, W. R., and H. I. Schiff, "A Simple Sensor for the Measurement of Atomic Oxygen Height Profiles in the Upper Atmosphere," Planet. Space Sci., 18, 1527-1534, 1970.
- Henderson, W. R., "D-Region Atomic Oxygen Measurement," J. Geophys. Res., 76, (13), 1971.

- Hering, W. S., and T. R. Borden, Jr., "Mean Distributions of Ozone Density Over North America, 1963-1964," U.S.A.F., Office of Aero-space Research, Environmental Res. Papers No. 162, Air Force Cambridge Res. Lab., Bedford, Mass., 19 pp., 1965.
- Hesstvedt, E., "On the Water Vapor Content of the High Atmosphere," *Geofys. Publ.* Oslo, 25, 1-18, 1964.
- Hesstvedt, E., "On the Possibility of Ice Cloud Formation at the Mesopause," *Tellus*, 14, 290-296, 1962.
- Hesstvedt, E., "On the Effect of Vertical Eddy Transport on Atmospheric Composition in the Mesosphere and Lower Thermosphere," *Geofys. Publ.*, 27, 1-35, 1968.
- Hilsenrath, E., L. Seiden, and P. Goodman, "An Ozone Measurement in the Mesosphere and Stratosphere by Means of Rocket Sonde," *J. Geophys. Res.*, 74, 6873-6879, 1969.
- Hilsenrath, E., "Ozone Measurements in the Mesosphere and Stratosphere During Two Significant Geophysical Events," *J. Atm. Sci.*, 28, 295-297, 1971.
- Hilsenrath, E., and R. Coley, "Performance of an Aluminum Oxide Hygrometer on the NASA CV-990 Aircraft Meteorological Observatory," GSFC Document X-651-71-37, NASA Goddard Space Flight Center, Greenbelt, Maryland, 1971.
- Hines, C. O., "Internal Atmospheric Gravity Waves at Ionospheric Heights," *Can. Journ. Phys.*, 38, 1441-1481, 1960.

- Hines, C. O., and C. A. Reddy, "On the Propagation of Atmospheric Gravity Waves through Regions of Wind Shear," J. Geophys. Res., 72, 1015-1034, 1967.
- Horvath, J. J., R. W. Simmons, and L. H. Brace, "Theory and Implementation of the Pitot-Static Technique for Upper Atmospheric Measurements," Univ. of Michigan Scientific Report NS-1, Ann Arbor, Mich., 1962.
- Hudson, R. D., Carter, V. L., and Breig, E. L., "Predissociation in the Schumman-Runge Band System of O_2 : Laboratory Measurements and Atmospheric Effects," J. Geophys. Res., 74, 4079, 1969.
- Humphreys, W. J., "Nacreous and Noctilucent Clouds," Mon. Wea. Rev., 61, 228, 1933.
- Hunt, B. G., "Photochemistry in a Moist Atmosphere," J. Geophys. Res., 71, 1385-1398, 1966.
- Iozenas, V. A., V. A. Krasnopol'skiy, A. P. Kuznetsov, and A. I. Lebedinskiy, "Studies of the Earth's Ozonosphere from Satellites," Izv., Atmos. and Oceanic Phys., 5, 77-82, 1969.
- Johnson, F. S., J. D. Purcell, R. Tousey, and K. Watanabe, "Direct Measurements of the Vertical Distribution of Atmospheric Ozone to 70 km Altitude," J. Geophys. Res., 57, 157-176, 1952.
- Kaplan, L. D., "Inference of Atmospheric Structure from Remote Radiation Measurements," J. Opt. Soc. Am., 49, 1004, 1959.
- Keneshea, T. J., and S. P. Zimmerman, "The Effect of Mixing Upon Atomic and Molecular Oxygen in the 70-170 km Region of the Atmosphere," J. Atmos. Sci., 27, 831-1970.

- Kennedy, J. S. , "An Atlas of Stratospheric Mean-Isotherms Derived from TIROS VII Observations," NASA X-622-66-307, Goddard Space Flight Center, Greenbelt, Maryland, 1966.
- Kennedy, J. S. , and W. Nordberg, "Circulation Features of the Stratosphere Derived from Radiometric Temperature Measurements with the TIROS VII Satellite," J. Atmos. Sci. , 24, (6), 711-719, 1967.
- King, J. I. F. , "The Radiative Heat Transfer of Planet Earth," Scientific Uses of Earth Satellites, Second Ed. , ed. by J. A. Van Allen, Univ. of Mich. Press, 316 pp. , 1958.
- Khvostikov, I. A. , "Present State of the Problem of Noctilucent Clouds," in Izdatel'stvo Nauka, Moscow, pp. 5-10, 1966. (NASA Tech. Trans. F10, 301).
- Krueger, A. J. , and W. R. McBride, "Sounding Rocket - OGO-4 Satellite Ozone Experiment: Rocket Ozonesonde Measurements," NWC TP4667, Naval Weapons Center, China Lake, Calif. , 1968.
- Leovy, C. , "Simple Models of Thermally Driven Mesospheric Circulation," J. Atmos. Sci. , 21, 327-341, 1964.
- Lindzen, R. S. , "Thermally Driven Diurnal Tides in the Atmosphere," Quart. J. Roy. Met. Soc. , 93, 18-42, 1967.
- Ludlam, F. H. , "Noctilucent Clouds," Tellus , 9, 341-364, 1957.
- Mateer, C. L. , D. F. Heath, and A. J. Krueger, "Estimation of Total Ozone from Satellite Measurements of Backscattered Ultraviolet Earth Radiance," J. Atmos. Sci. , (to be published), 1971.

- Mateer, C. L., "On the Information Content of Umkehr Observations," J. Atmos. Sci., 22, 370-381, 1965.
- Mateer, C. L., "Retrieval of Atmospheric Parameters from Shortwave Radiation Measurements," Proceedings of Workshop on the Mathematics of Profile Inversion, NASA-AMES Research Center, July 1971. To be published.
- Murgatroyd, R. J., "Winds and Temperatures between 20 km and 100 km — A Review," Quart. J. Roy. Met. Soc., 83, 417-458, 1957.
- Nagata, T., T. Tohmatsu, and T. Ogawa, "Sounding Rocket Measurement of Atmospheric Ozone Density, 1965-70," COSPAR, Leningrad, May 1970.
- Nimbus II Data User's Guide, National Space Science Data Center, Goddard Space Flight Center, Greenbelt, Md., 73-91, 1966.
- Nimbus III User's Guide, National Space Science Data Center, Goddard Space Flight Center, Greenbelt, Md., 1969.
- Nimbus IV User's Guide, National Space Science Data Center, Goddard Space Flight Center, Greenbelt, Md., March 1970.
- Nordberg, W., A. W. McCulloch, L. L. Foshee, and W. R. Bandeen, "Preliminary Results from Nimbus II," Bul. Amer. Met. Soc., 47, (11), 1966.
- Nordberg, W., and S. I. Rasool, "Introduction to Space Science," Ed. W. N. Hess and G. D. Mead, Gordon & Breach, New York, 1968.
- Nordberg, W., and W. Smith, "The Rocket Grenade Experiment," NASA Tech. Note TND-2107, 1964.

- Obukhov, A. M. , "The Statistically Orthogonal Expansion of Emperical Functions," *Izvestiya, Seriya Geoficizicheskaya*, Akad. Nauk SSR, 3, 432, 1960.
- Paetzold, H. K. , "The Photochemistry of the Atmospheric Ozone Layer, Chemical Reactions in the Lower and Upper Atmosphere," *Interscience Pub.* , 181, 1961b.
- Paetzold, H. K. , "Messungen des Atmosphärischen Ozone," *Handbook der Aerologie*, ed. by W. Hesse, Leipzig, Akademische Verlagsgesellschaft, 458-531, 1961a.
- Paton, J. , "Noctilucent Clouds," *Met. Mag.* , London, 93, 161-179, 1964.
- Prabhakara, C. , "Feasibility of Determining Atmospheric Ozone from Outgoing Infrared Energy," *Mon. Wea. Rev.* , 97, 1969.
- Prabhakara, J. , B. J. Conrath, L. J. Allison, J. Steranka, "Seasonal and Geographic Variation of Atmospheric Ozone Derived from Nimbus 3," GSFC Document X-651-71-38, pp. 75, Goddard Space Flight Center, Greenbelt, Md. , 1971.
- Reed, E. I. , "A Night Measurement of Mesospheric Ozone by Observations of Ultraviolet Airglow," *J. Geophys. Res.* , 73, 2951, 1968.
- Rodgers, C. D. , "Satellite Infrared Radiometer; A Discussion of Inversion Methods," *Univ. of Oxford, Clarendon Lab. Mem.* 66.13, 25 pp. , 1966.
- Shimazaki, T. , and A. R. Laird, "A Model Calculation of the Diurnal Variation in Minor Neutral Constituents in the Mesosphere and Lower Thermosphere Including Transport Effects," *J. Geophys. Res.* , 75, 3221, 1970.

Sissons, N. V. , "Ozone Measuring Techniques and Their Assessment for W.

R. E. Dropsonde Use," Australian Defense Scientific Service, WRE Note
SAD 196, 1968.

Smith, W. L. , "Statistical Estimation of the Atmosphere's Geopotential Height
Distribution from Satellite Radiation Measurements," ESSA Tech. Report
NESC 48, 1969.

Smith, W. S. , L. B. Katchen, and J. S. Theon, "Grenade Experiments in a
Program of Synoptic Meteorological Measurements," in Meteorological
Investigations of the Upper Atmosphere, ed. by R. S. Quiroz, Meteorologi-
cal Monographs of the AMS, 9, (31) 170-175, 1968b.

Smith, W. S. , J. S. Theon, P. C. Swartz, J. F. Casey, and J. J. Horvath,
"Temperature, Pressure, Density, and Wind Measurements in the Strato-
sphere and Mesosphere, 1967," NASA Tech. Report TR R-316, 1969.

Smith, W. S. , J. S. Theon, J. F. Casey, and J. J. Horvath, "Temperature,
Pressure, Density, and Wind Measurements in the Stratosphere and Meso-
sphere, 1968," NASA Tech. Report TR R-340, 1970.

Smith, W. S. , J. S. Theon, J. F. Casey, A. Azcarraga, and J. J. Horvath,
"Temperature, Pressure, Density, and Wind Measurements in the Strato-
sphere and Mesosphere, 1969," NASA Tech. Report TR R-360, 1971.

Smith, W. , L. Katchen, P. Sacher, P. Swartz, and J. Theon, "Temperature,
Pressure, Density, and Wind Measurements with the Rocket Grenade Ex-
periment, 1960-63," NASA Tech. Report TR R-211, 1964.

- Smith, W. , J. Theon, L. Katchen, and P. Swartz, "Temperature, Pressure, Density, and Wind Measurements in the Upper Stratosphere and Mesosphere, 1964," NASA Tech. Report TR R-245, 1966.
- Smith, W. S. , J. S. Theon, P. C. Swartz, L. B. Katchen, and J. J. Horvath, "Temperature, Pressure, Density, and Wind Measurements in the Upper Stratosphere and Mesosphere, 1965," NASA Tech. Report TR R-263, 1967.
- Smith, W. S. , J. S. Theon, P. C. Swartz, L. B. Katchen, and J. J. Horvath, "Temperature, Pressure, Density, and Wind Measurements in the Stratosphere and Mesosphere, 1966," NASA Tech. Report TR R-288, 1968a.
- Strand, O. N. , and E. R. Westwater, "Minimum rms Estimation of the Numerical Solution of a Fredholm Integral Equation of the First Kind," SIAM J. Numerical Analysis, 5, 287, 1968.
- Theon, J. S. , "Short Term Temperature Variations in the Atmosphere Below 120 km," Proceed. Third Nat'l Conf. on Aerospace Meteorology, New Orleans, 449-456, May 1968.
- Theon, J. S. , W. S. Smith, J. F. Casey, and B. R. Kirkwood, "The Mean Observed Structure and Circulation of the Upper Atmosphere," To be published as NASA Tech. Report, 1971.
- Theon, J. S. , W. Nordberg, and W. S. Smith, "Temperature Measurements in Noctilucent Clouds," Science, 157, (3787), 419-421, 1967.

- Theon, J. S. , and W. S. Smith, "The Meteorological Structure of the Mesosphere Including Seasonal and Latitudinal Variations," Proceed. of the Fourth ESRIN-ESLAB Symp. on Upper Atmospheric Models and Related Expts. , Frascati, Italy, July 1970, D. Reidel Publ. Co. , Dordrecht, Holland.
- Theon, J. S. , W. S. Smith, and J. F. Casey, "Statistical Models of the Density and Wind Profiles in the Mesosphere Based on 208 Soundings," Proceed. of the AMS Fourth Natl. Conf. on Aerospace Meteorology, 306-311, Las Vegas, Nev. , May 1970.
- Timothy, A. F. , and Timothy, J. G. , "Long-Term Intensity Variations in the Solar Helium II Lyman Alpha Line," J. Geophys. Res. , 6950, 1970.
- TIROS VII Radiation Data Catalog & User's Manual, Vol. I, Goddard Space Flight Center, Greenbelt, Md. , 256 pp. , 1964.
- Twomey, S. , "The Application of Numerical Filtering to the Solution of Integral Equations Encountered in Indirect Sensing Measurements," J. Franklin Inst. , 279, 95-109, 1965.
- Twomey, S. , "Indirect Measurements of Atmospheric Temperature Profiles from Satellites. II. Mathematical Aspects of the Inversion Problem," Mon. Wea. Rev. , 94, 363-366, 1966.
- Wark, D. Q. , and H. E. Fleming, "Indirect Measurements of Atmospheric Temperature Profiles from Satellites," Mon. Wea. Rev. , 94, 351, 1966.

- Wark, D. Q., and D. T. Hilleary, "Atmospheric Temperature: Successful Test of Remote Probing," Science, 165, 1256, 1969.
- Warnecke, G., and Andrew W. McCulloch, "Stratospheric Temperature Patterns Derived from Nimbus II Measurements," GSFC Documents X-622-67-436, Goddard Space Flight Center, Greenbelt, Md., 1967.
- Warner, J., and E. G. Bowen, "A New Method of Studying the Fine Structure of Air Movements in the Free Atmosphere," Tellus, 5, 36-41, 1953.
- Weeks, L. H., and L. G. Smith, "A Rocket Measurement of Ozone Near Sunrise," Planet. Space Sci., 16, 1189-1195, 1968.
- Wei, Ding-wen, "The Non-uniqueness of the Solution for the Vertical Distributions of Ozone from the Calculation by the Umkehr Method B.," Acta Geophys. Sinica, 11, 123-135 (in Chinese); English summary 1963, Scientia Sinica, XII, 1065-1070.
- White, W. C., and A. J. Krueger, "Shipboard Observations of Total Ozone from 38°N to 60°S," J. Atmos. Terres. Phys., 30, 1615-1622, 1968.
- Witt, G., J. Martin-Lof, N. Wilhelm, W. S. Smith, Space Research ed. by D. G. King-Hele, P. Muller, G. Righini, North-Holland, Amsterdam, 5, 820, 1965.
- Wright, John B., "The Robin Falling Sphere," Stratospheric Circulation, ed. by Willis L. Webb, Academic Press, New York, 115-139, 1969.

Table 3.1.1. Number of Soundings Included in Each Mean

Model Atmosphere											
Site	Winter			Summer			Spring/Fall			Annual	
	Dec	Jan	Feb	Jun	Jul	Aug	Mar	Apr	May	Jan thru	Dec
							Sep	Oct	Nov		
Natal-Ascension											
(6-8°S)	—			—						34	
Wallops											
(38°N)	28			24				41		—	
Churchill											
(59°N)	29			12				13		—	
Barrow											
(71°N)	19			17				10		—	

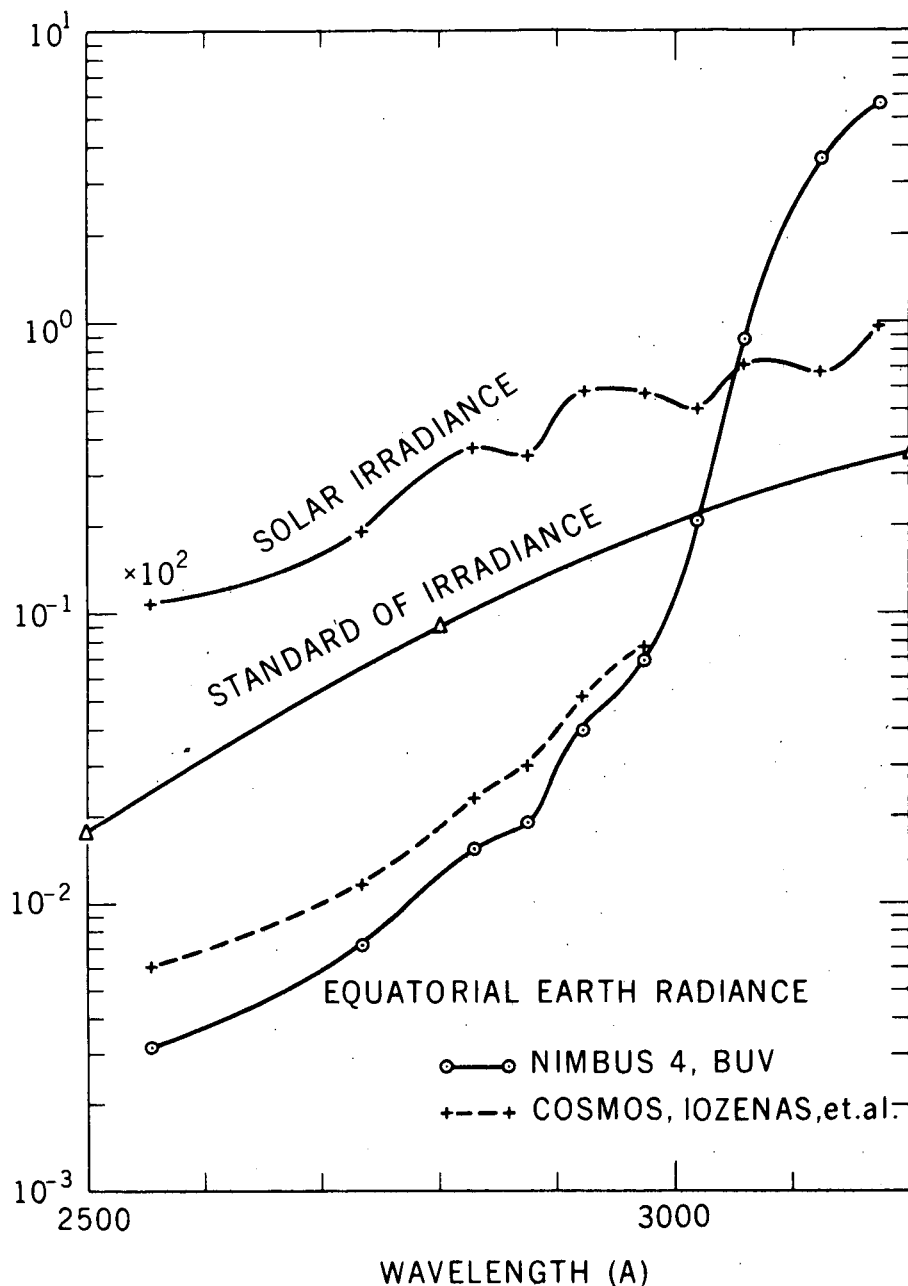


Figure 2.2.3.1. Wavelength dependence of solar irradiance, laboratory standard of irradiance, and radiance backscattered from the Earth at the Equator. The units of irradiance are $\text{ergs cm}^{-2} \text{sec}^{-1} \text{\AA}^{-1}$ and radiance, $\text{ergs cm}^{-2} \text{sec}^{-1} \text{\AA}^{-1} \text{sterad}^{-1}$. The ordinate should be multiplied by 10^2 to read solar irradiance. The Earth radiance measured by Iozenas, et al. (1969) on the Cosmos satellites is shown for comparison with the NIMBUS BUV measurements. Both measurements are from the equatorial regions where the polarization is essentially zero. The agreement is quite good at the long wavelength end; however, at 2555\AA , the USSR measurement of the Earth radiance is larger by about a factor of two. We believe that this discrepancy could be due to stray light originating in the USSR instrument.

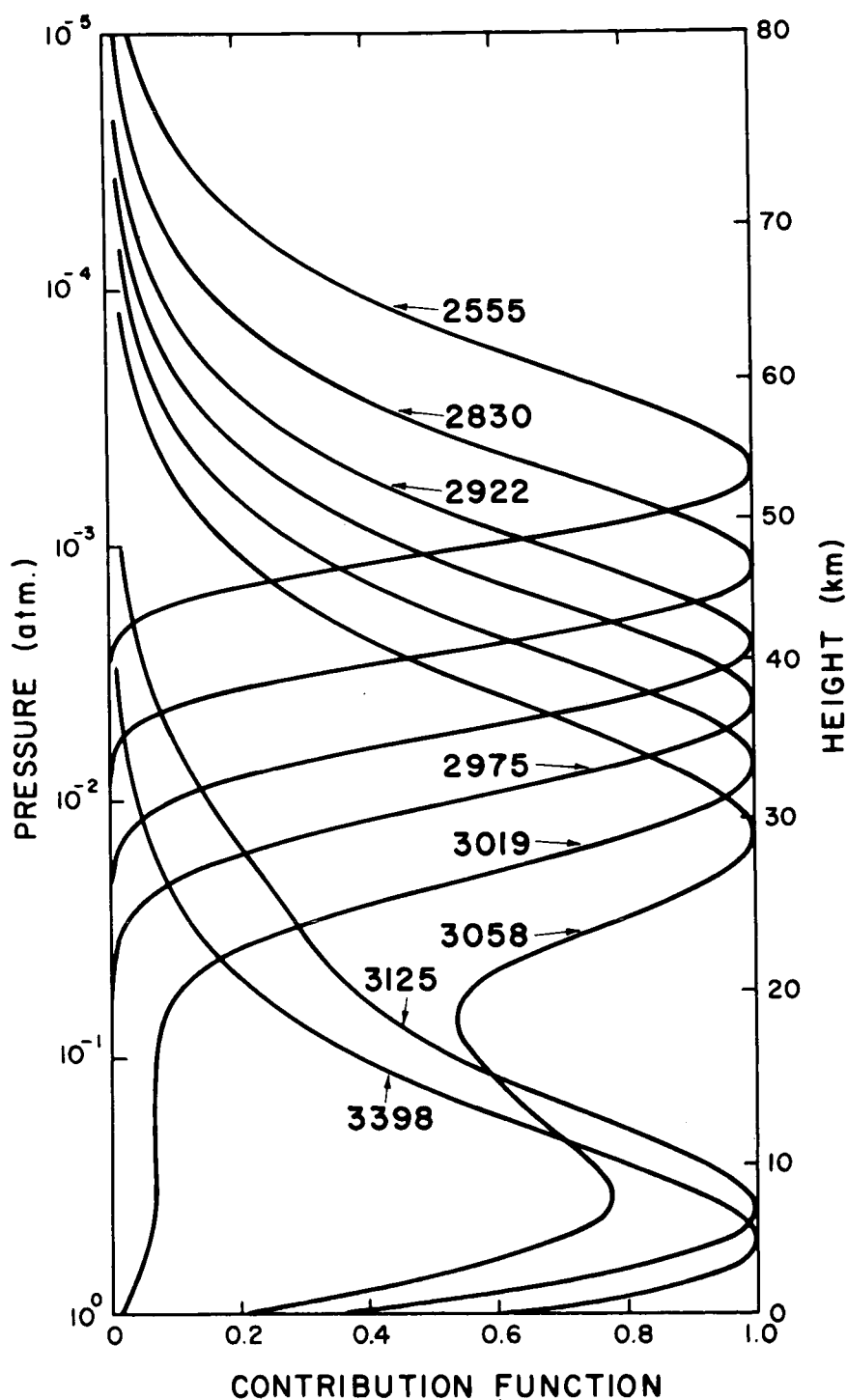


Figure 2.2.3.2. Contribution to the backscattered radiation from various levels in the atmosphere. Each curve is normalized to unity at level of maximum. (Surface reflectivity = 0, solar zenith angle = 60 degrees, nadir angle of observation = 0 degree, total ozone = 0.336 atm-cm.)

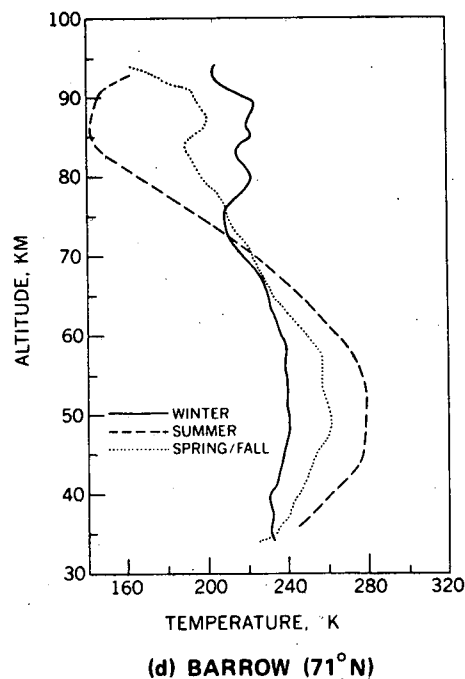
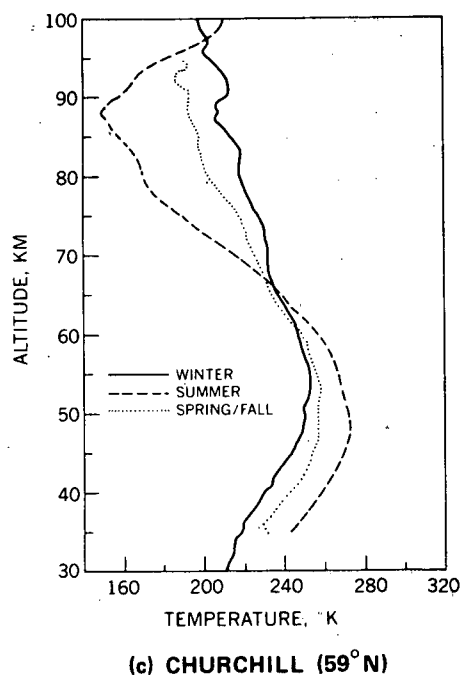
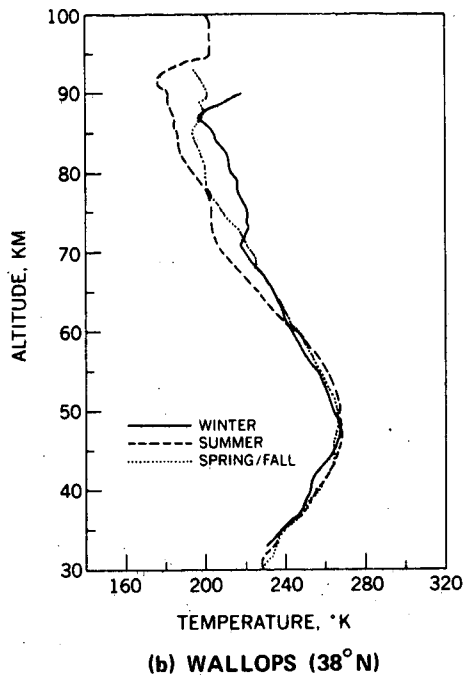
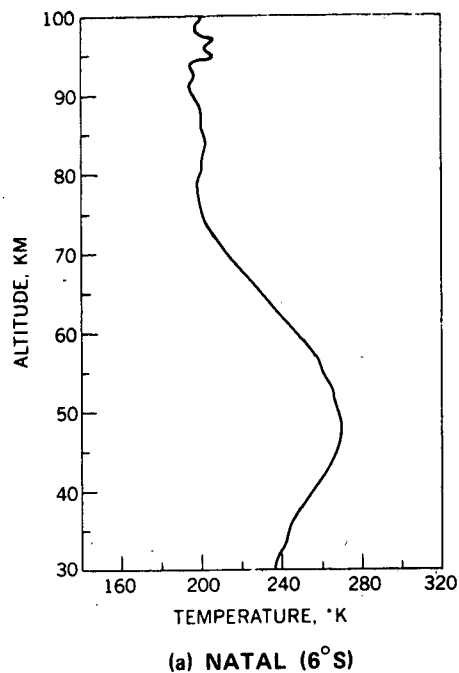


Figure 3.1.1. Mean annual temperature profile for Natal-Ascension Island (6 S-8 S) based on 34 soundings (a), mean seasonal temperature profiles for Wallops Island (38 N) based on 28 winter, 24 summer and 41 transition soundings (b), for Churchill (59 N) based on 29 winter, 12 summer and 13 transition soundings (c), and for Barrow (71 N) based on 19 winter, 17 summer, and 10 transition soundings (d) (after Theon, et al., 1971).

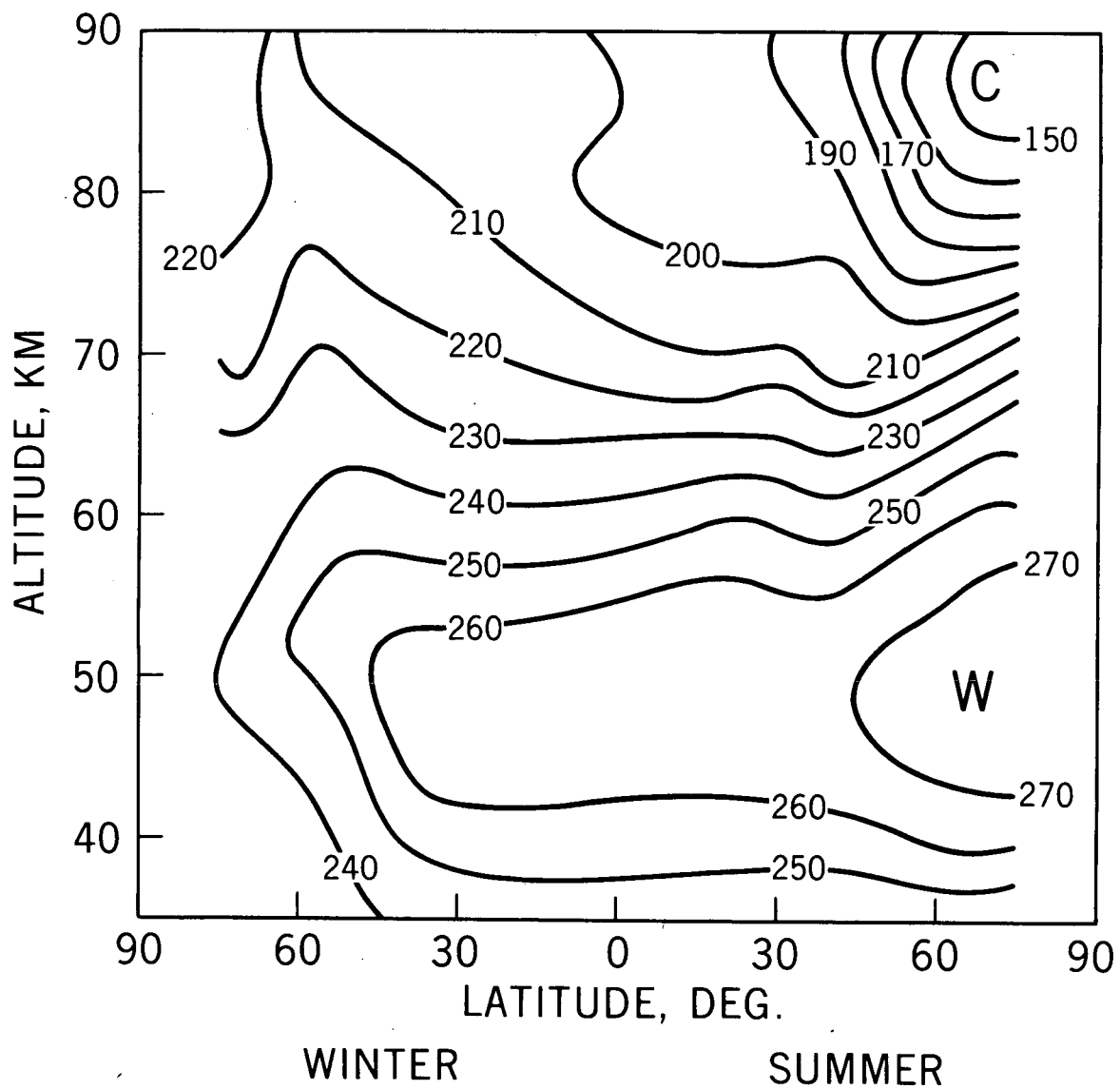


Figure 3.1.2. A quasi-meridional cross-section of temperature in degrees K derived from mean profiles in Figure 3.1.1 (after Theon and Smith, 1970):

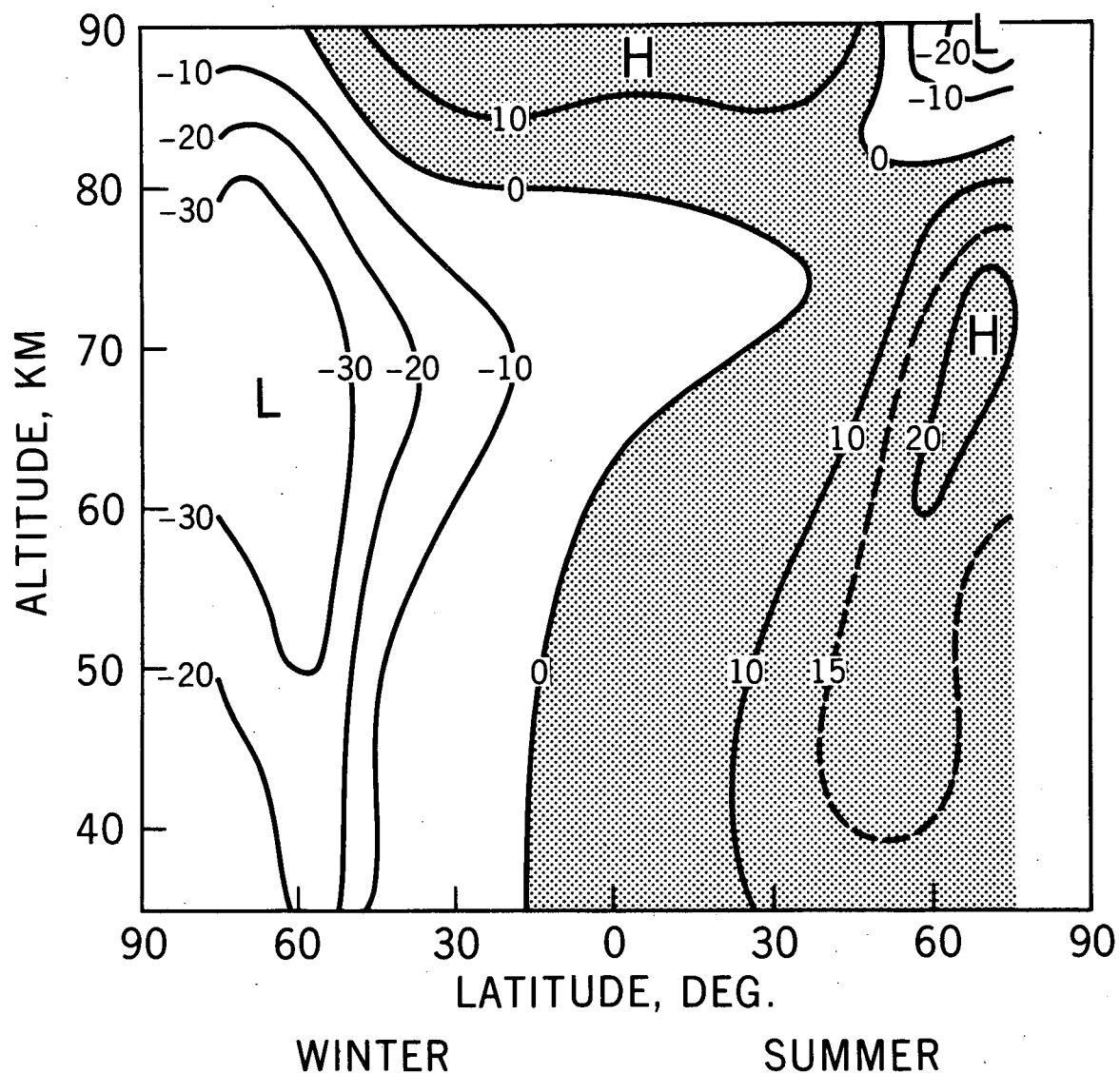
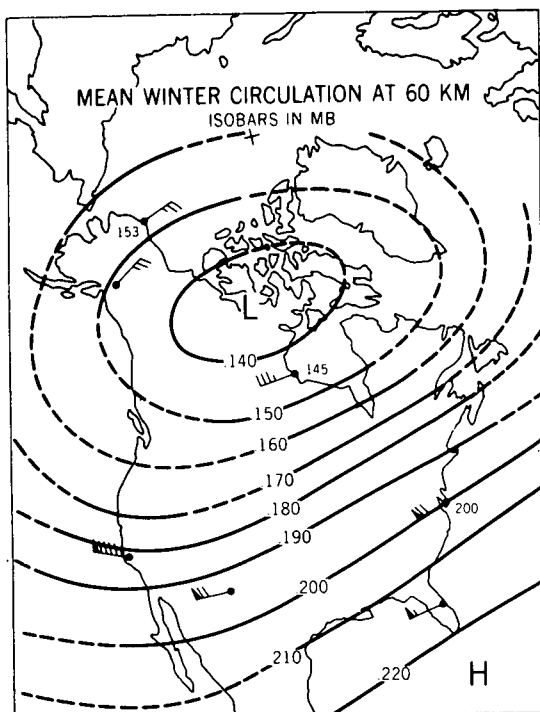
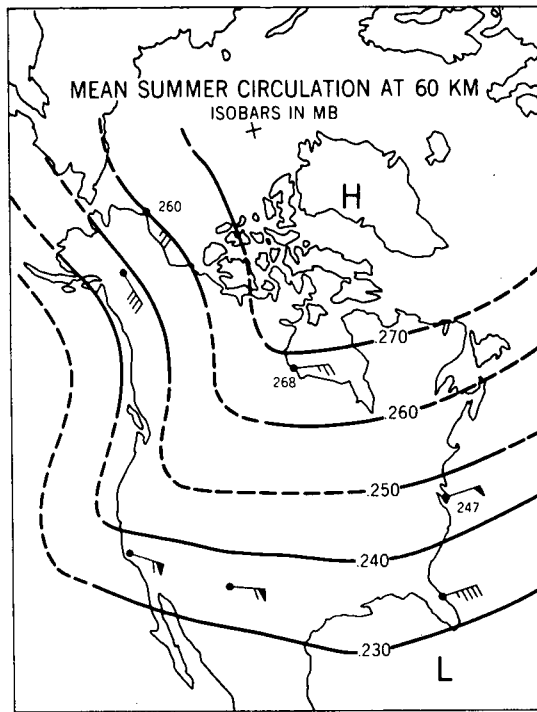


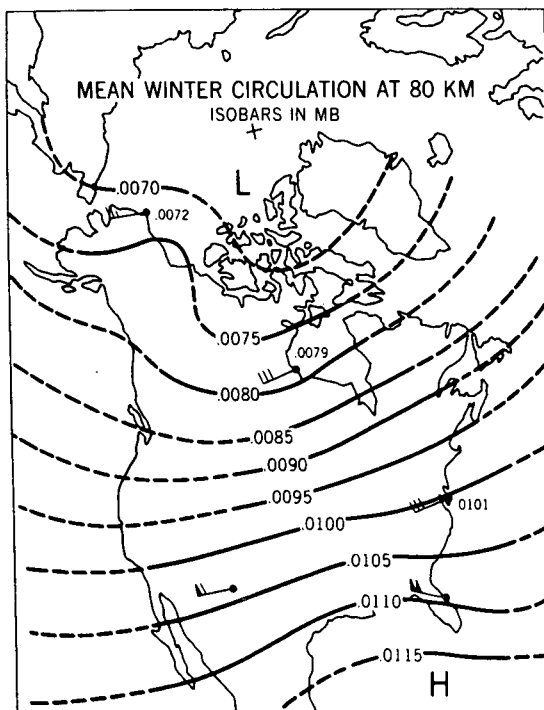
Figure 3.1.3. A quasi-meridional cross-section of pressure as percent difference from the U.S. Standard Atmosphere 1962, derived from mean profiles in Figure 3.1.1 (after Theon and Smith, 1970).



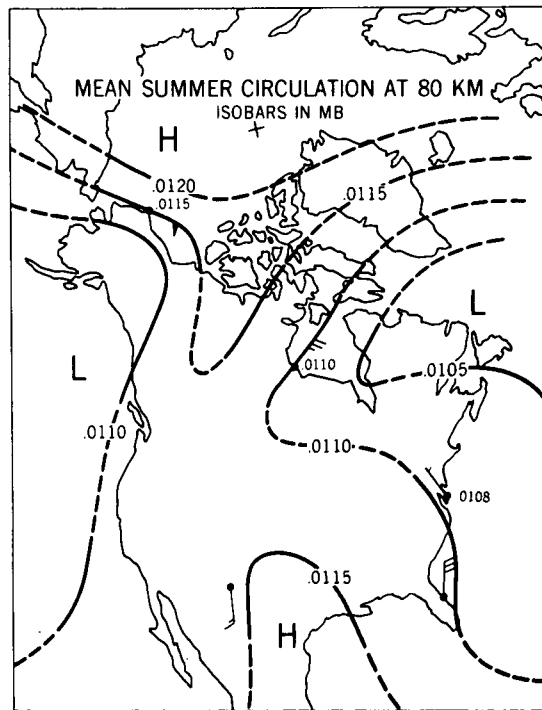
(a)



(b)



(c)



(d)

Figure 3.1.4. Mean winter circulation at 60 km (a), and 80 km (c) and mean summer circulation at 60 and 80 km (b and d respectively). Isobars are given in mb, wind in m sec^{-1} (after Theon and Smith, 1970).

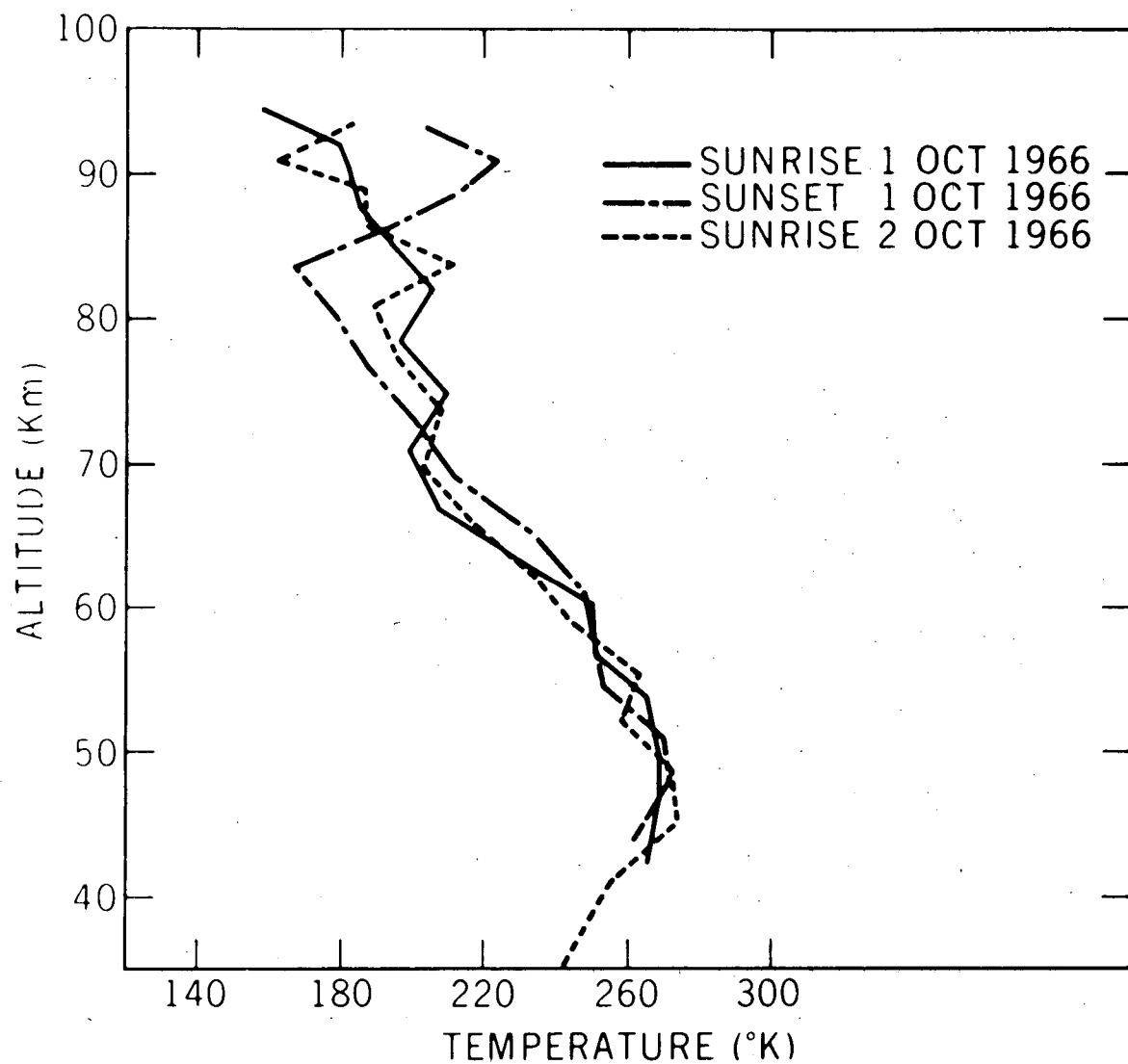


Figure 3.2.1. Temperature profiles at Natal (6 S). The soundings were separated in time by twelve hours. (after Smith, et al., 1968b).

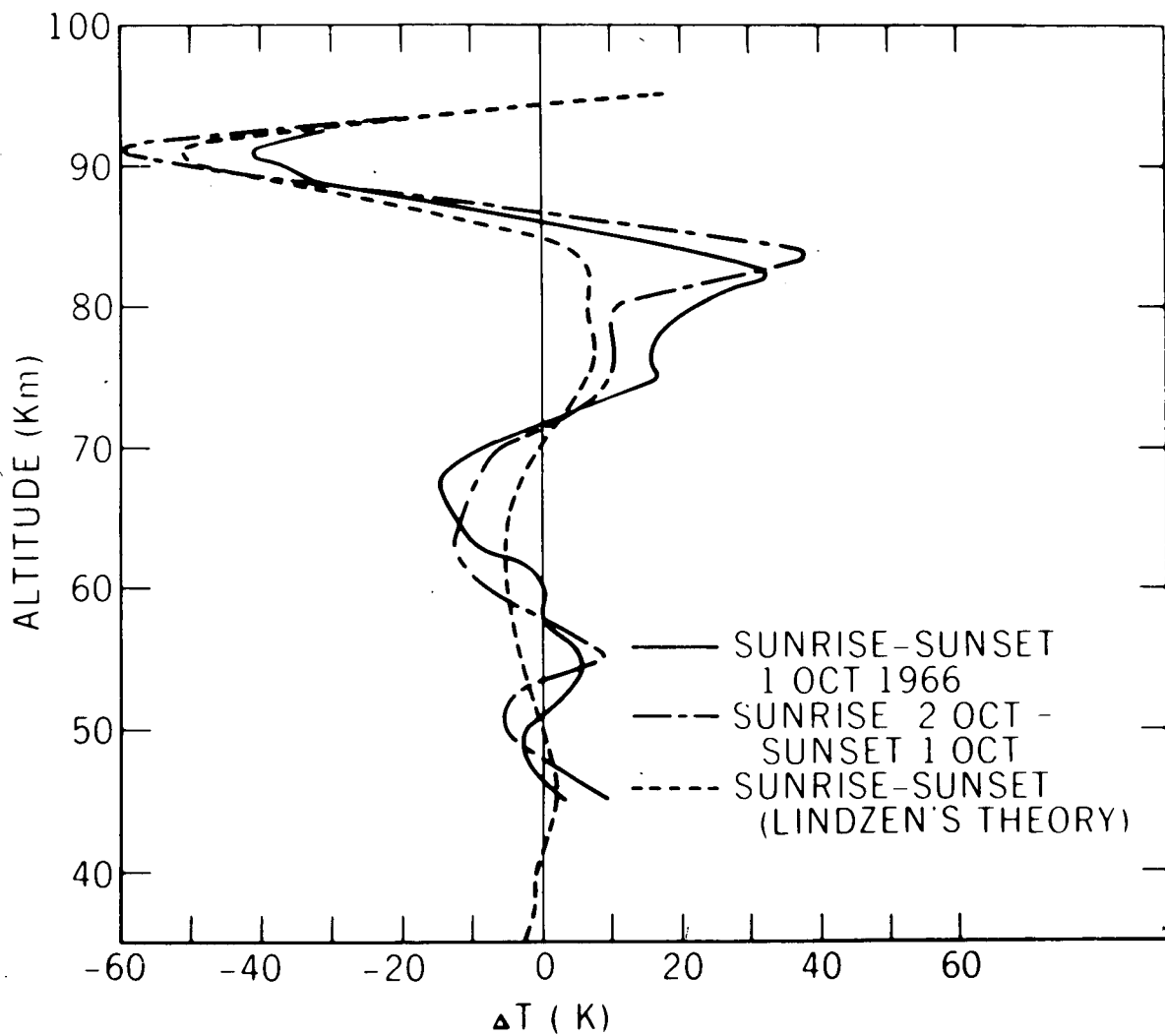


Figure 3.2.2. Twelve hour temperature changes as a function of altitude at Natal compared with theoretical change. (after Smith, et al., 1968b).

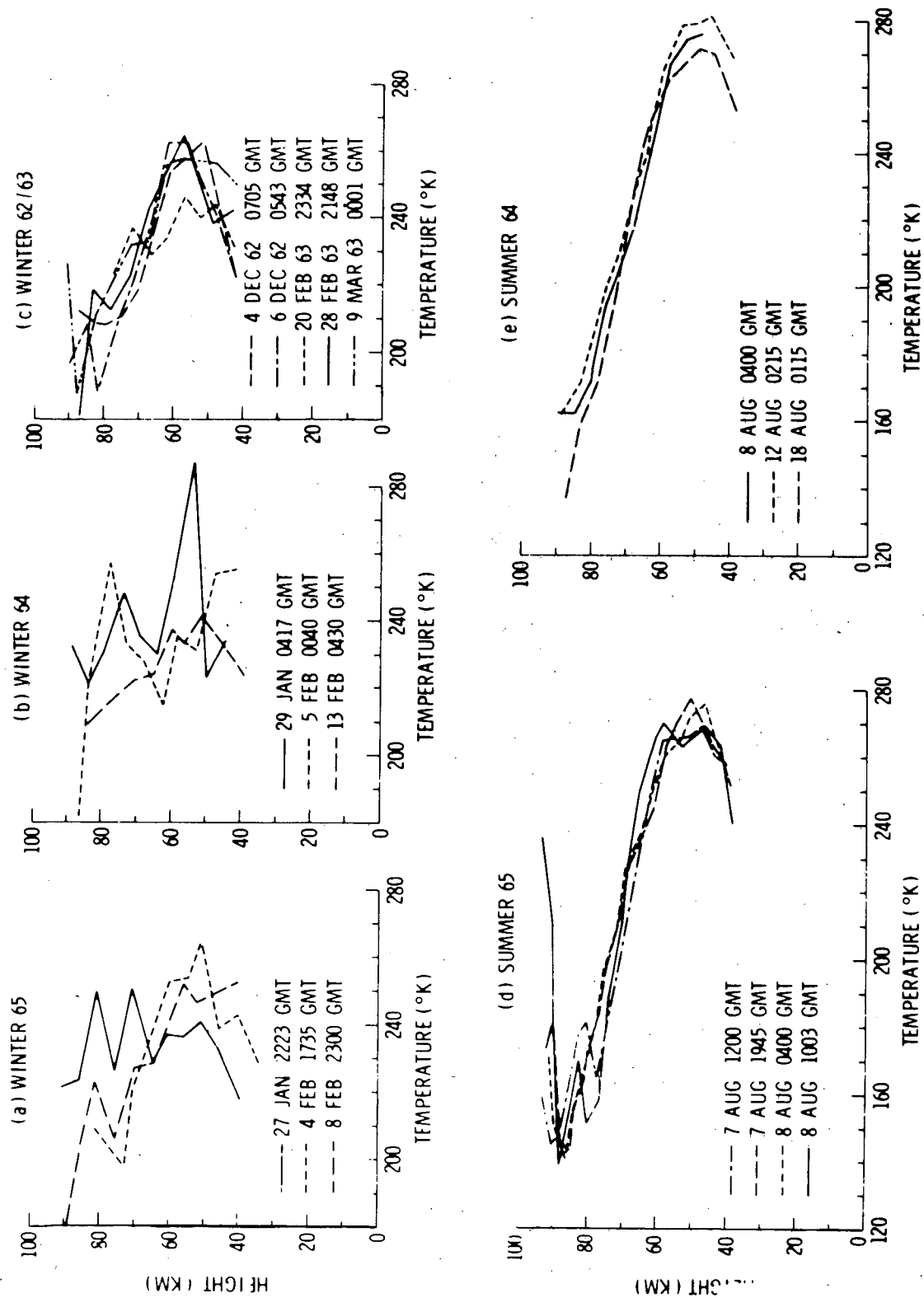


Figure 3.2.3. Typical winter (a, b, c) and summer (d, e) temperature soundings at Wallops Island (38 N).

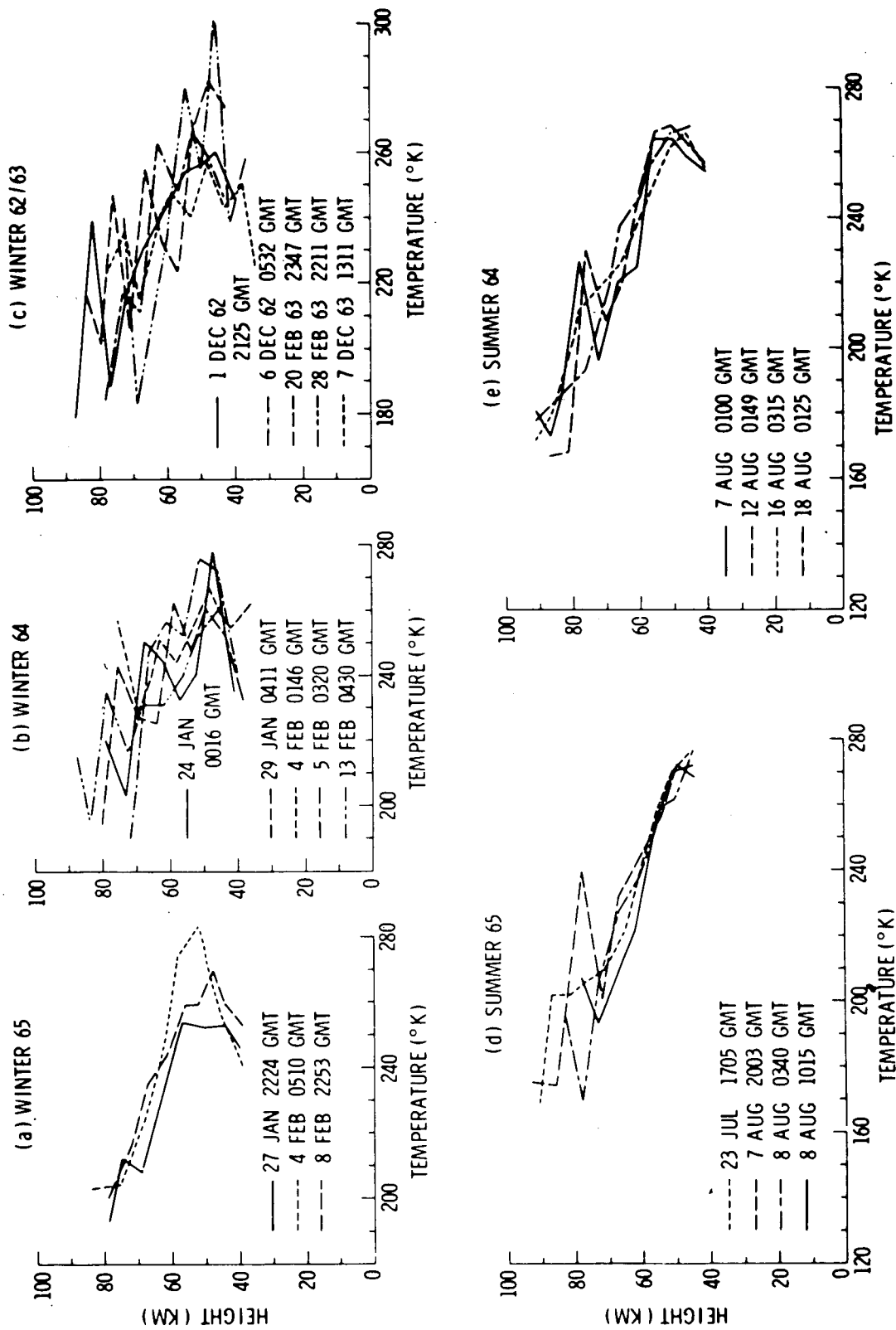


Figure 3.2.4. Typical winter (a, b, c) and summer (d, e) temperature soundings at Churchill (59°N). (after Theon, 1968).

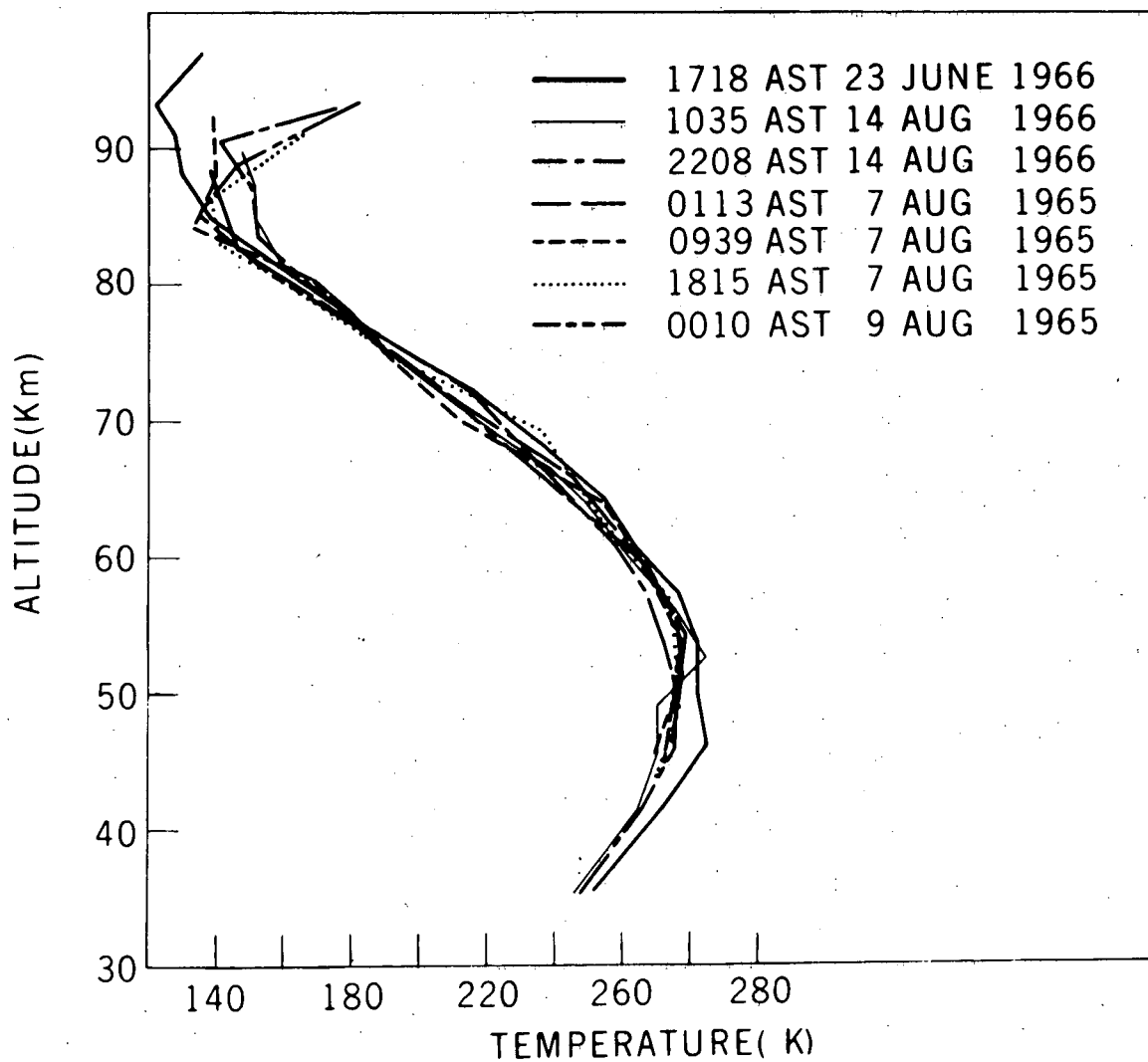


Figure 3.2.5a. Summer temperature profiles at Barrow (71 N). (after Theon, 1968).

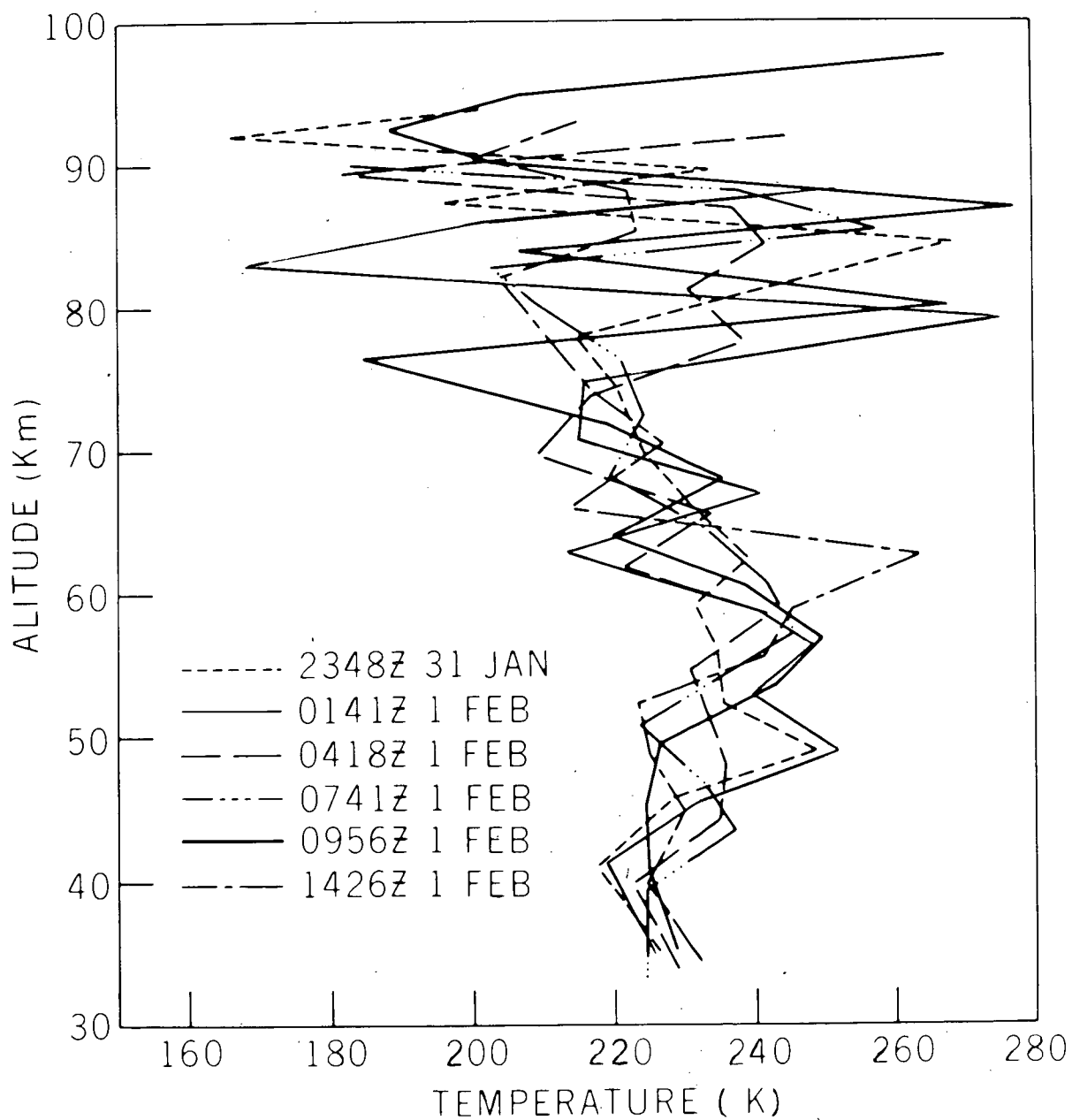
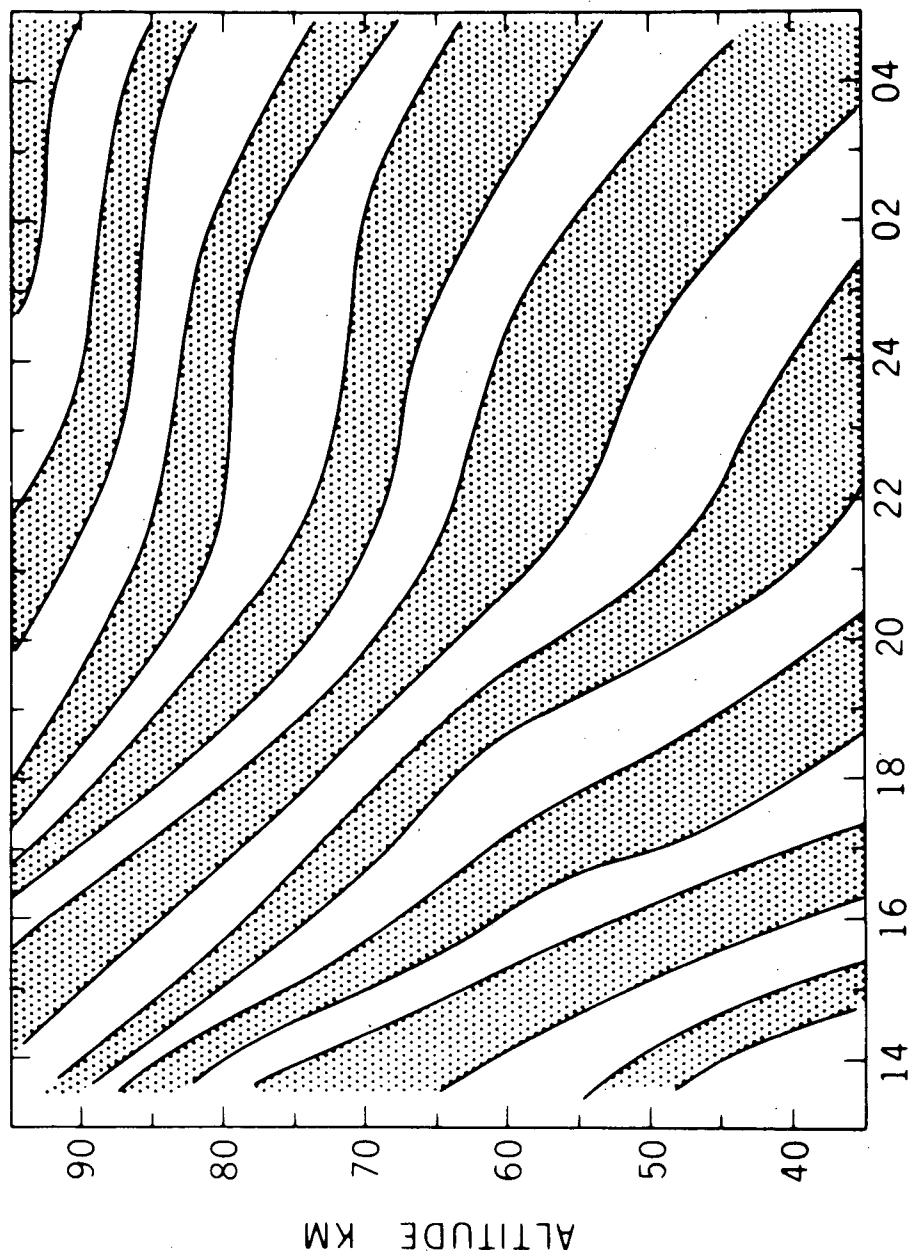


Figure 3.2.5b. Winter temperature profiles at Barrow in 1967. (after Smith, et al., 1968b).



ALASKA STANDARD TIME, HRS

Figure 3.2.5c. Diagram indicating warmed (shaded) and cooled regions at Barrow. Phase propagation is downward.

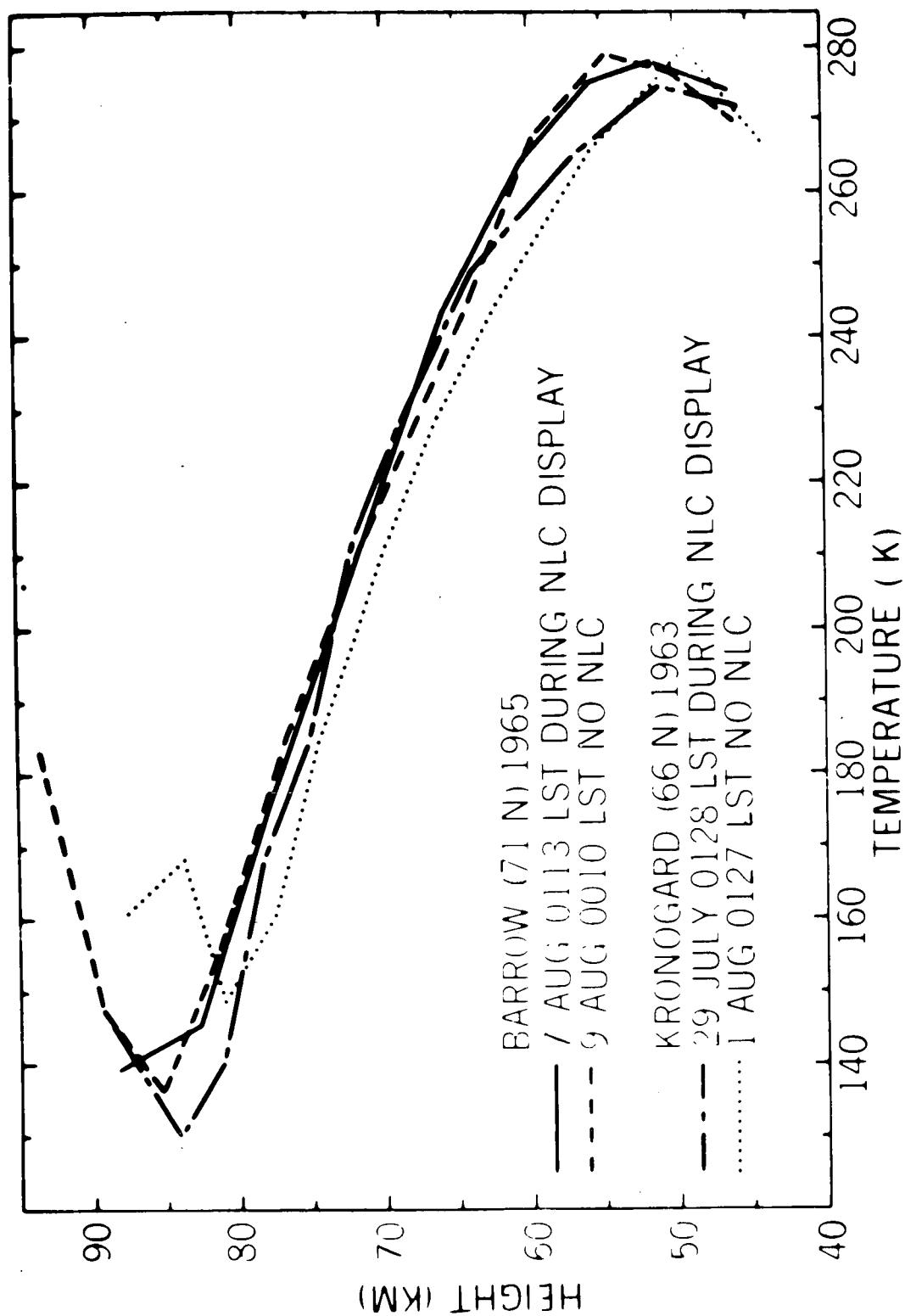


Figure 3.3.1. Temperature profiles above Kronogard, Sweden (66 N), and Barrow during the summers of 1963 and 1965, respectively. Note that the Barrow mesopause was colder in the absence of noctilucent clouds than during the cloud display, but the reverse was observed at Kronogard. (LST = local standard time; NLC = noctilucent cloud). (after Theon, et al., 1967).

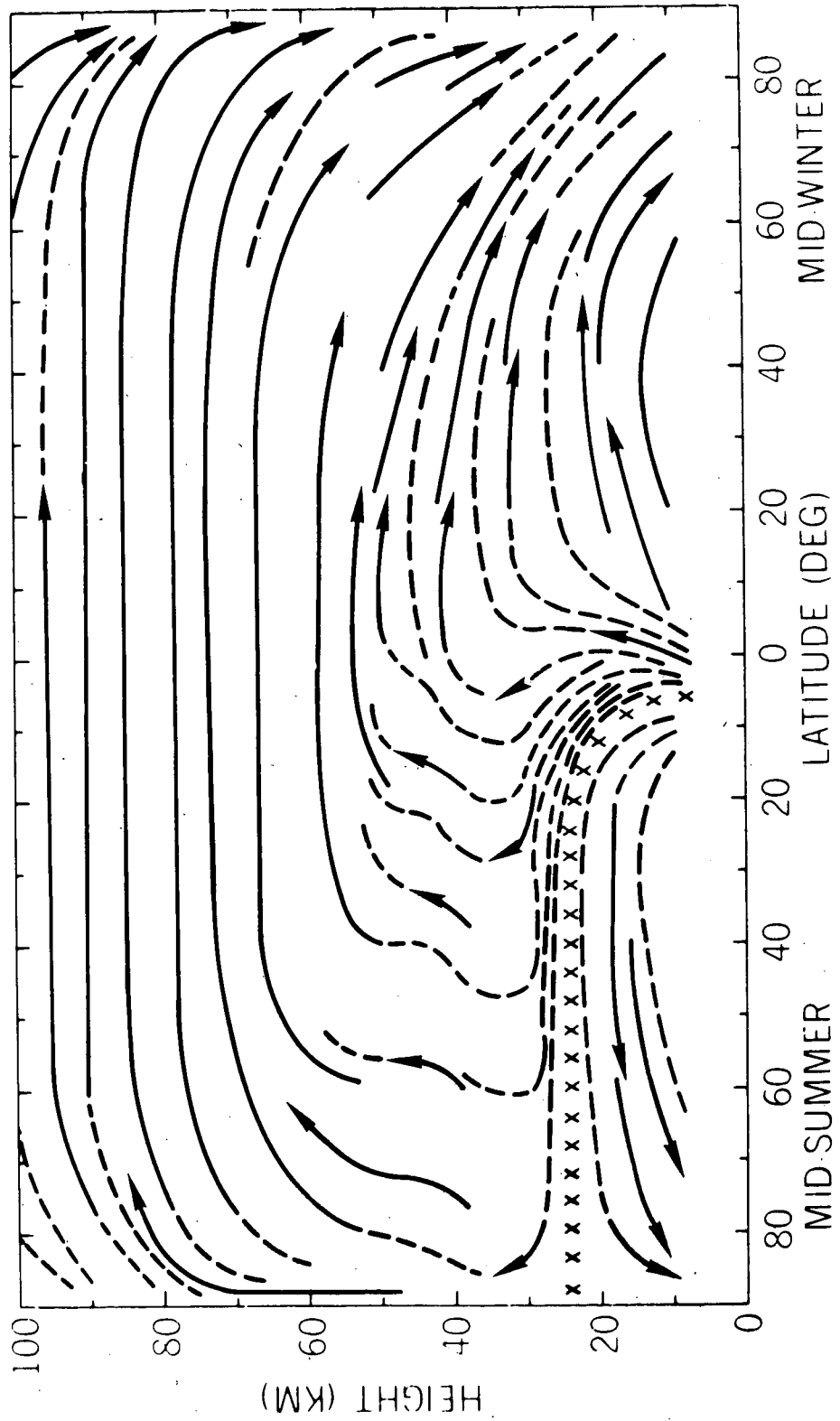


Figure 3.3.2. Meridional circulation. (after Hessvedt, 1964).

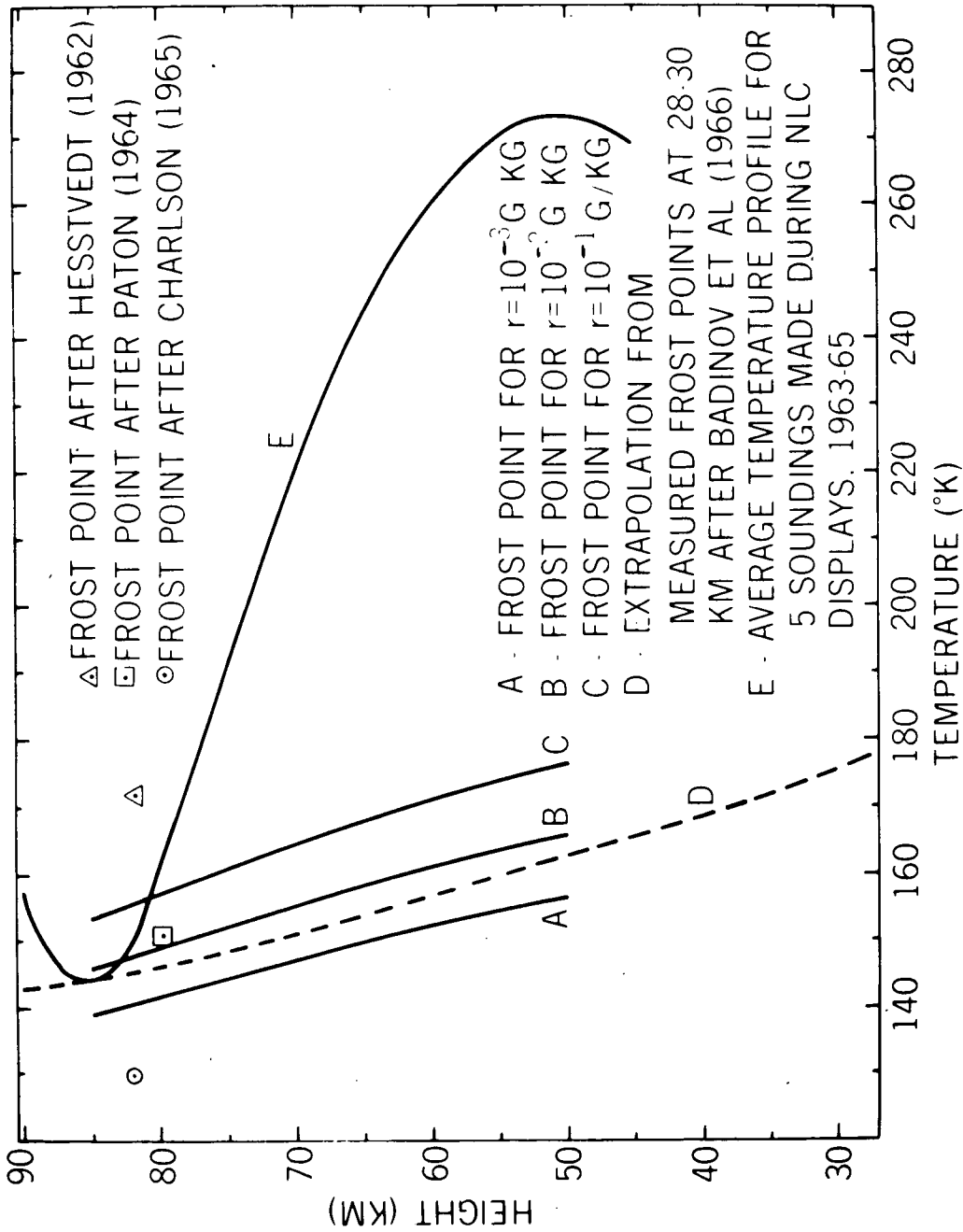


Figure 3.3.3. Comparison of estimates of frost points by several authors, with the average temperature profile for the five soundings conducted during displays of noctilucent clouds. A, Frost point for mixing ratio of 10^{-3} g kg $^{-1}$, B, 10^{-2} g kg $^{-1}$, for 10^{-1} g kg $^{-1}$; D, extrapolation from measured frost points at 28 to 30 km by after Badinov, et al. (1966); and E, average temperature profile for five soundings made during displays of noctilucent clouds, 1963 to 1965. (after Theon, et al., 1967).

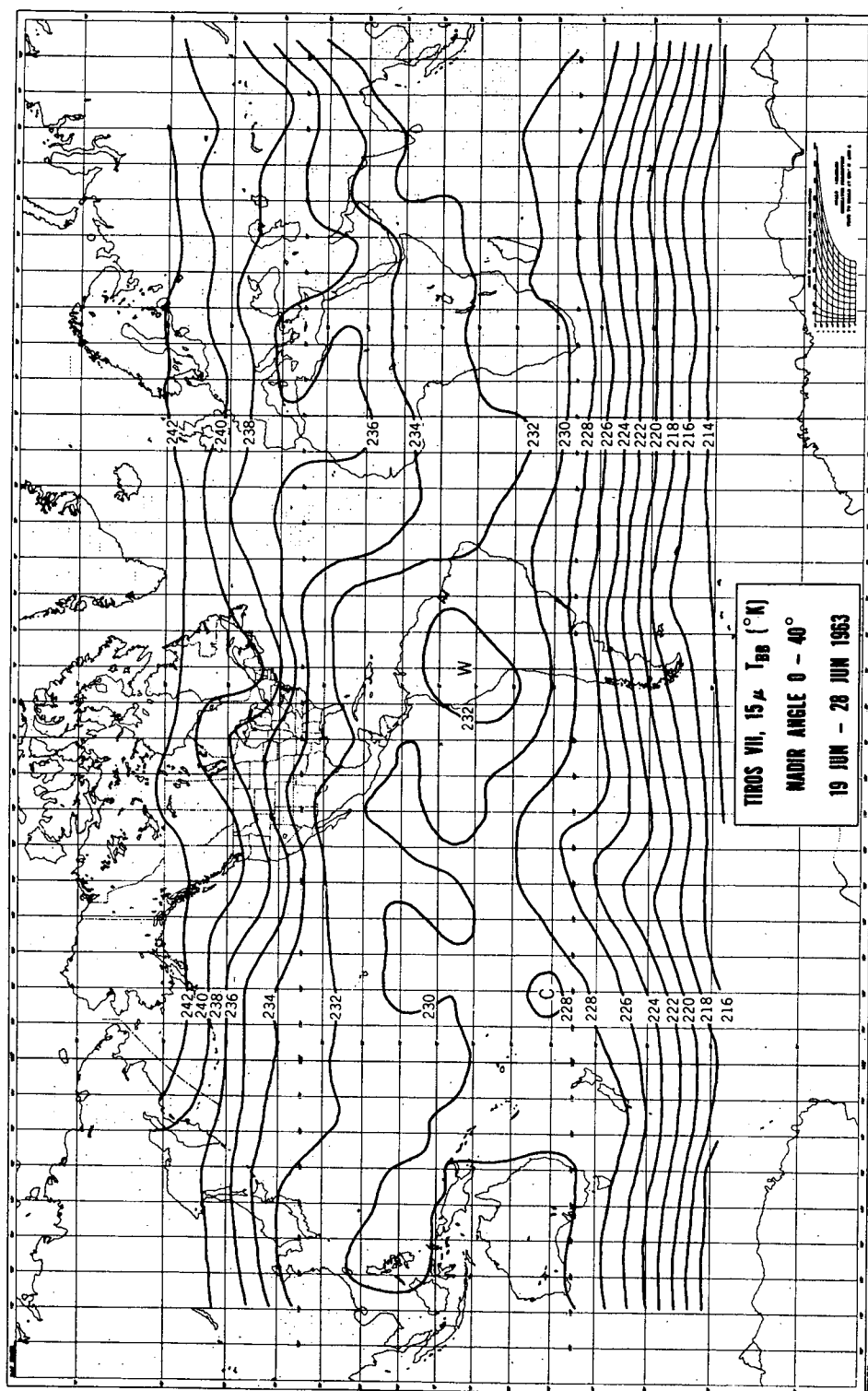


Figure 3.4.1. Isotherms for average equivalent black-body temperatures derived from TIROS 7 radiation observations during the period 19 June - 28 June 1963. Numbers along isotherms are in degrees K. Radiation observations were restricted to nadir angles 0-40 degrees. (after Kennedy and Nordberg, 1967).

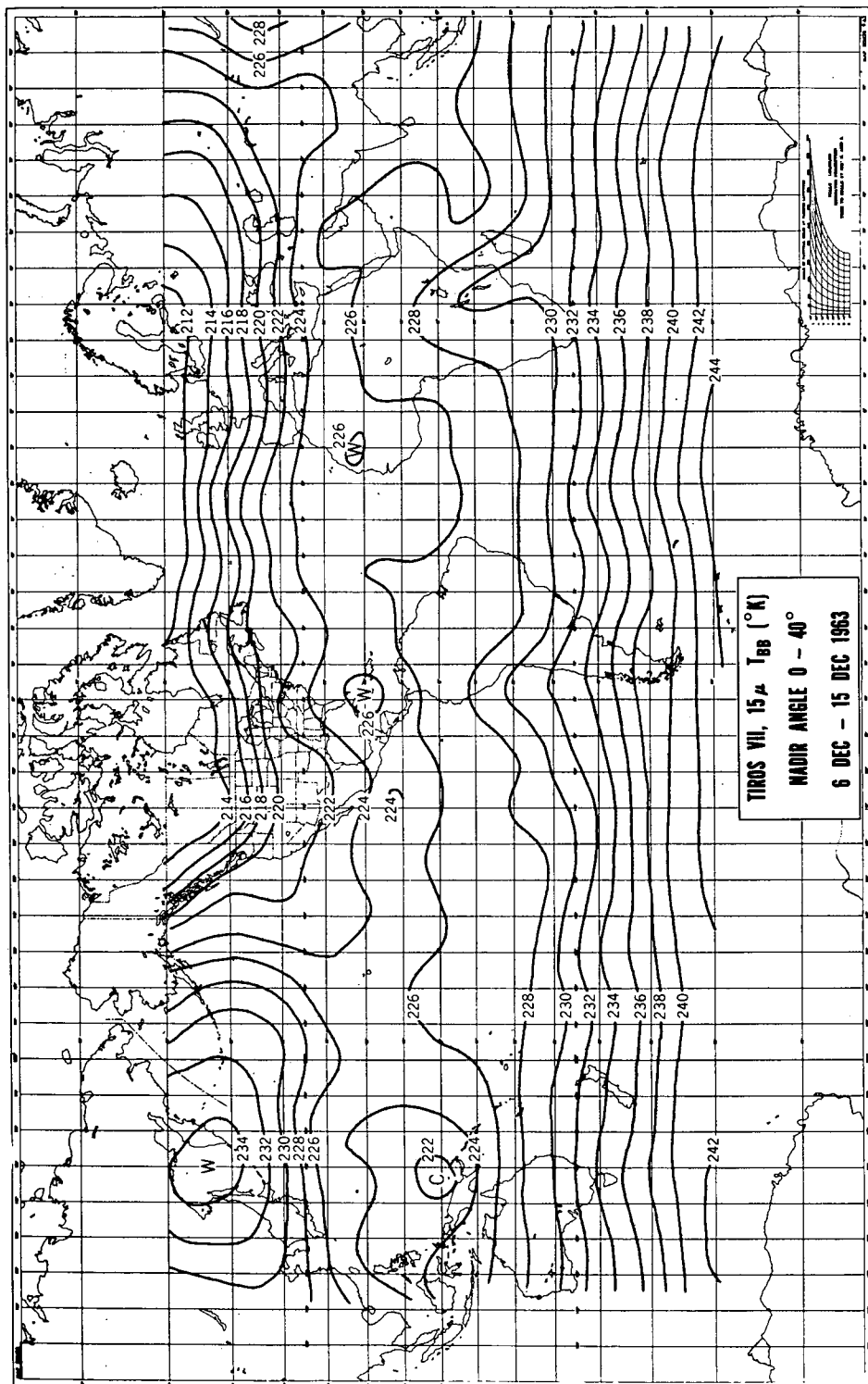


Figure 3.4.2. Same as Figure 3.4.1 for period 10-19 December 1963.

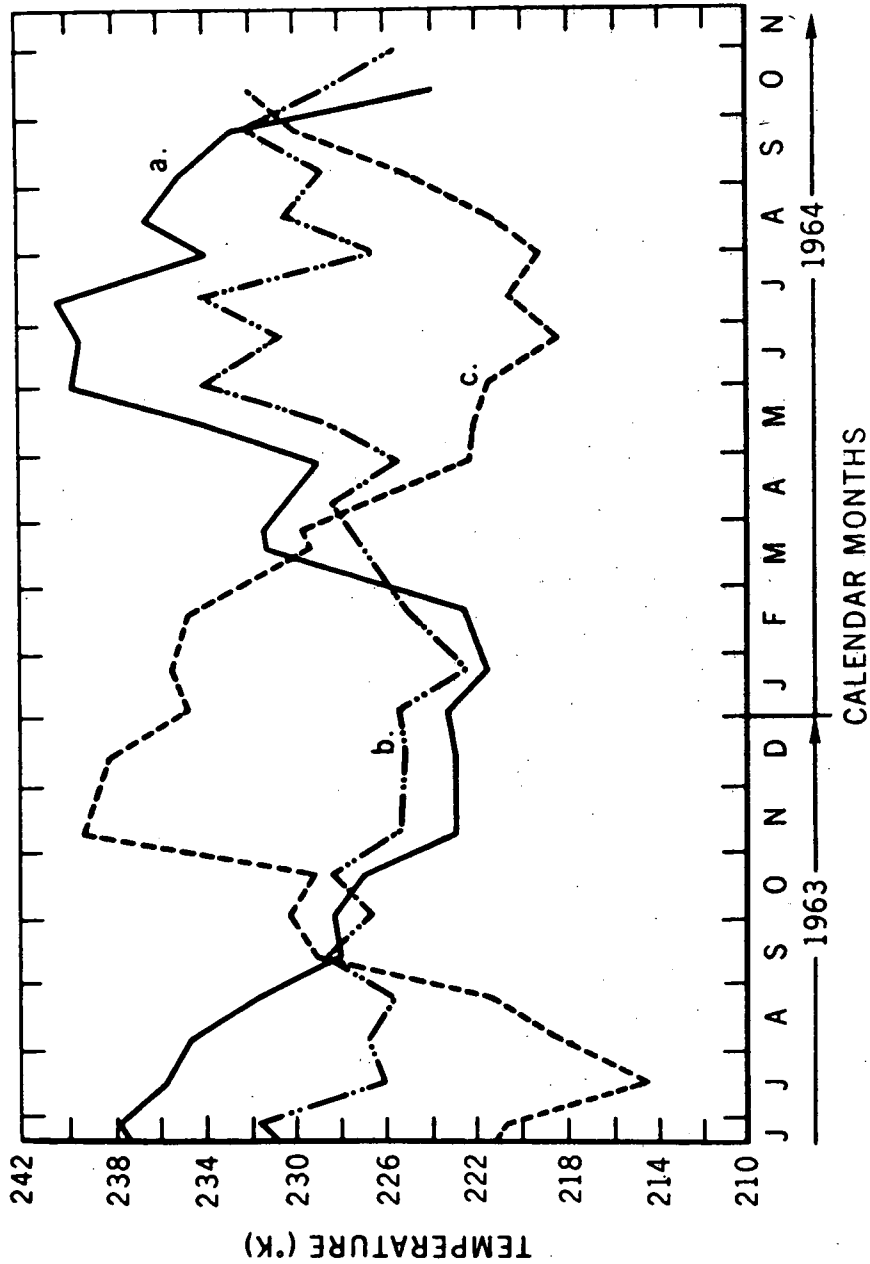


Figure 3.4.3. Variations of average black-body temperatures derived from TIROS VII radiation observations with time for a., latitudes 40-65 N, b., latitudes 30 N-30 S and c., 40-65 S. Averages are for typical 10-day periods for each respective season. (after Kennedy and Nordberg, 1967).

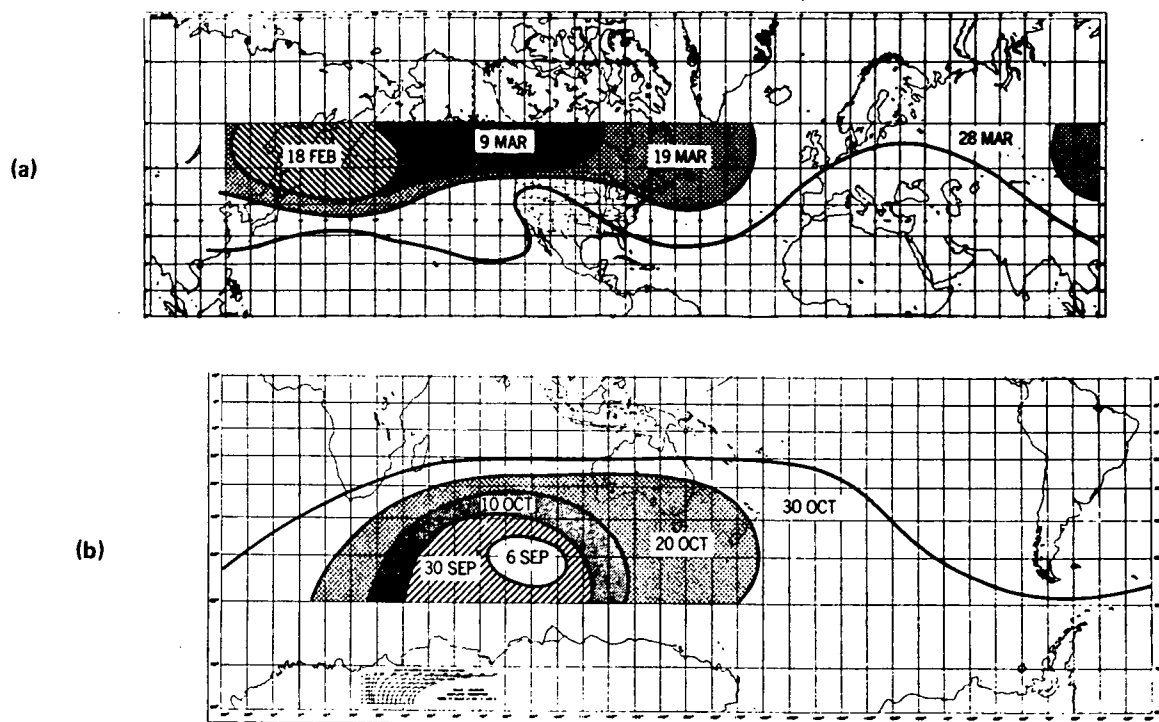


Figure 3.4.4. Progression of the final warming in the Northern Hemisphere stratosphere in 1964 (a) and for the Southern Hemisphere in 1963 (b). Solid lines indicate the 230 K equivalent black-body isotherms for the dates shown. (after Kennedy and Nordberg, 1967).

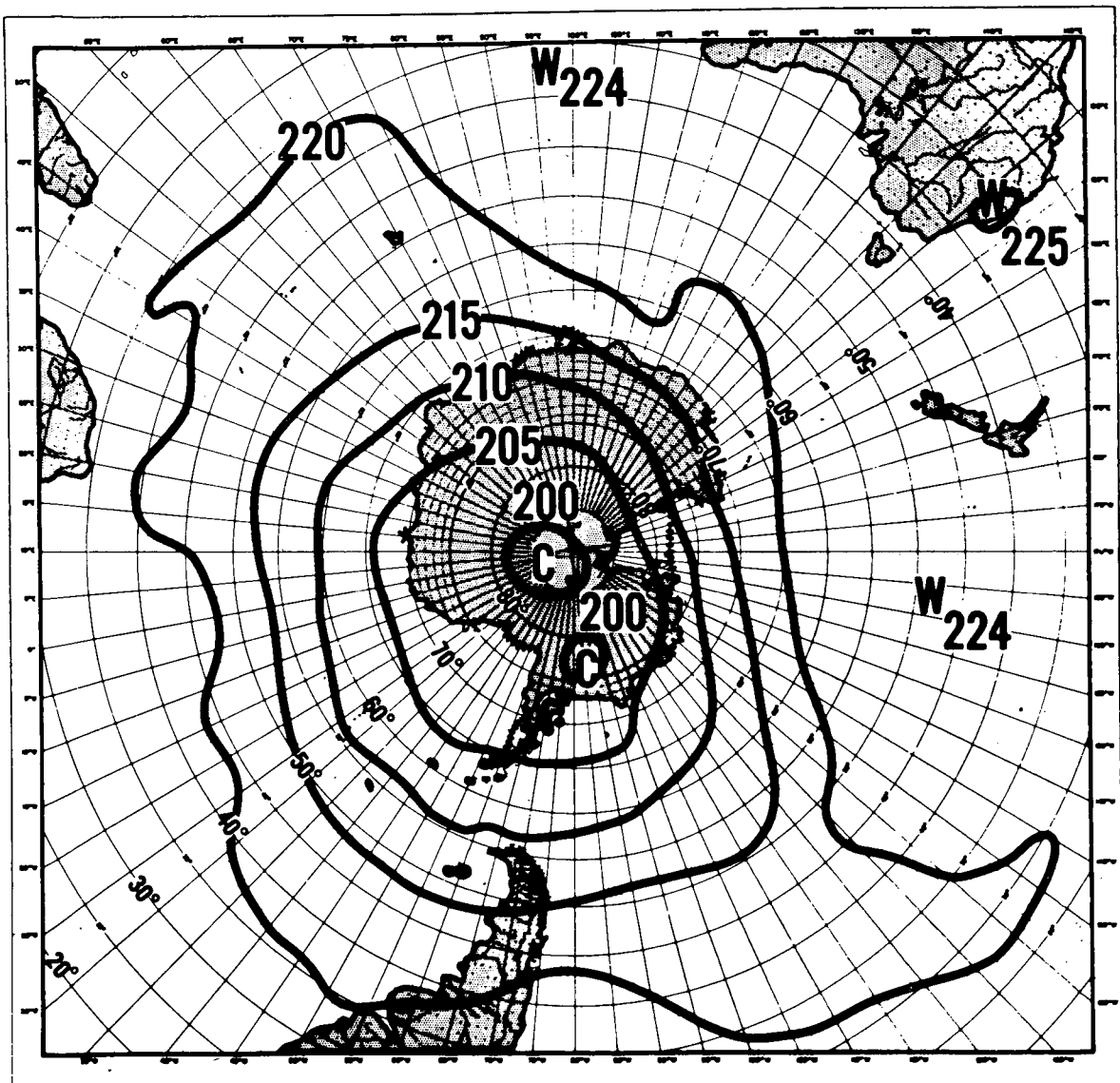
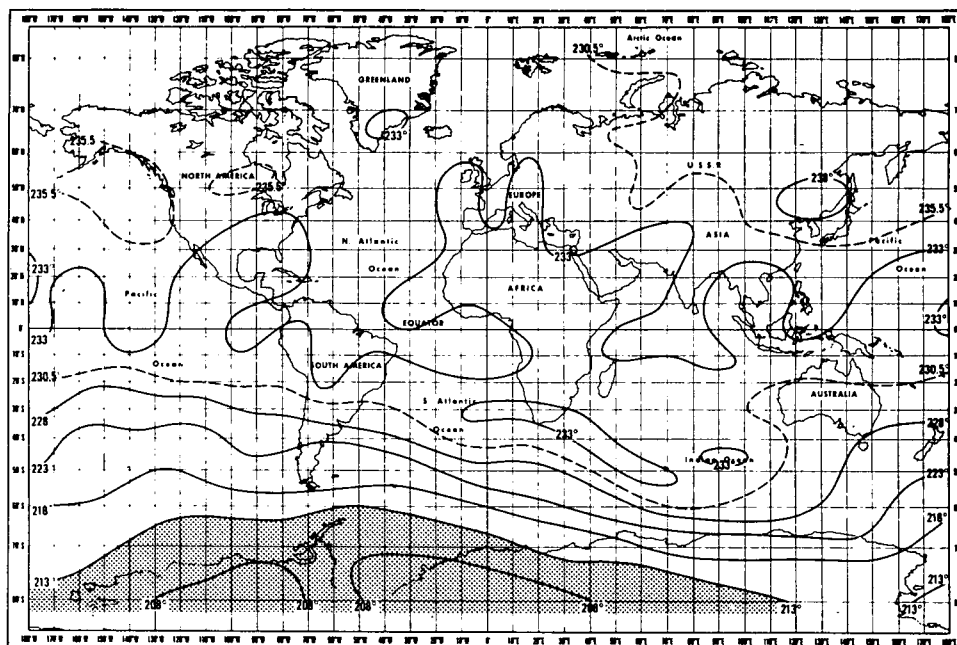
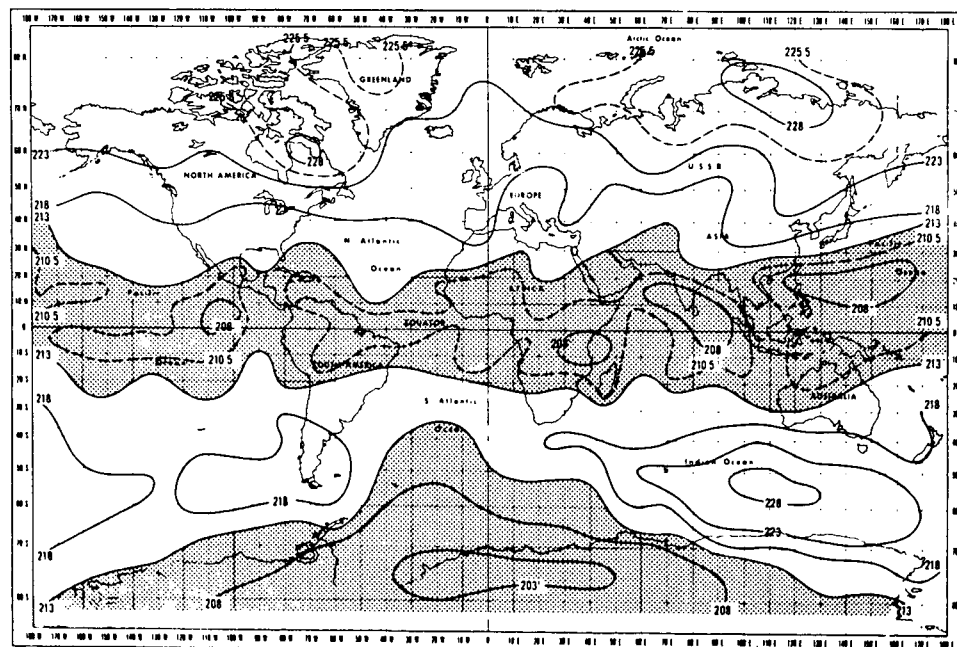


Figure 3.4.5. Stratospheric Temperature Distribution (K) from Nimbus 2 Measurements on June 10, 1966.



10 MB



50 MB

Figure 3.4.6. Nimbus 3 IRIS temperatures (K) on April 29, 1969 for 50 mb level (a) and for 10 mb level (b). (after Prabhakara et al.).

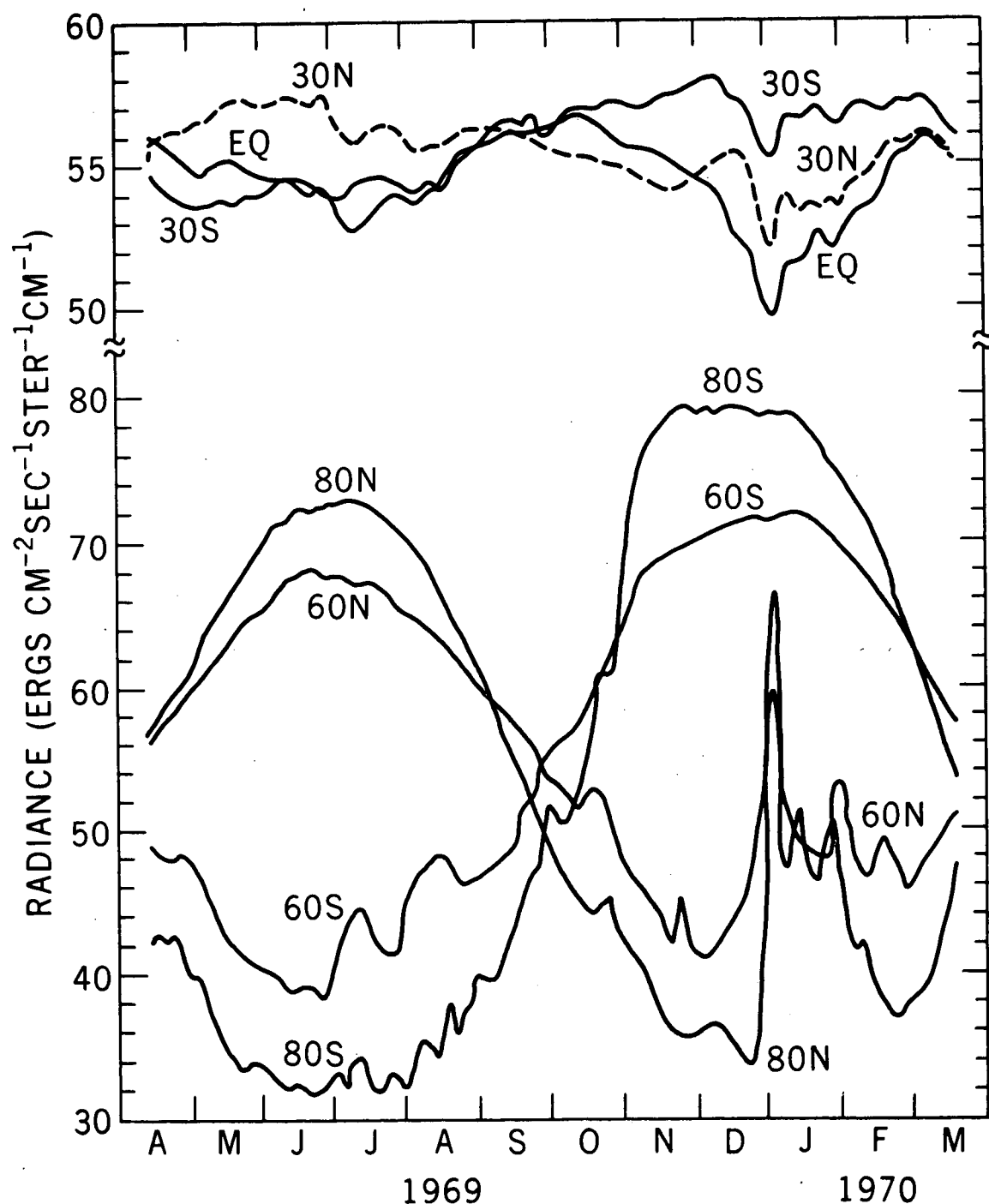


Figure 3.4.7. Annual march of radiance measured with the SIRS at $15.0\ \mu\text{m}$ ($669.3\ \text{cm}^{-1}$) for selected latitudes showing the seasonal warming and cooling of the stratosphere. For each latitude indicated, measurements were averaged daily over a 4-degree zone around the latitude circle. (after Fritz and Soules, 1970).

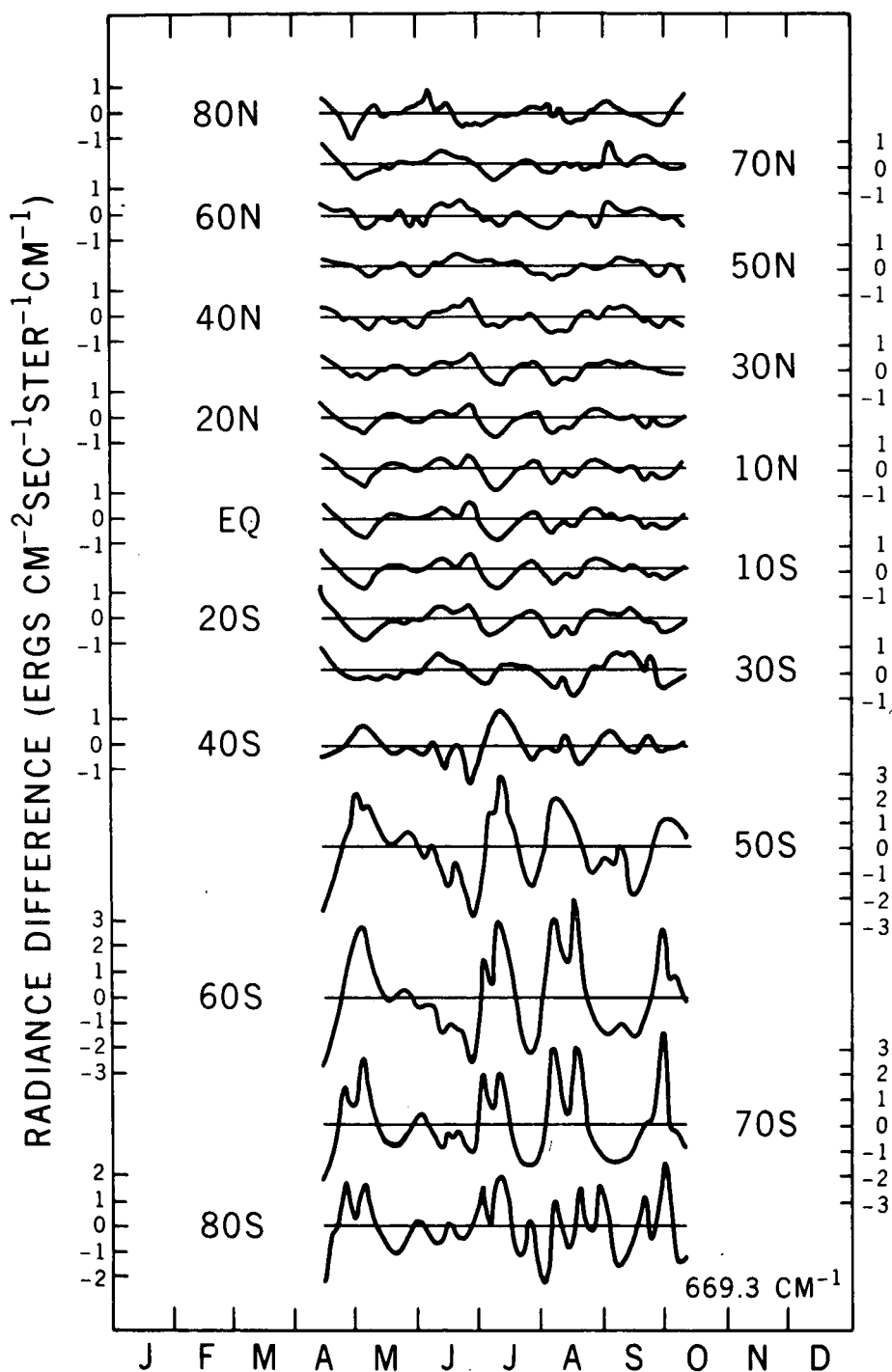


Figure 3.4.8. Deviation of averaged latitudinal radiances measured with SIRS at $15\mu\text{m}$ from a least squares fit for 80 N to 80 S from April 14-October 10, 1969 showing close relationship between the Southern Hemisphere warming and cooling periods in the high latitudes and corresponding cooling and warming periods in the tropical and Northern Hemisphere latitudes. (after Fritz and Soules, 1970).

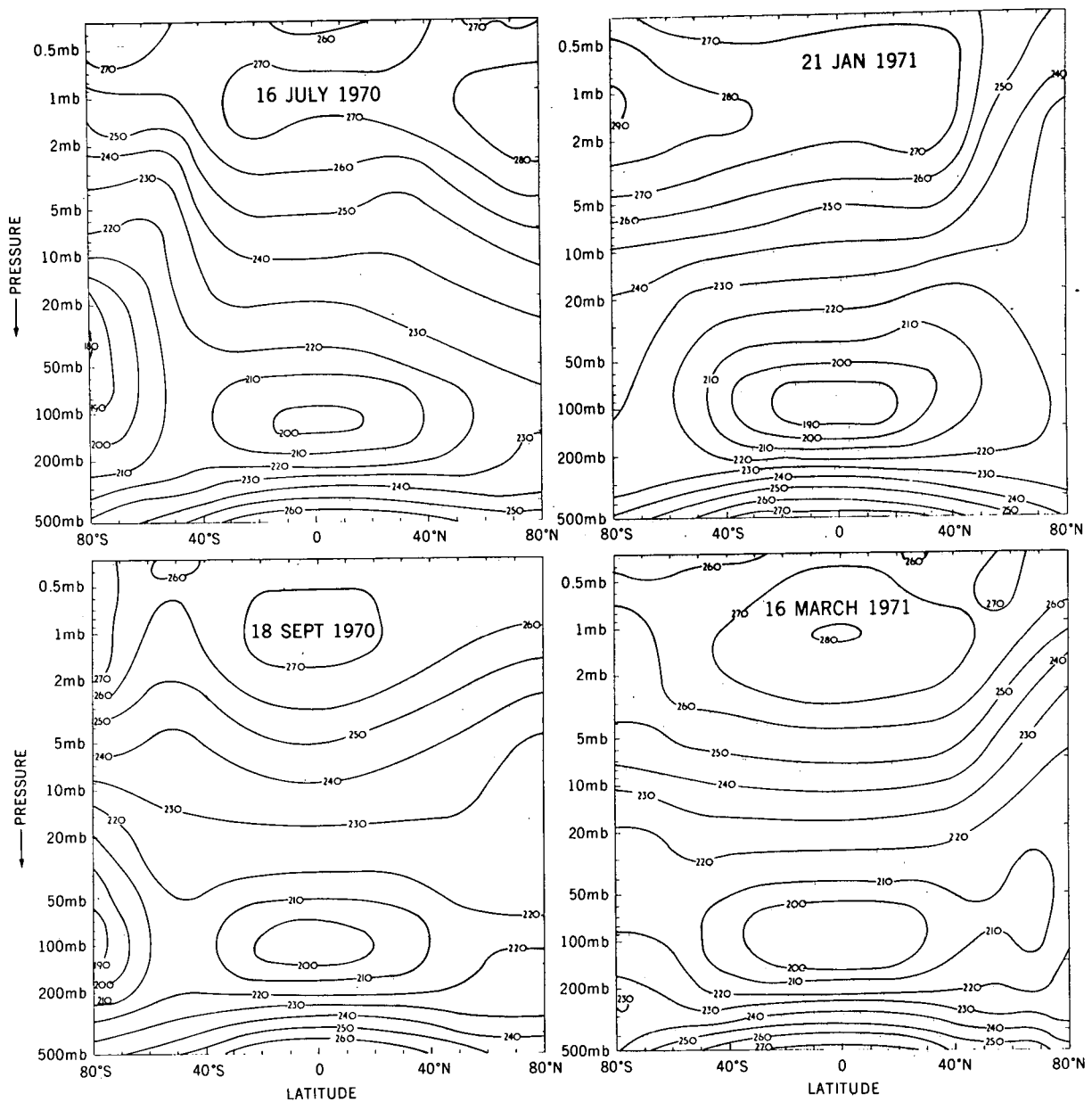


Figure 3.4.9. Meridional temperature cross-sections from surface to the 0.5 mb pressure level derived from SCR measurements on 16 July 1970, 18 September 1970, 21 January 1971 and 16 March 1971. Data from about twelve satellite passes at longitudes progressing successively westward by about 30 degrees were averaged for each latitude for each 24 hour period. (courtesy Williamson and Houghton).

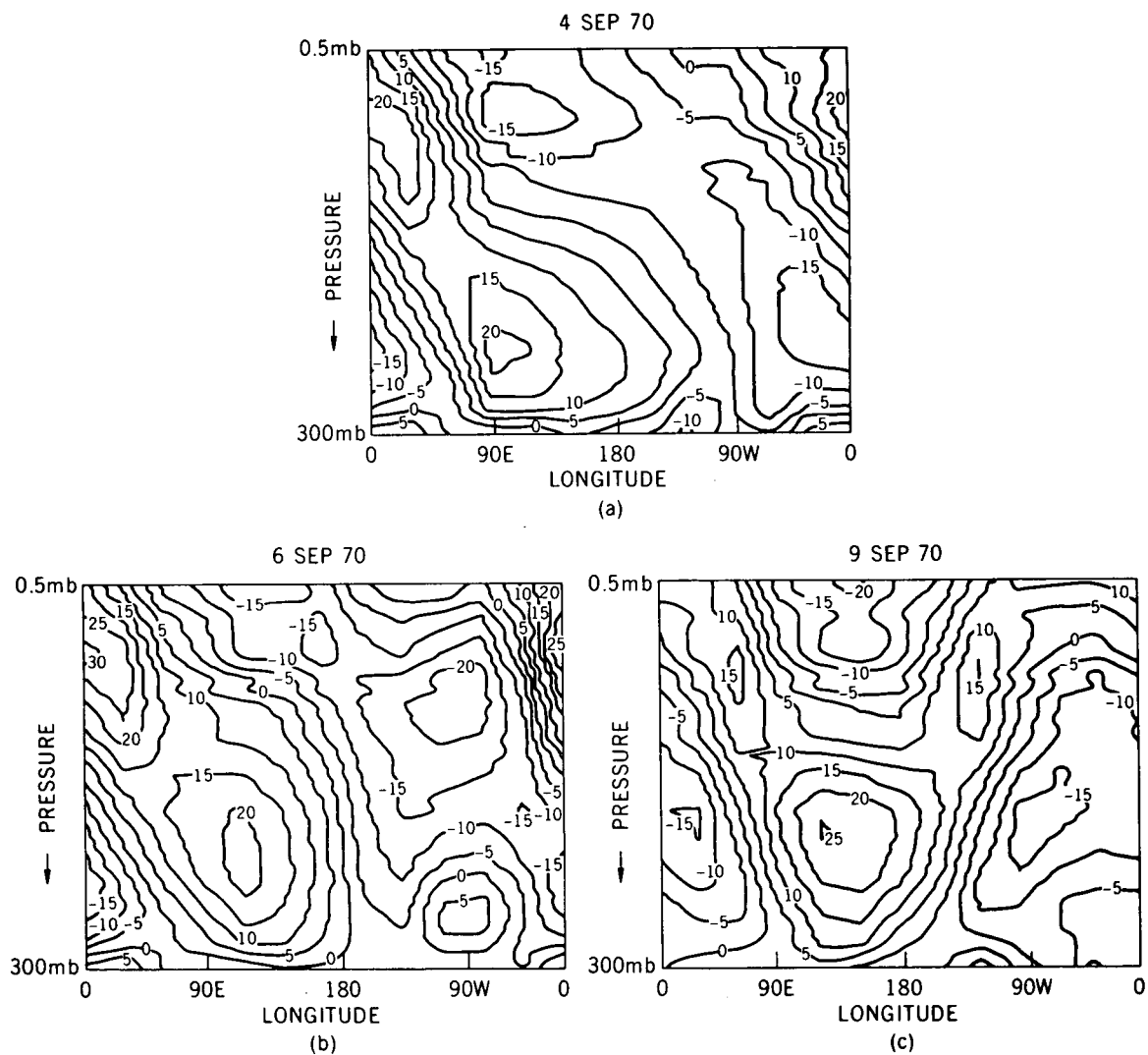


Figure 3.4.10. Cross-section of temperature deviation between the 300 and 0.5 mb levels at longitudes around the 55-60 S latitude zone, from the mean temperatures for this latitude zone on 4 September (a), 6 September (b), and 9 September (c) 1970. Temperature deviations are shown in degree C. (courtesy Williamson and Houghton).

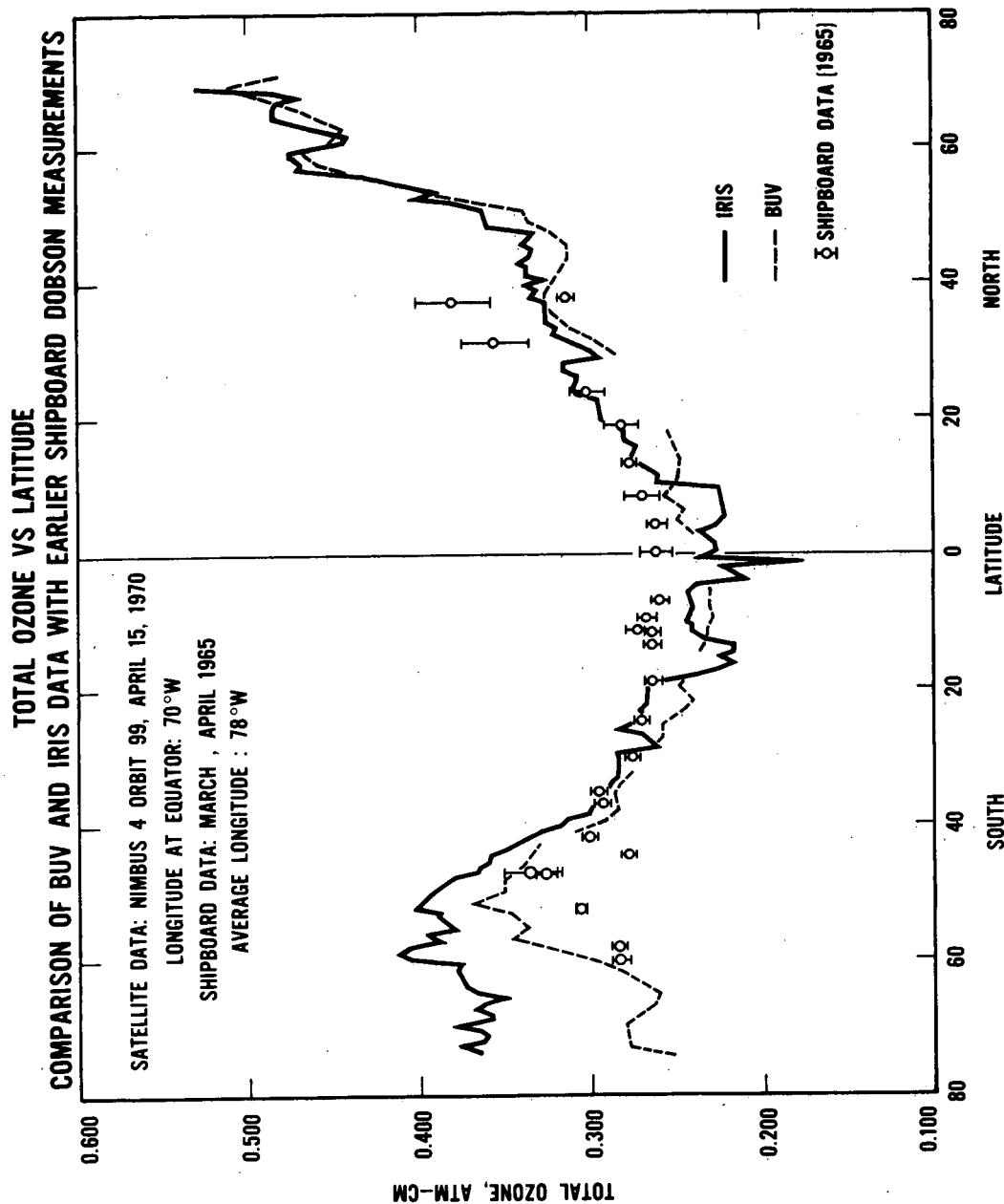
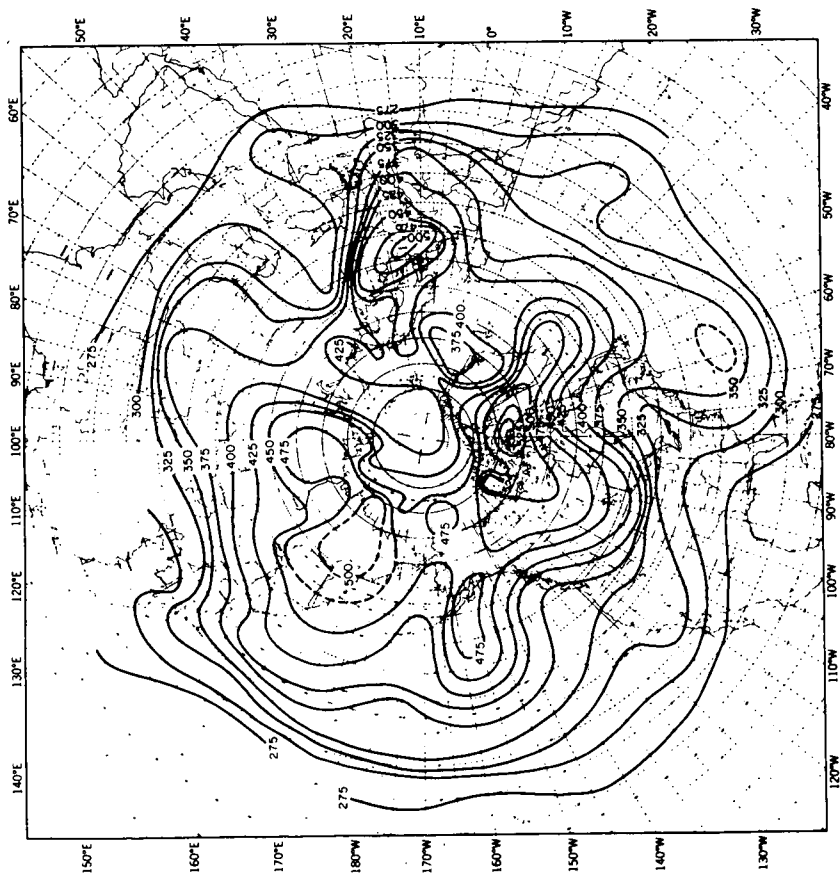
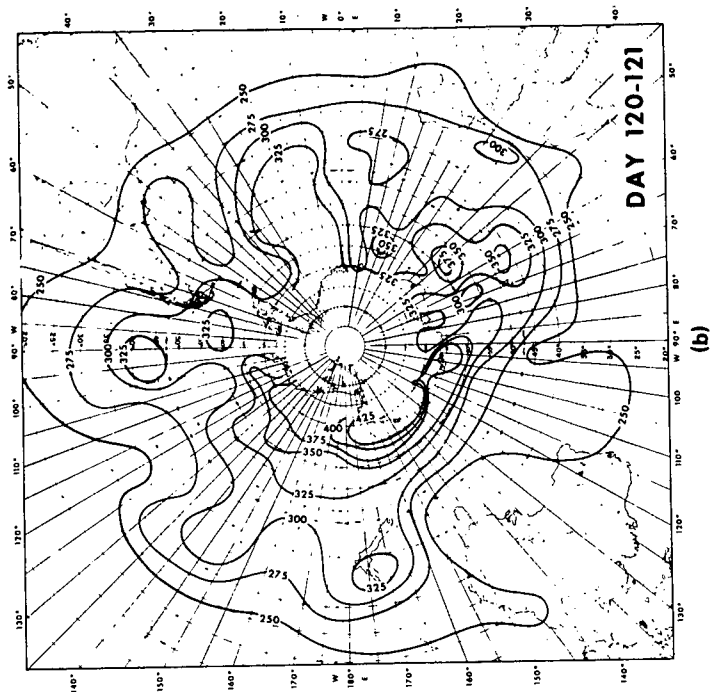


Figure 3.5.1.1. Comparison of total ozone amounts derived from the IRIS and BUV instruments on Nimbus 4 for orbit 99 on April 15, 1970. Points with error bars are results from an earlier latitudinal survey with a Dobson Spectrophotometer on board a ship.

BUV TOTAL OZONE APRIL 30 MAY 1, 1970 ORBITS 294-312



(a)



(b)

OZONE AMOUNTS IN MILLI ATM-CM

Figure 3.5.1.2. Total ozone contours for the northern and southern hemispheres derived from BUV measurements on April 30 and May 1, 1970. Units are milli atm-cm.

TOTAL O₃ (10⁻³ CM STP)

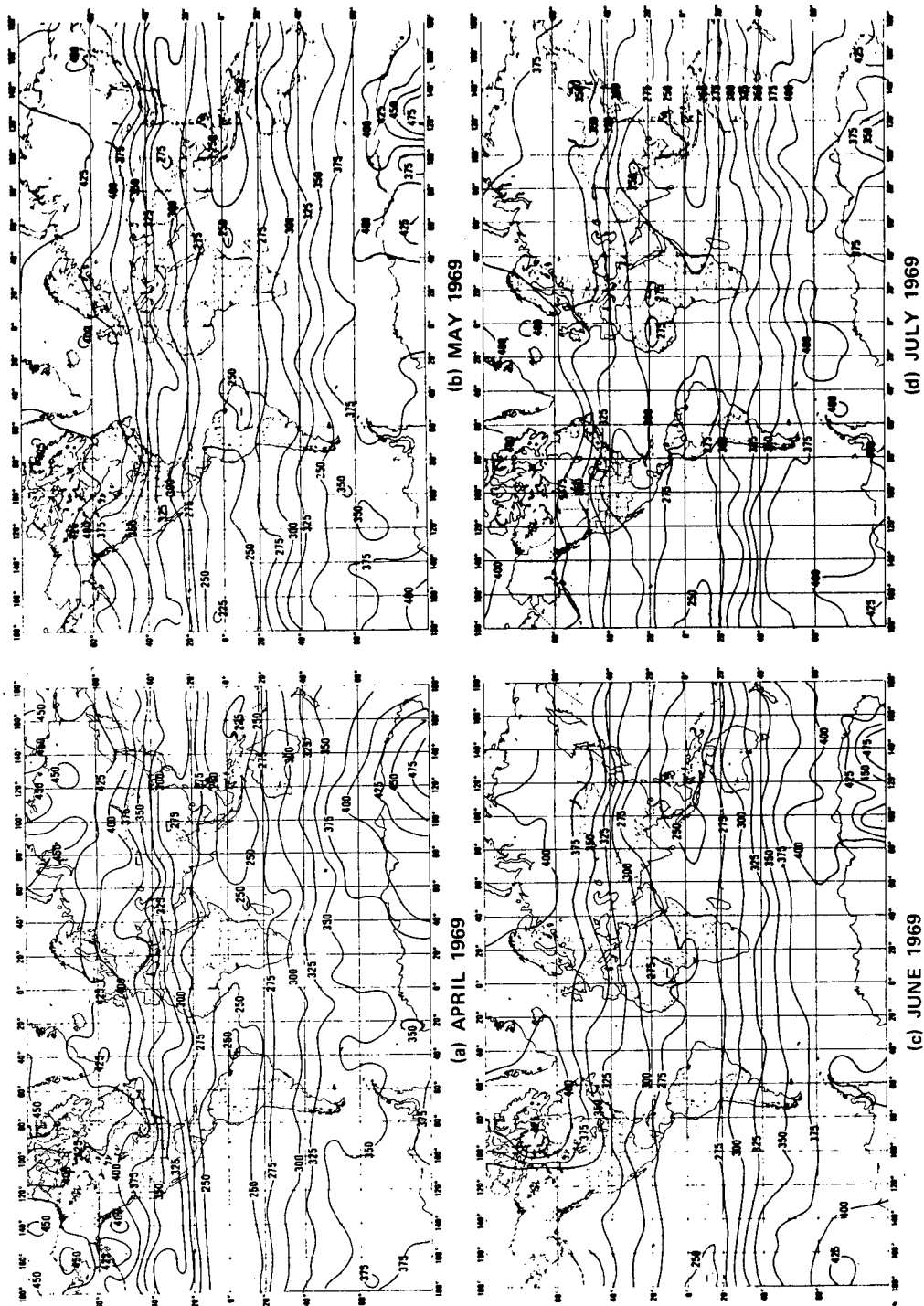


Figure 3.5.1.3. Global distribution of total ozone (10⁻³ cm STP) derived from Nimbus 3 IRIS for April (18-30), May, June and July (1-22) 1969.

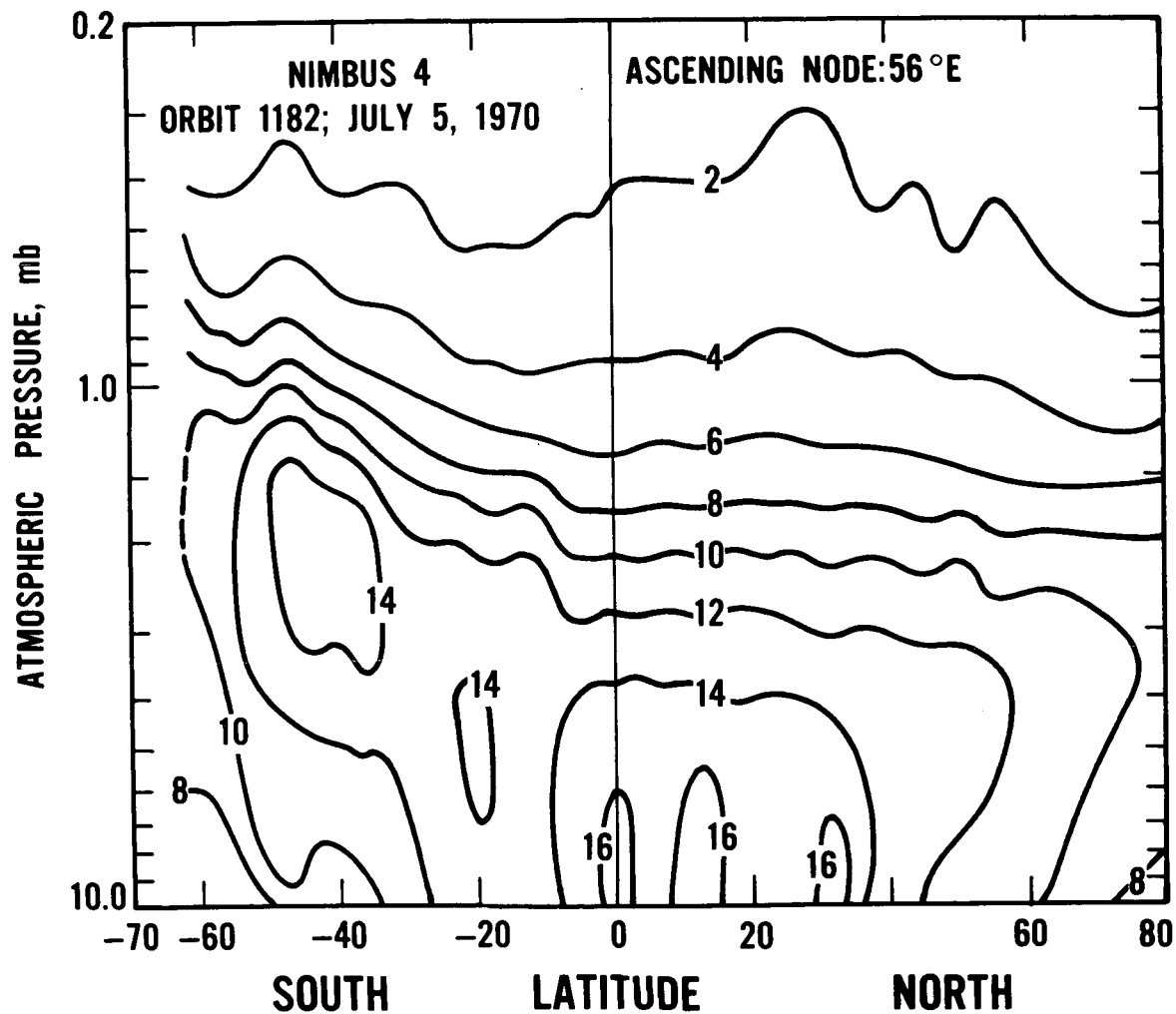
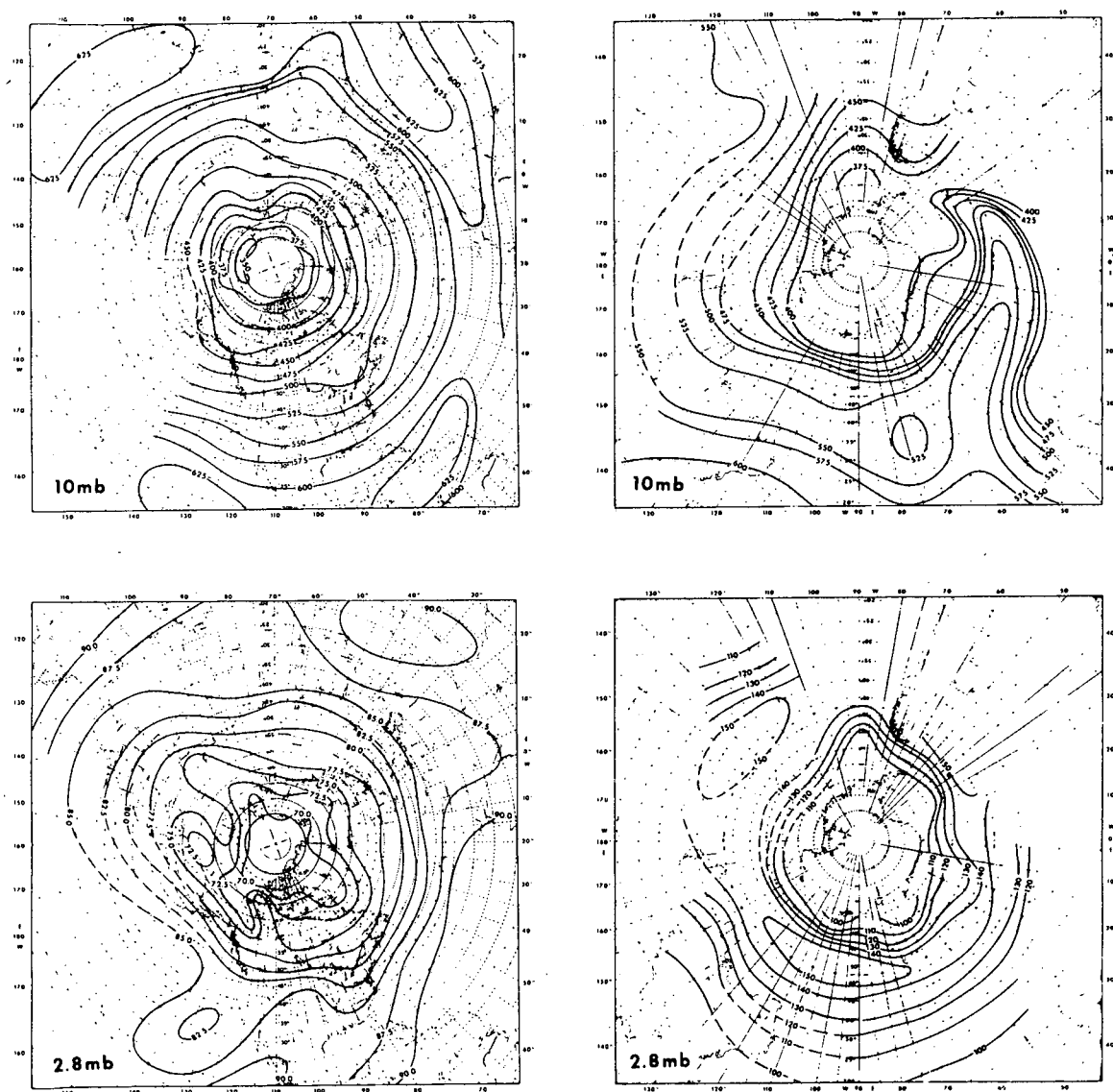


Figure 3.5.2.1. Meridional cross-section of ozone mass mixing ratio ($\mu\text{ gm gm}^{-1}$) in the atmospheric pressure region from 10 to 0.2 mb derived from BUUV earth radiance data at wavelengths from 2555 to 2976 Å from Nimbus 4 orbit 1182 on July 5, 1970.

TOTAL OZONE ABOVE 10mb AND 2.8mb



OZONE AMOUNTS IN 10^{-4} ATM-CM
July 5, 1970

Figure 3.5.2.2. Contours of total ozone above 10 mb (top) and total ozone above 2.8 mb (bottom) for northern and southern hemispheres on July 5, 1970 derived from BOV high altitude data.

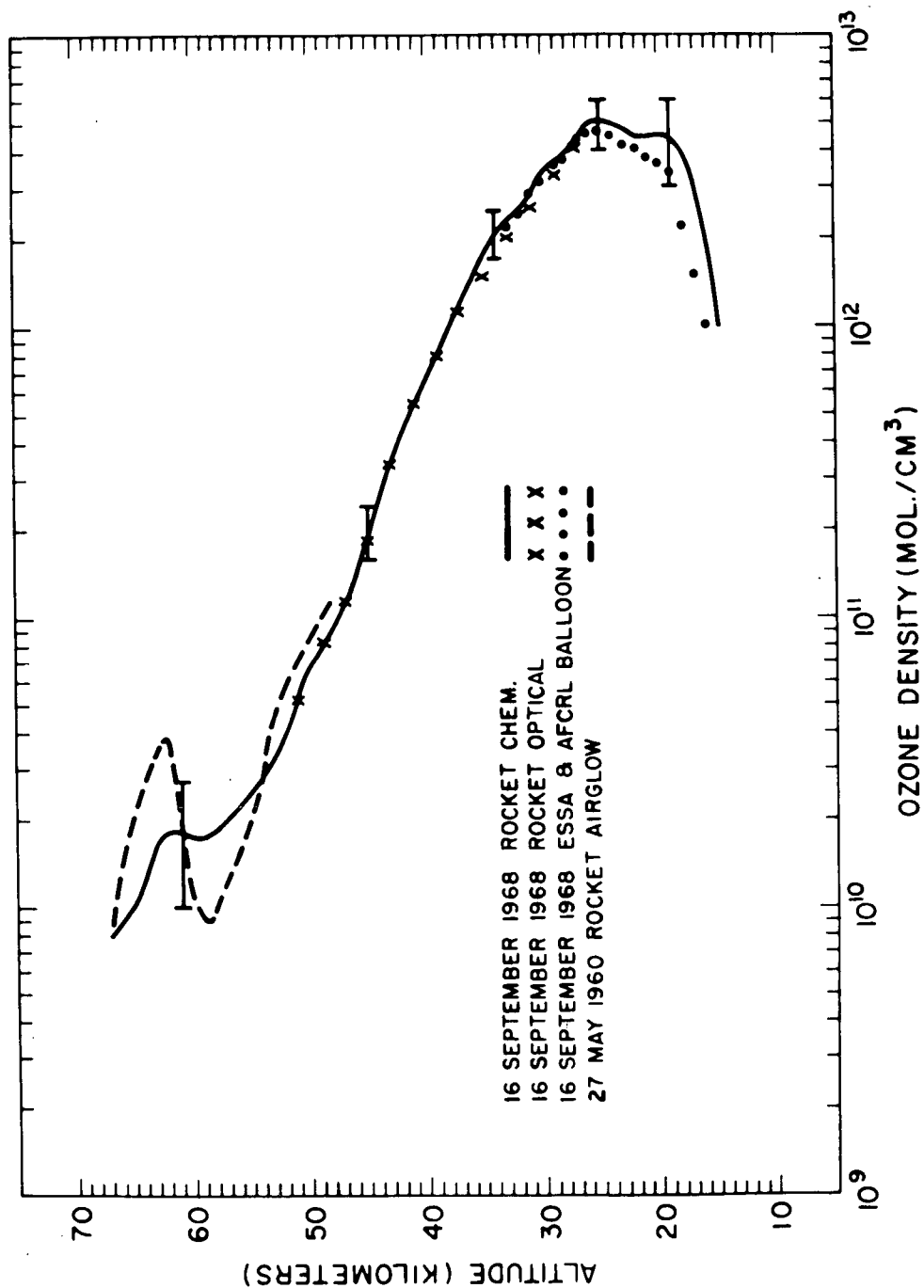


Figure 3.6.1. Ozone distribution measured with chemiluminescent probe on 16 September 1968 over Wallops Island, Virginia compared with simultaneous balloon and optical sondes, and airglow experiment by Reed et al. (1969).

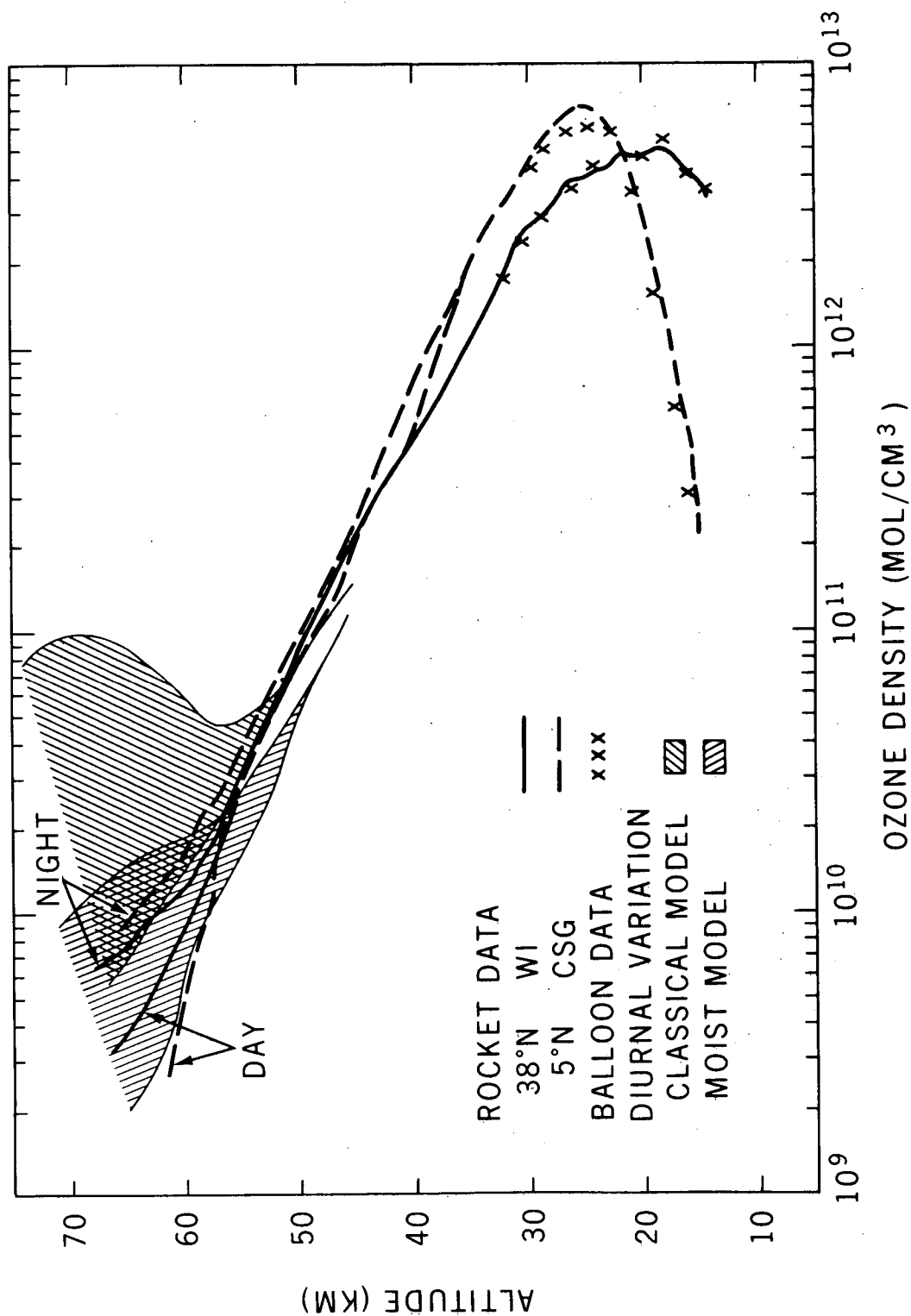


Figure 3.6.2. Diurnal Variation of Ozone. Measurements at two latitudes 5°N and 38°N, compared with photochemical models.

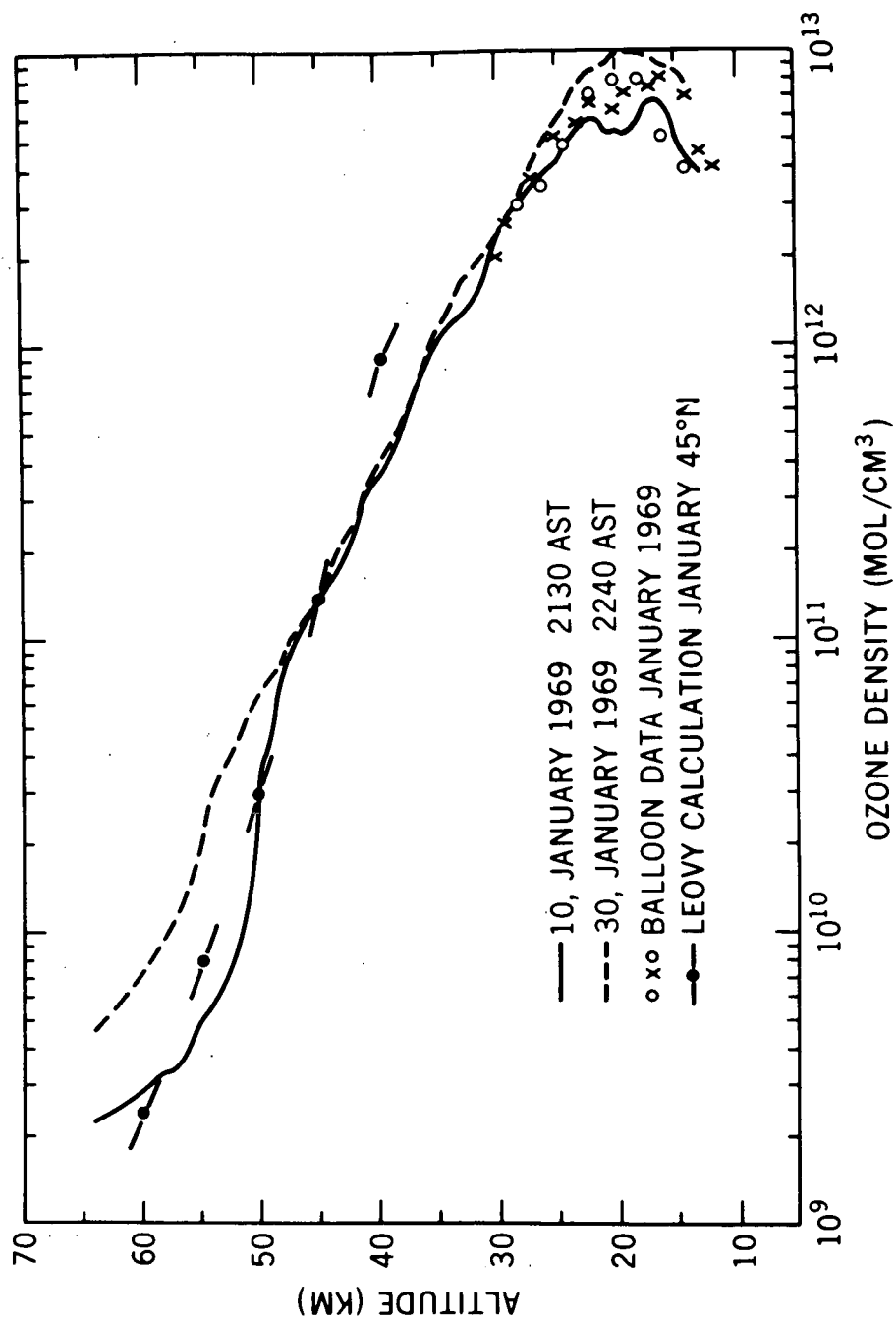


Figure 3.6.3. Ozone concentration vs height measured over Pt. Barrow Alaska 71°N on 11 and 30 January of 1969. (after Hilsenrath, 1971).

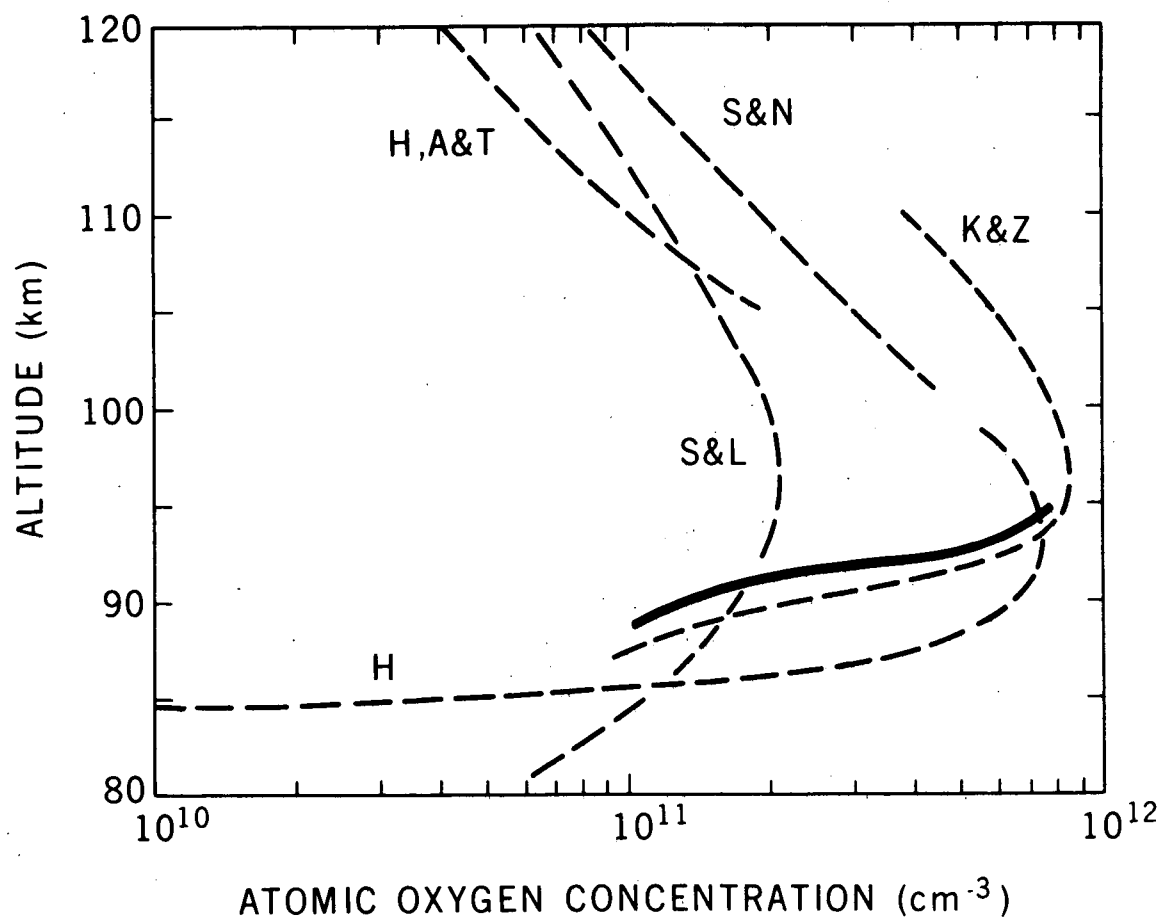


Figure 3.7.1. Atomic oxygen in the Mesosphere. Silver film measurements are presented as heavy solid line and compared to calculations of Shimazaki and Laird (1970) (S&L) Hestvedt (1968) (H), Keneshea and Zimmerman (1970) (K&Z) and Rocket Mass Spectrometer Measurements of Hedin, et al. (1964) (after Henderson, 1971).

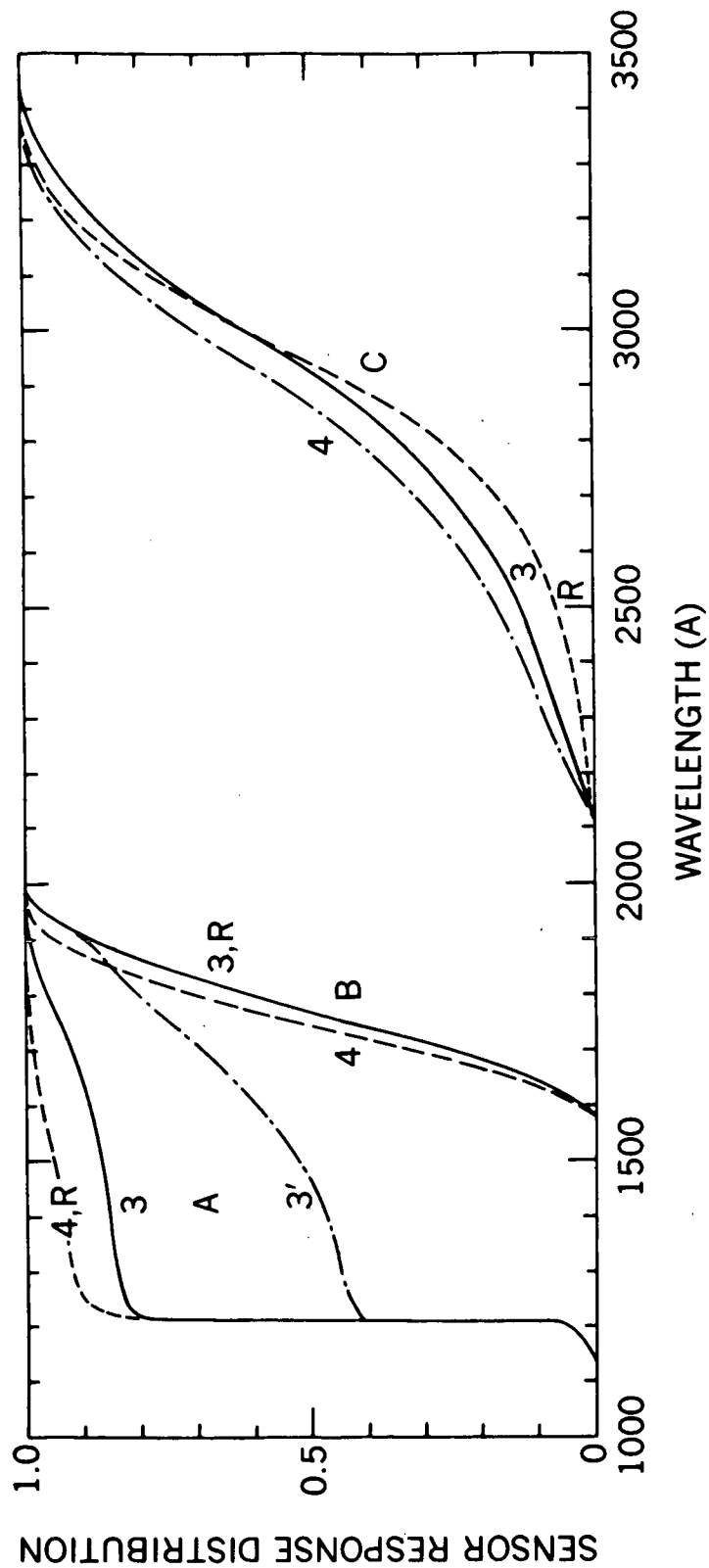


Figure 3.8.1. Sensor response distribution is the fraction of the total signal coming from wavelengths shorter than λ . A, B, C designates the three sensors used on the rocket flight (R), on Nimbus 3 (3) and on Nimbus 4 (4); and 3 illustrates the computed response distribution for sensor A after degradation in orbit. (Heath, 1971).

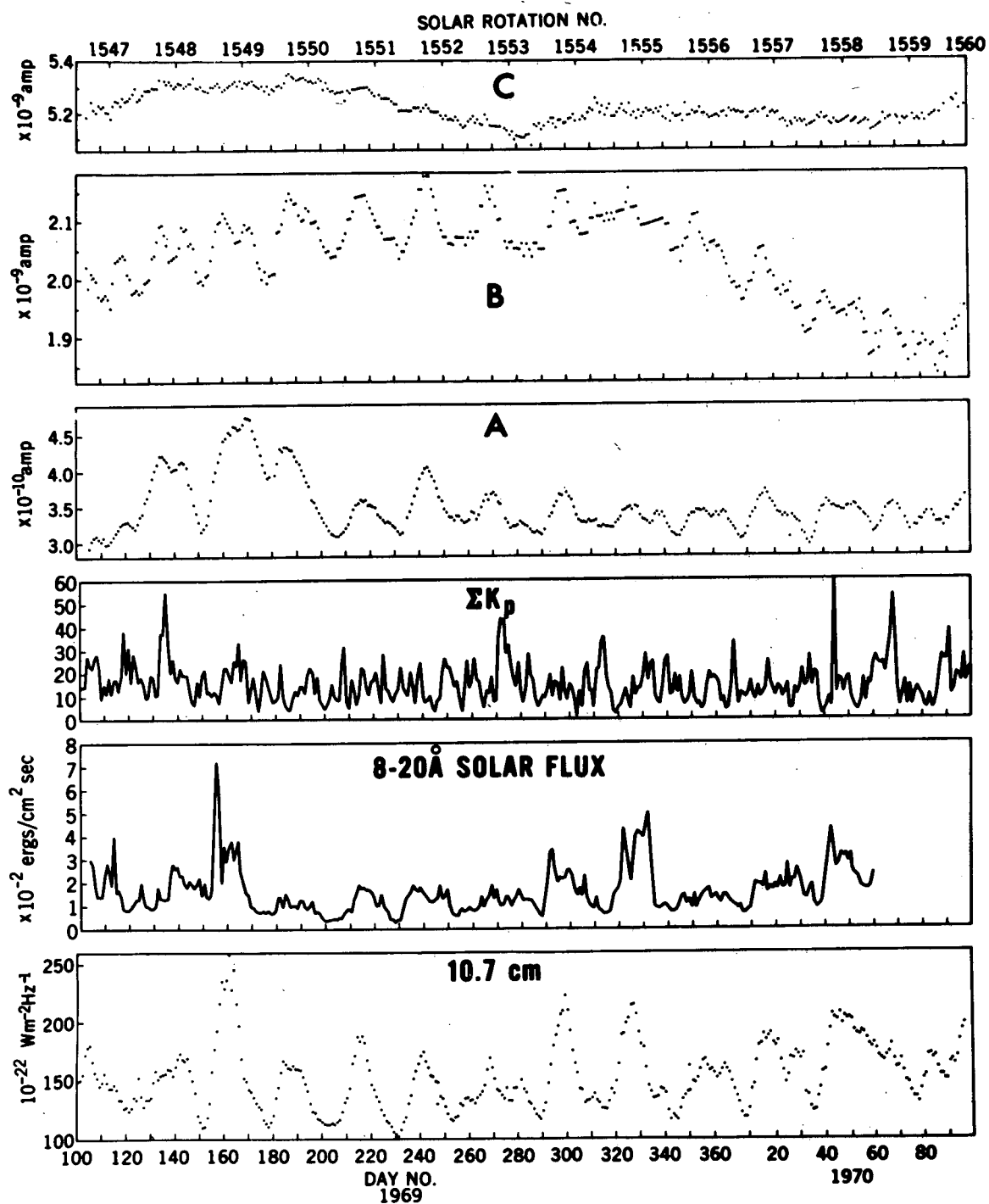


Figure 3.8.2. Time plot of MUSE sensor currents, with exponential decay factors removed, compared with other indicators of solar activity. (Heath, 1971).

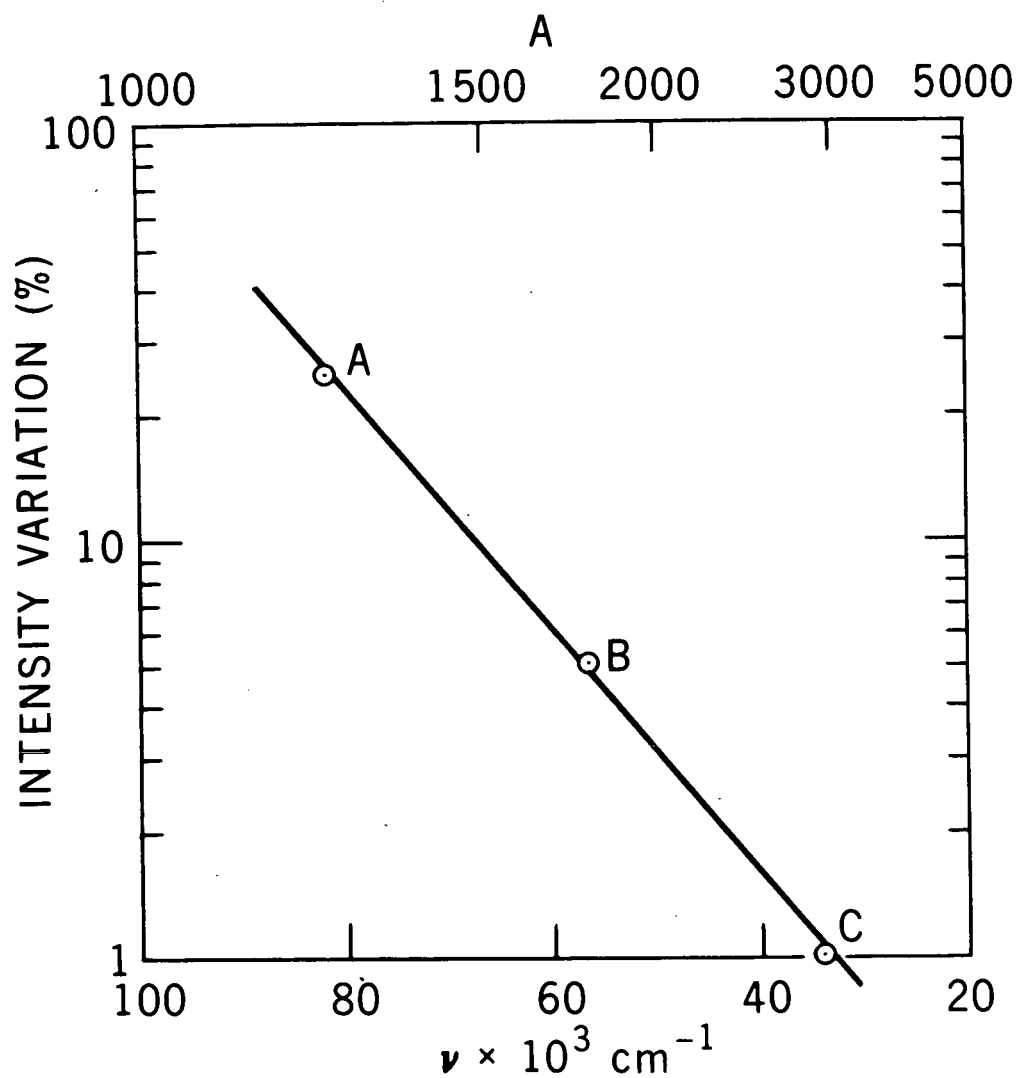


Figure 3.8.3. Percentage UV variation typically observed with the MUSE sensors versus the wave number of the 0.5 point of the response distribution given in Figure 3.8.1. (Heath, 1971).

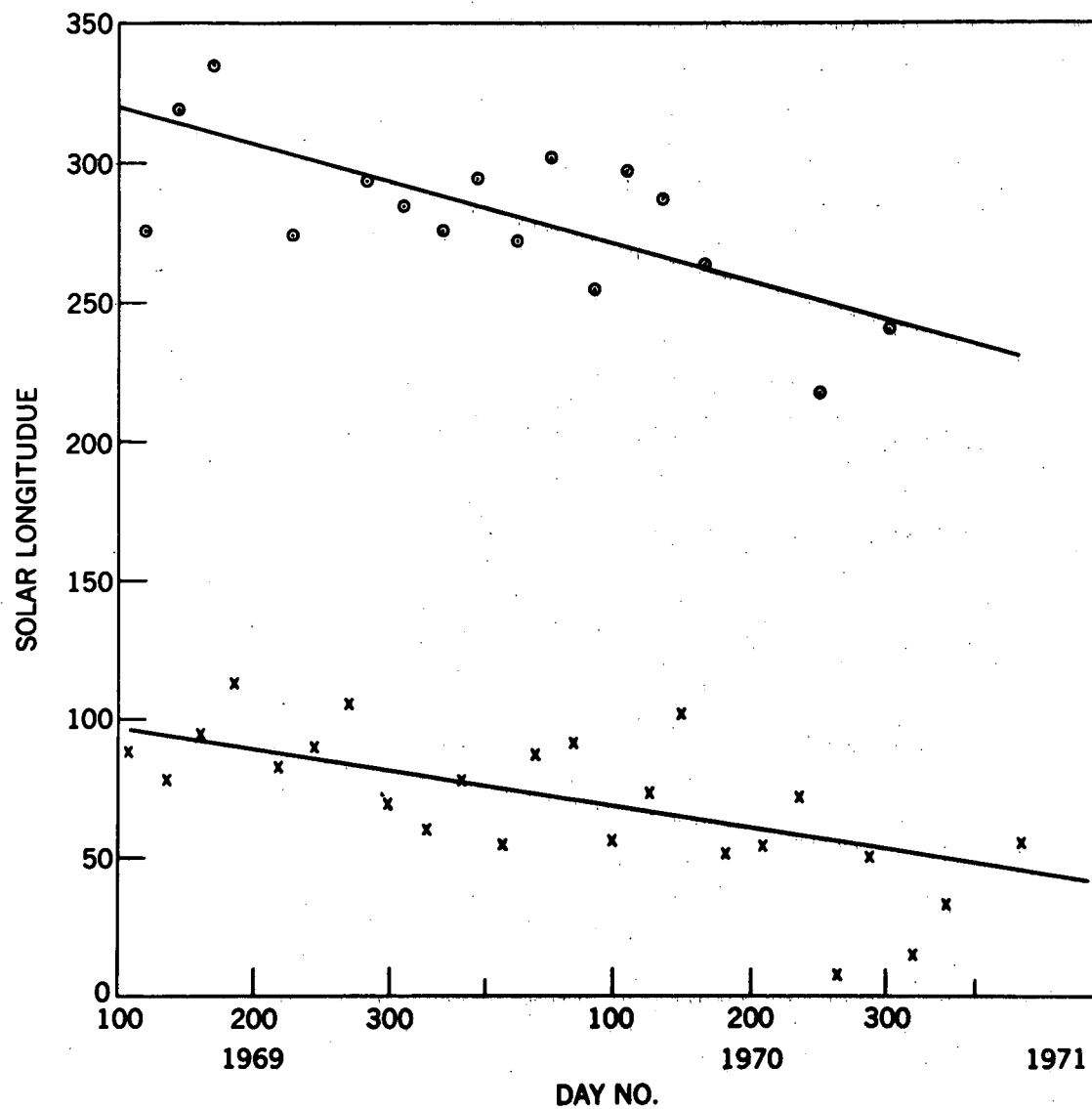


Figure 3.8.4. Carrington longitude of the central meridian at the time of observed UV flux maxima. The stronger region is indicated by (X), while the secondary region is shown by (O). (Heath, 1971).

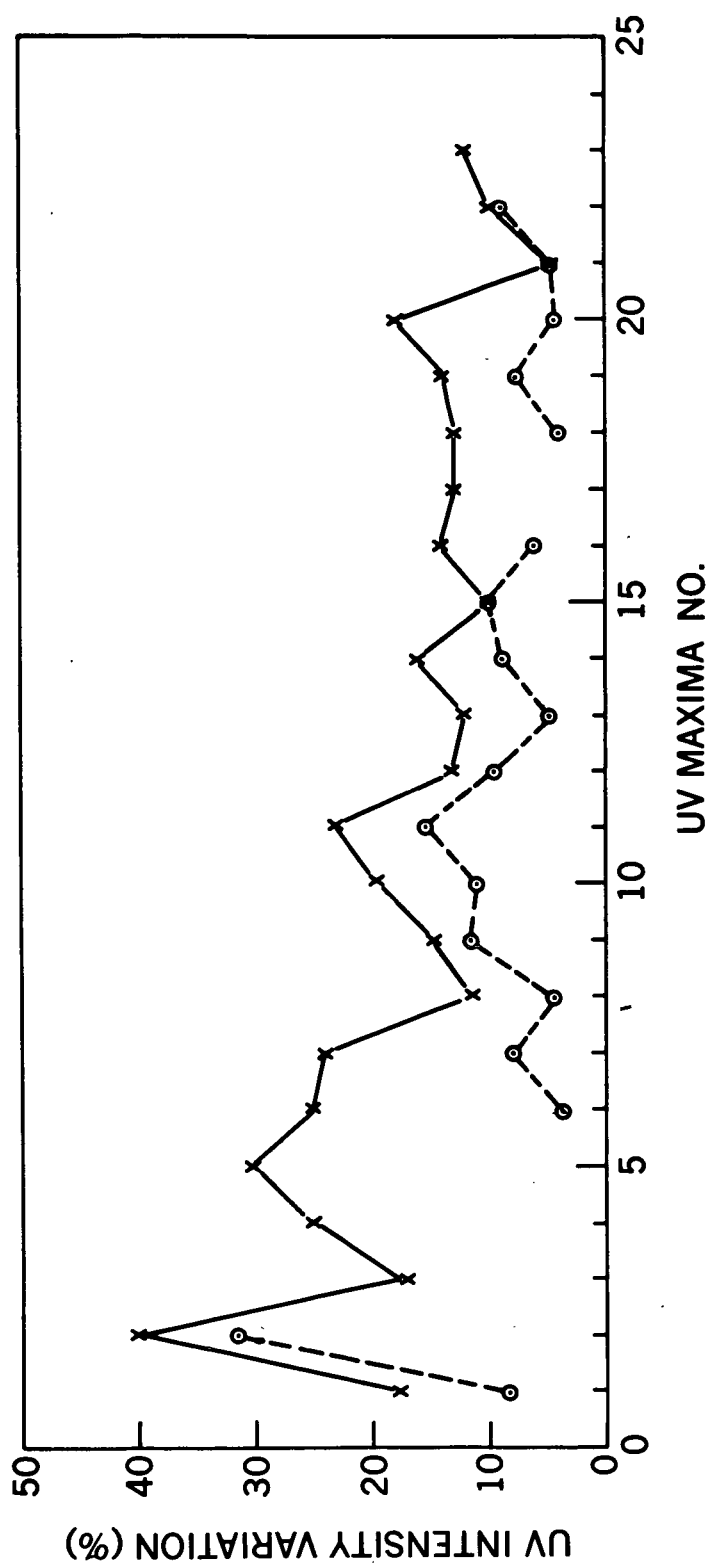


Figure 3.8.5. Time dependence of the UV flux variation observed for the two active regions. (Heath, 1971).

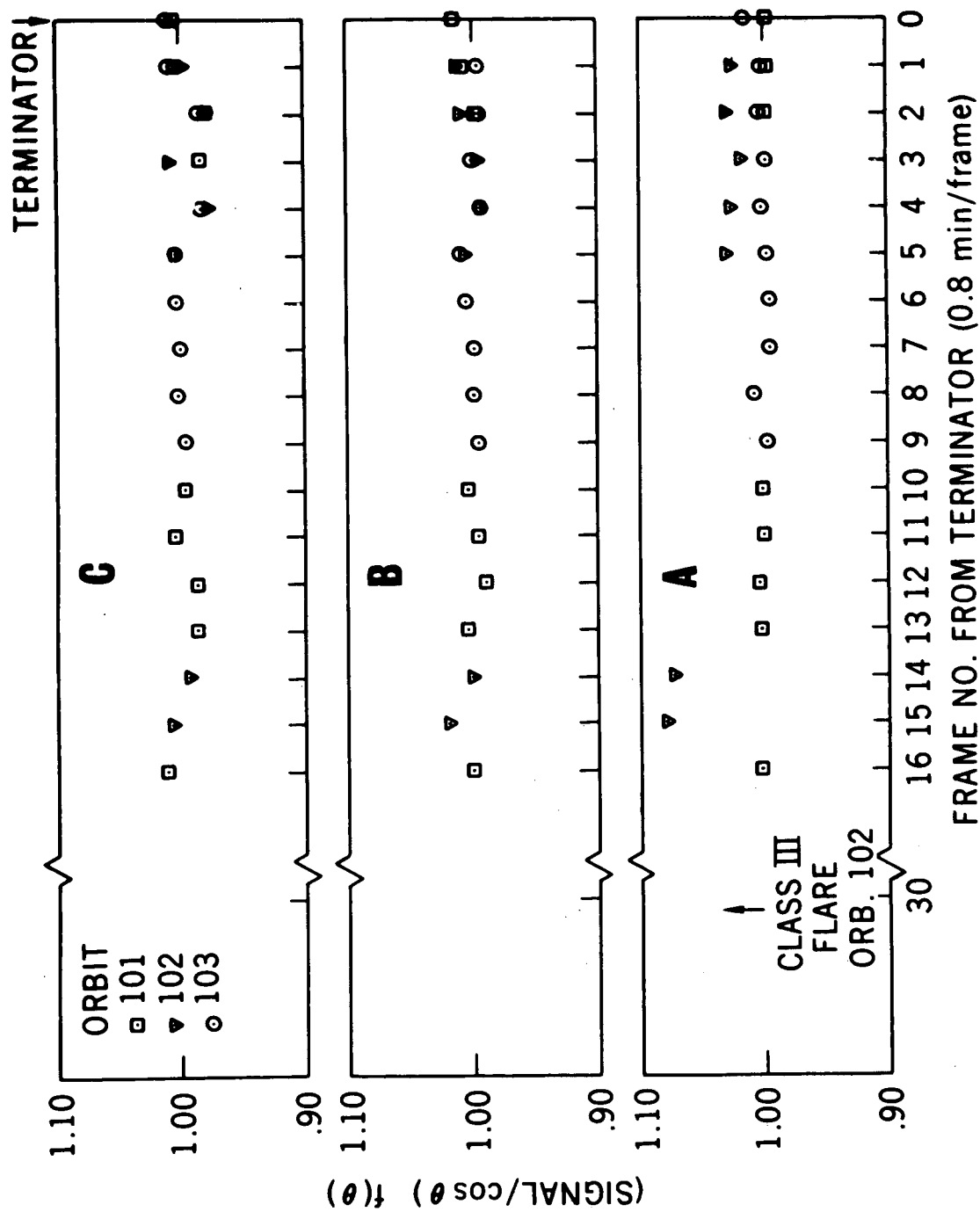


Figure 3.8.6. Enhancement of UV flux associated with major optical flare. (Heath, 1971).